



1 **A Dissertation Submitted to**
2 **Shanghai Jiao Tong University for the degree of**
3 **Doctor of Philosophy in Physics**

4
5
6 Search for new phenomena in dijet events with
7 quark/gluon tagger using the ATLAS detector

8
9
10
11
12 Wanyun Su

13
14
15
16
17 Tsung-Dao Lee Institute
18 Shanghai Jiao Tong University
19 Shanghai, P.R.China
20 August 28, 2023

21

22



23

申请上海交通大学博士学位论文

24

25

26

在 ATLAS 双喷注末态中利用 夸克/胶子标定寻找新粒子

27

28

29

30

作者：苏琬云

31

导师：李数、Shih-Chieh Hsu (University of Washington,
Seattle)

32

33

李政道研究所
上海交通大学

34

35

36

37

2023 年 8 月 28 日

38

39

上海交通大学

学位论文原创性声明

40 本人郑重声明：所呈交的学位论文，是本人在导师的指导下，独立进行研究
41 工作所取得的成果。除文中已经注明引用的内容外，本论文不包含任何其他个人
42 或集体已经发表或撰写过的作品成果。对本文的研究做出重要贡献的个人和集体，
43 均已在文中以明确方式标明。本人完全知晓本声明的法律后果由本人承担。

44 学位论文作者签名：
日期： 年 月 日

45
46

47

48

上海交通大学

学位论文使用授权书

49 本人同意学校保留并向国家有关部门或机构送交论文的复印件和电子版，允
50 许论文被查阅和借阅。

51 本学位论文属于：

- 52 公开论文
53 内部论文，保密 1年 / 2年 / 3年，过保密期后适用本授权书。
54 秘密论文，保密 ____ 年（不超过 10 年），过保密期后适用本授权书。
55 机密论文，保密 ____ 年（不超过 20 年），过保密期后适用本授权书。
56 （请在以上方框内选择打“√”）

57

58 学位论文作者签名： 指导教师签名：
日期： 年 月 日 日期： 年 月 日

摘要

这篇论文中所呈现的物理分析旨在寻找标准模型之外的新物理现象，使用积分亮度为 140 fb^{-1} ，中心质心能量为 13 TeV ，由 ATLAS 探测器记录的质子-质子碰撞数据。该分析在三个不同的谱中寻找超越标准模型的新共振体证据：未标记双喷注不变质量、一个胶子标记和两个胶子标记信道。为了增加观察新共振体的灵敏度，该分析采用了一种基于关联粒子轨迹数量的胶子标记方法，以优先地寻找一个或多个胶子衰变的共振体迹象。由于来自夸克和胶子的喷注可以使用夸克/胶子标记器进行识别，因此本研究调查了两种标记器：一种基于与喷注关联的带电轨迹数目，而另一种则采用增强决策树来结合各种喷注次级结构可观测量，同时提供了标记效率的数据与蒙特卡洛模拟之间的差异。在数据上执行矩阵方法，从夸克/胶子丰富子样本中获取夸克/胶子分数，该样本由喷注的赝快度定义。在分析中，利用了将量子色动力学背景估计为参数化双喷注质量谱的统计框架。然后在 95% 的置信水平上，针对多种超越标准模型物理理论以及一个独立于模型的通用高斯形状信号，设置了上限。

73

74 **关键词：**标准模型，ATLAS 探测器，喷注标定

ABSTRACT

75

ABSTRACT

76

77 The physics analyses presented in this PhD dissertation search for new physics be-
78 yond the Standard Model (BSM) in the dijet mass distribution using an integrated lumi-
79 nosity of 140 fb^{-1} of proton-proton collisions with a centre-of-mass energy at 13 TeV
80 recorded by the ATLAS detector. This analysis aims at searching for the evidence of
81 the BSM resonances in three different spectra: the untagged dijet invariant mass, one
82 gluon-tagged and two gluon-tagged channels. In order to increase the sensitivity to ob-
83 serve new resonances that preferentially decaying to one or more gluons, a gluon-tag
84 method based on the number of associated particle tracks is employed. Jets originating
85 from quarks and gluons can be identified using quark/gluon tagger. Two taggers are in-
86 vestigated: one tagger based on the number of charged tracks associated with the jets,
87 while the other employs a boosted decision tree to combine various jet substructure ob-
88 servables. Differences between data and Monte Carlo simulation of tagging efficiency
89 are provided. A matrix method is performed on data to retrieve the quark/gluon fraction
90 from quark/gluon-enriched subsamples, defined by the pseudorapidity of the jet. In the
91 analysis, the quantum chromodynamics (QCD) background is estimated by the statistical
92 framework which parameterised the dijet mass spectrum. Upper limits then are set at the
93 95% confidence level on a variety of theories of BSM physics and a model-independent
94 generic Gaussian shape signal.

95

96 **KEY WORDS:** Standard Model, ATLAS, calibration, jet tagging

97 Contents

<small>98</small>	1	Introduction	<small>1</small>
<small>99</small>	2	The theory framework	<small>3</small>
<small>100</small>	2.1	The Standard Model	<small>3</small>
<small>101</small>	2.1.1	Quantum chromodynamics	<small>4</small>
<small>102</small>	2.2	Physics beyond the Standard Model	<small>7</small>
<small>103</small>	2.2.1	H'	<small>7</small>
<small>104</small>	2.2.2	String	<small>7</small>
<small>105</small>	2.2.3	Quantum Black Holes	<small>8</small>
<small>106</small>	3	The ATLAS Experiment	<small>9</small>
<small>107</small>	3.1	The Large Hadron Collider	<small>9</small>
<small>108</small>	3.2	The ATLAS detector	<small>11</small>
<small>109</small>	3.2.1	Inner detector	<small>12</small>
<small>110</small>	3.2.2	Calorimeters	<small>14</small>
<small>111</small>	3.2.3	Muon spectrometer	<small>18</small>
<small>112</small>	3.2.4	Trigger and data acquisition	<small>18</small>
<small>113</small>	4	Jets in ATLAS	<small>21</small>
<small>114</small>	4.1	Jet reconstruction	<small>21</small>
<small>115</small>	4.2	Jet calibration and cleaning	<small>24</small>
<small>116</small>	4.2.1	Pile-up corrections	<small>24</small>
<small>117</small>	4.2.2	Jet energy scale and η calibration	<small>25</small>
<small>118</small>	4.2.3	Global sequential calibration	<small>26</small>
<small>119</small>	4.2.4	Residual <i>in situ</i> calibration	<small>27</small>
<small>120</small>	5	The calibration of quark/gluon jets taggers	<small>28</small>
<small>121</small>	5.1	Data and Monte Carlo samples	<small>28</small>
<small>122</small>	5.1.1	Data	<small>28</small>
<small>123</small>	5.1.2	Monte Carlo simulation	<small>29</small>
<small>124</small>	5.2	Object and Event selection	<small>30</small>
<small>125</small>	5.2.1	Physics object definition	<small>31</small>
<small>126</small>	5.2.2	Event Selection and definition of quark and gluon-enriched samples	<small>32</small>
<small>127</small>	5.3	Quark/gluon tagging variables	<small>32</small>

Contents

128	5.3.1	The BDT tagger	34
129	5.3.1.1	Feature selections	35
130	5.3.1.2	Training weights	36
131	5.3.1.3	Training Configuration	39
132	5.4	Matrix Method	42
133	5.5	MC non-closure	46
134	5.5.1	Closure test for BDT tagger	49
135	5.5.2	Summary for the MC Closure test	52
136	5.6	Scale factor	52
137	5.7	Systematic uncertainties	60
138	5.7.1	Parton shower modelling uncertainty	60
139	5.7.2	Hadronisation modelling uncertainty	61
140	5.7.3	Matrix element uncertainty	62
141	5.7.4	PDF uncertainty	62
142	5.7.5	Scale variation uncertainty	62
143	5.8	Splitting-Kernel variation uncertainty	63
144	5.9	Tracking uncertainty	63
145	5.10	JES /JER uncertainty	63
146	5.10.1	N_{trk} / BDT re-weighting	64
147	5.10.2	The MC non-closure	68
148	5.10.3	Statistical uncertainty	68
149	5.11	Results	69
150	5.12	Conclusions	87
151	6	Search for new phenomena in dijet events	88
152	6.1	Monte Carlo models	89
153	6.1.1	QCD background	89
154	6.1.2	H'	89
155	6.1.3	Strings	90
156	6.1.4	Quantum Black Holes	92
157	6.2	Events selections	94
158	6.2.1	Observables and Kinematic Variables	94
159	6.2.2	Baseline selection	95
160	6.3	Quark-Gluon Sample Selection	96

Contents

161	6.3.1	Expected Signal Significance	97
162	6.3.1.1	Resonances that decay to quark-quark	97
163	6.3.1.2	Signals that decay to gluon-gluon	98
164	6.3.1.3	Signals that decay to quark-gluon	99
165	6.3.2	Selection Criteria	101
166	6.3.2.1	Signal Selection Efficiencies	106
167	6.4	Signal Optimisation	108
168	6.4.1	y^* Cut Optimisation	108
169	6.4.2	Dijet Mass Turn-on	113
170	6.4.3	Optimised Selection	116
171	6.4.4	Selected Kinematic Plots	117
172	6.5	Statistical Framework	120
173	6.5.1	Fitting Framework	120
174	6.5.2	Statistical Method	121
175	6.5.2.1	Parametric background models	121
176	6.5.2.2	Uncertainties	122
177	6.5.2.3	Likelihood function definition	122
178	6.5.2.4	Statistical Method	123
179	6.5.2.5	Test statistic and p-value definitions	124
180	6.5.2.6	Generation of pseudo-data	125
181	6.5.2.7	Definition of exclusion limit	125
182	6.5.2.8	Implementation	126
183	6.5.3	Background Estimation	126
184	6.5.4	Analysis Strategy	126
185	6.5.5	Spurious Signal Tests	127
186	6.5.6	Fit Stability Tests	132
187	6.6	Systematic uncertainties	134
188	6.6.1	String resonance systematic uncertainties	134
189	6.6.2	q/g tagging Systematics	136
190	6.6.2.1	Pure MC Systematics	136
191	6.7	Results	138
192	6.7.1	Untagged Resonances: Model-independent Gaussian Limits . .	138

Contents

193	7 Conclusions	142
194	8 Acknowledgements	153

195

1 Introduction

196 Over the past seventy years, the theories and discoveries of thousands of physi-
197 cists have developed a notable insight into the fundamental structure of matters, called
198 fundamental particles, which are governed by four fundamental forces. One of the best
199 understandings of how these particles and three of the forces interact with each other is
200 encapsulated in the Standard Model (SM) [30, 44] of particle physics. Developed in the
201 early 1970s, it has been successfully proved by almost all experimental results. The huge
202 success of the discovery of Higgs Boson in 2012 predicted by the SM was awarded the
203 Nobel Prize in Physics in 2013. The SM has become established as a well-tested physics
204 theory.

205 Although the SM accurately describes the phenomena within its domain, there are
206 still theoretical flaws that prevent some fundamental physical phenomena from being
207 fully explained by the SM. First of all, the model contains many parameters that cannot
208 be derived from calculations alone but must be determined by experiment. In 1998, the
209 Japanese Super Kamioka neutrino detector published results on neutrino oscillations that
210 suggested the neutrinos have a non-zero rest mass, which did not match the prediction
211 made by the SM. Besides, the existence of gravity and dark matter has not yet been
212 described by the SM theory.

213 Many models of physics beyond the Standard Model (BSM) [26] predict the pres-
214 ence of new particles that couple to quarks and/or gluons. Such particles could be pro-
215 duced in proton-proton collisions at the Large Hadron Collider (LHC) [56] and then
216 decay into quarks and gluons, during this process two hadronic jets are created, which
217 then can be seen by the detector. The new energy regime ($\sqrt{s} = 13$ TeV) with an inte-
218 grated luminosity of 140 fb^{-1} provided by the LHC opens a window to search for BSM
219 particles.

220 In the SM, these dijet events are generated mainly by quantum chromodynamic
221 (QCD) processes and appeared to be a smoothly decreasing invariant mass (m_{jj}) dis-
222 tribution, however, a new particle that decays into quarks or gluons could appear as a
223 resonance in the m_{jj} spectrum. If the resonant samples can be classified based on the
224 type of parton that initiated the jets, the sensitivity of the search for such resonances
225 could be largely increased. Hence, classifying jets as initiated from a quark or a gluon
can be effective for improving SM measurements and searches for BSM physics.

Introduction

Recent developments [52, 49, 47, 51, 46, 45, 48, 8, 9, 69, 41, 75, 43, 54, 86, 24, 65] in quark/gluon (q/g) tagging have resulted from advances in the theoretical [36], phenomenological [58, 63, 60, 66] and experimental understanding of q/g tagging as well as the development of powerful machine learning techniques that can utilize the entire jet internal radiation pattern. The calibration of q/g taggers is performed to account for the systematics of searching results.

This thesis is structured as follows. Chapter 2. describes the theoretical framework of the SM, its limitations and various potential extensions beyond it. An introduction to the LHC and the ATLAS detector is given in Chapter 3. Jet reconstructions and calibrations are briefly described in Chapter 4. The quark/gluon tagger definitions and the selection criteria used to generate the various event samples employed in the discriminant extraction, the method and the scale factor results are presented in Chapter 5. The details of the search for new resonances in the dijet spectrum and the limit setting results are shown in Chapter 6. In the end, the conclusion and outlook of the research are presented in Chapter 7.

242

2 The theory framework

243 2.1 The Standard Model

244 The Standard Model of particle physics, which describes the three fundamental
 245 interactions - strong, weak and electromagnetic interactions - and the fundamental par-
 246 ticles that make up all matter, is the most successful theory of particle physics known.
 247 The SM divides particles into two categories, fermions and bosons, based on the values
 248 of their spin: fermions are the particles that makeup matter, such as electrons in leptons,
 249 quarks and neutrinos, which have half-integer spin; bosons are the particles that trans-
 250 mit forces, such as photons and mesons that transmit electromagnetic forces, gluons that
 251 transmit strong nuclear forces, W and Z that transmit weak nuclear forces, have integer
 252 spin. Different properties shown in fermions and bosons are due to the difference in
 253 spin. According to the spin-statistics theorem, fermions obey the Pauli exclusion princi-
 254 ple, whereas bosons do not, thus bosons do not have a theoretical limit on their spatial
 255 density.

256 The SM is a paradigm of a quantum field theory which provides the mathematical
 257 framework for it. The Lagrangian controlled the dynamics and kinematics of the system
 258 satisfies the $SU(3) \times SU(2)_L \times U(1)_Y$ gauge symmetry, in which $U(1)_Y$ corresponds to
 259 a particle B with weak hypercharge Y . $SU(2)_L$ corresponds to particles W_α ($\alpha = 1, 2,$
 260 $3)$ with weak isospin T and only left-handed chiral particles. The electroweak force
 261 which unifies the electromagnetism and the weak interaction as a Yang-Mills field is
 262 represented by the group $SU(2)_L \times U(1)_Y$, mathematically. In SM, the Z^0 boson and the
 263 photon (γ) are given by:

$$\begin{pmatrix} \gamma \\ Z^0 \end{pmatrix} = \begin{pmatrix} \cos \theta_W & \sin \theta_W \\ -\sin \theta_W & \cos \theta_W \end{pmatrix} \begin{pmatrix} B \\ W_3 \end{pmatrix} \quad (2.1)$$

264 where θ_W is the weak mixing angle.

265 The charged massive bosons W^\pm are given by W_1 and W_2 :

$$W^\pm = \frac{1}{\sqrt{2}} (W_1 \mp iW_2) \quad (2.2)$$

266 $SU(3)$ corresponds to eight vector fields A^α ($\alpha = 1, 2, \dots, 8$) representing gluon fields,
 267 which are vector gauge bosons that carry the colour charge of the strong interaction and

mediate between quarks in QCD. The Higgs boson, unlike all other known bosons such as the photon, is a scalar boson and has a non-zero average value in vacuum. It is resulted from the process of spontaneous symmetry breaking. The Higgs mechanism explains the generation of the property "mass" for gauge bosons. At a critical temperature, the Higgs field introduces a vacuum expectation value that causes spontaneous symmetry breaking during interactions, leads the bosons it interacts with acquire masses. A Yukawa coupling is used in the SM to describe the interaction between the Higgs field and fundamental fermions, explain the generation of the masses of fermions.

This chapter therefore focuses on the present SM, various extensions and variants of the SM that have been proposed by theoretical physicists are explored in Section 2.2.

2.1.1 Quantum chromodynamics

QCD is the theory of the strong interaction between quarks and gluons, and it is a fundamental component of the SM of particle physics. Satisfying the $SU(3)$ symmetry group invariant, QCD is a non-abelian gauge theory, over the years, QCD has collected a huge body of experimental evidence, proved that it has been a successful application from a quantum field theory.

The Lagrangian of QCD can be expressed as:

$$\mathcal{L}_{\text{QCD}} = \bar{\psi}_i \left(i\gamma^\mu (D_\mu)_{ij} - m\delta_{ij} \right) \psi_j - \frac{1}{4} G_{\mu\nu}^a G_a^{\mu\nu} \quad (2.3)$$

where ψ_i is the quark field in the fundamental representation of the $SU(3)$ gauge group, indexed by i and j running from 1 to 3; m corresponds to the quark mass; the γ^μ are Dirac matrices relating the spinor representation to the vector representation of the Lorentz group.

D_μ is defined as the gauge covariant derivative:

$$(D_\mu)_{ij} = \partial_\mu \delta_{ij} - ig_s (T_a)_{ij} \mathcal{A}_\mu^a \quad (2.4)$$

which couples the quark field with a coupling strength g_s to the gluon fields via the infinitesimal $SU(3)$ generators T_a . By including the Gell-Mann matrices λ_a ($a=1\dots 8$), an explicit representation of T_a is defined by $T_a = \lambda_a/2$.

293 The gauge invariant gluon field strength tensor $G_{\mu\nu}^a$ is given by:

$$G_{\mu\nu}^a = \partial_\mu A_\nu^a - \partial_\nu A_\mu^a + g_s f^{abc} A_\mu^b A_\nu^c \quad (2.5)$$

294 where A_μ^a are the gluon fields, indexed by a, b and c running from 1 to 8; f^{abc}
 295 are the structure constants of $SU(3)$. The coupling strength g_s can be referred to strong
 296 coupling constant α_s :

$$\alpha_s = \frac{g_s^2}{4\pi} \quad (2.6)$$

297 There are some salient properties that QCD exhibits:

298 Colour confinement

299 This is a consequence of the force between two colour-charged particles that can
 300 not be isolated in a condition that below the Hagedorn temperature of approxi-
 301 mately 2 terakelvin. To separate two quarks in a hadron, extremely high energy
 302 is required, leading to the creation of a quark-antiquark pair that formed a pair of
 303 hadrons rather than a single hadron. In addition, glueballs which are formed only
 304 of gluons are colourless and also consistent with confinement, causing difficulty
 305 in identification in experiments.

306 Asymptotic freedom and the running coupling

307 This is a feature of QCD that demonstrates the strong interactions between quarks
 308 and gluons become asymptotically weaker as the energy scale of them increases
 309 and the corresponding length scale decreases. This is opposite to the behaviour of
 310 colour-charged particles at low energies where the confinement of quarks and glu-
 311 ons exhibits. At high energy, the coupling decreases logarithmically as a function
 312 of momentum transfer Q :

$$\alpha_s(Q^2) \stackrel{\text{def}}{=} \frac{g_s^2(Q^2)}{4\pi} \approx \frac{1}{\beta_0 \ln(Q^2/\Lambda^2)} \quad (2.7)$$

313 where β_0 is a one-loop beta function in QCD and has the dependence of the cou-
 314 pling parameter g_s . The quantity Λ is referred to QCD scale that is measured
 315 in processes where the strong coupling constant and other measurables vary with
 316 momentum transfer Q . However, this is only effective at leading order (LO). By

317 including higher order terms, the calculation expanded in order of α_s resulted in
 318 more complexity and less significance as the scale of Q increases. On the other
 319 hand, as Q tends to be infinite large, the coupling strength becomes zero thus the
 320 behaviors of quarks are asymptotically free. These variation of coupling α_s under
 321 the different scales of energy in QCD is described as the running coupling.

322 The calculation of matrix element in QCD can be rather complex as more and more
 323 perturbative contributions are considered, which requires the application of complicated
 324 integrals over a large number of variables. A Feynman diagram is used as a representa-
 325 tion of the expressions of these integrals pictorially and an improvement of undertaking
 326 the critical calculations.

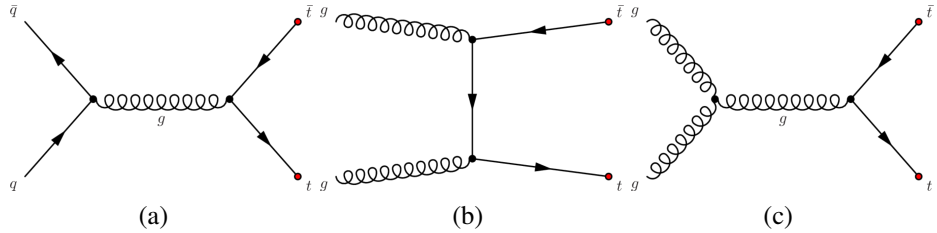


Figure 2.1 Feynman diagrams of strong interaction in top-antitop quarks production via (a) one gluon exchange in quark-antiquark annihilation, gluon-gluon fusion in (b) t-channel and (c) s-channel.

327 With more interactions points involved in, more complicated the calculations be-
 328 come. The effects of self-interactions between particles themselves can happen by pro-
 329 ducing a virtual particle which is restricted by the uncertainty principle, represented as a
 330 loop in a Feynman diagram. The accuracy of the calculation has dependency on the cou-
 331 pling α_s and is contributed to a fraction at each order. By including an infinite number
 332 of virtual particles, the calculations are led to divergent and infinite. A set of techniques
 333 named renormalization are employed in solving the infinities showed up in the calcu-
 334 lations, by which the infinite self-interactions are parameterised by re-scaling them as
 335 finite values to compensate the effects. The ultraviolet divergence that occurs from inte-
 336 grating the contributions at extreme high energy is represented by renormalization scale
 337 μ_R , on the contrast, μ_F represents the condition of an integral diverges at infinitesimal
 338 energy.

339 **2.2 Physics beyond the Standard Model**

340 **2.2.1 H'**

341 Many extensions of the SM predict the existence of new heavy Higgs-boson-like
342 particles. 2HDMs are a wide set of models in which the couplings scale with Yukawa
343 couplings thus leads to a relatively small branching ratio of the scale H or pseudoscalar
344 A to gluons. New particles that decay into photons are also predicted by BSM and have
345 a branching ratio to gluons. Besides, some classes of models predicted the new particle
346 decaying into photons with a branching ratio to gluons, where the relative branching
347 ratio of photons to gluons is model-dependent. Models with new heavy fermions through
348 scalar decays to gluons are also exist.

349 The motivation of a model-independent di-gluon resonances is that the m_{jj} back-
350 ground is dominated by valence quark scattering at high energy, which leads gluon tag-
351 ging particularly effective. At higher energy, there is higher jet constituent multiplicity
352 that makes gluon tagging becomes more effective, thus the search in this analysis could
353 gain the most from gluon tagging.

354 For this analysis, a high mass simulated $SU(3)$ singlet scalar H' decaying into a
355 pair of gluons is used. The physical width in practice is set to be narrow to be model-
356 dependent and thus the m_{jj} width is set by the detector resolution.

357 **2.2.2 String**

358 A mathematical framework named string theory has contributed to a variety of prob-
359 lems in the SM such as the existence of gravity, it offers a unified description of particle
360 physics and gravity. String theory handles point-like particles as one-dimensional objects
361 called strings and demonstrates the behaviours of these strings propagating through time
362 and space. By regarding particles as infinitesimal vibrating strings, the charge, mass,
363 and other properties of them are determined by the vibration or twist of the strings. A
364 dynamical object called brane is employed to generalize the representation of a point
365 particle to higher dimensions such that a string can be regarded as a brane of dimension
366 one and can propagate through time and space under the principles of quantum mechan-
367 ics. Among them, a so-called Dirichlet membrane (D-brane) is widely used as the open
368 strings satisfy the Dirichlet boundary conditions.

369 In this analysis, we consider type-II string theory which includes a D-brane local-

370 ized in $p + 3$ partial dimension: D p -brane, compactified on a six-dimensional torus. The
371 choice of the string mass scale M_s is to be smaller than the 4-dimensional Planck scale to
372 keep the coupling small, at the expense of introducing $9 - p$ large transverse dimensions
373 felt only by gravity. Only the fundamental string scale in the TeV range is what this
374 analysis is interested in.

375 By considering the main subprocesses in dijet production that are independent of
376 the details of the compactification. Amplitudes, which include $2 \rightarrow 2$ scattering processes
377 involving two gluons and two quarks, or four gluons, are independent of the details of the
378 compactification such as the configuration of branes. This model independence makes it
379 possible to compute the string corrections to QCD dijet processes.

380 **2.2.3 Quantum Black Holes**

381 Quantum Black Holes (QBH), also called micro black holes, are regarded as hy-
382 pothetical mini (less than a solar mass unit) black holes that dominated by quantum
383 mechanical effects. Some hypotheses predict that QBH could be produced at energies as
384 low as the TeV range, which can be generated in particle accelerators such as the LHC
385 and can be observed through the particles that are emitted by the process of Hawking
386 radiation.

387 In the simplest scenario, the decay of QBH via Hawking radiation can be approx-
388 imately described as isotropic decay to a many-particle final state. The threshold of
389 quantum-gravity energy scale M_D is set to be well below the the actual thermal black
390 hole production threshold for gravitational interactions so that two-body states in final
391 states are the dominant, a resonance-like result is expected in predominantly two-body
392 final states as jets near M_D . Such isotropic final states is aimed as probes of quantum
393 gravitational effects in this dijet analysis.

3 The ATLAS Experiment

395 3.1 The Large Hadron Collider

396 The LHC, built by European Organization for Nuclear Research (CERN) located in
 397 Geneva, Switzerland, is the largest circular particle accelerator in the world. The goal of
 398 it is to probe the various theoretical predictions made by physicists.

399 It consists superconducting magnets that construct a 27-kilometer ring lying in the
 400 tunnel under the ground. Inside the LHC, two beams made of protons or ions are accel-
 401 erated to extreme high speed in opposite direction in individual vacuum pipes then made
 402 into collision by a strong magnetic field within the structures.

403 The LHC is the last section of the CERN accelerator complex where a series of
 404 machines accelerates the particles to increasingly higher and higher energies. The highest
 405 energies of beams are reached at the LHC.

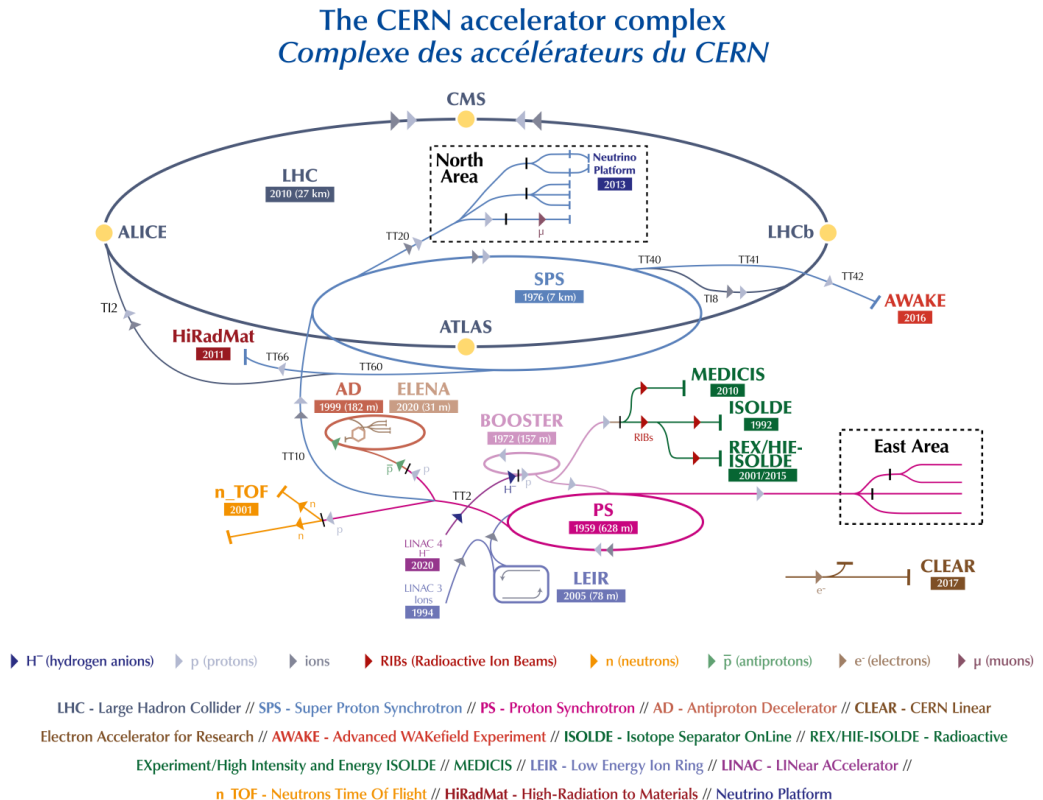


Figure 3.2 The CERN accelerator complex

406 Seven detectors are placed around four collision points in the collider. Different
 407 types of particles are accelerated according to the research, the main beams are protons,
 408 but the LHC also run beams of heavy ions as lead–lead collision or proton–lead collisions.

409 The energy of particles is increased by a series of processes before being injected
 410 into the main accelerator. For a proton-proton collision, negative hydrogen ions are gen-
 411 erated by the linear particle accelerator Linac4 at 160 MeV then injected into the Proton
 412 Synchrotron Booster, where protons are obtained by stripping electrons away from the
 413 atom and accelerated to 2 GeV. After entered the Proton Synchrotron the energy of the
 414 protons is 26 GeV, and then their energies are increased in Super Proton Synchrotron to
 415 450 GeV before they are finally injected into the main ring.

416 One of the characteristics that defines the power of an accelerator is the centre-of-
 417 mass energy, which represents the total momentum of the system and thus indicates the
 418 total mass of potential new particles as well as probes the internal structure of known
 419 particles under the law of energy invariant within the system. In 2010, the first collisions
 420 were made at an energy of 3.5 TeV each beam, later in 2018, an energy of 6.5 TeV per
 421 beam was achieved, resulted in the centre-of-mass energy of 13 TeV where the protons
 422 moved at a 99.9% speed of light. It took less than 90 μ s for photons to go through the
 423 whole LHC ring.

424 Other quantities such as luminosity, denoted as \mathcal{L} , also represents the performance
 425 of an accelerator. It is the rate of interactions during a certain period of time and can be
 426 expressed as:

$$\mathcal{L} = \frac{N^2 f_{rev}}{4\pi\sigma_x\sigma_y} \quad (3.1)$$

427 where N is the number of particles in a bunch, in the case that a beam has Gaussian
 428 distribution and has brunches crossing frecuency f_{rev} . σ_x and σ_y denote as transverse
 429 beam widths in the x- and y-plane. The luminosity takes the units of $\text{cm}^{-2} \cdot \text{s}^{-1}$.

430 The total number of physics events detected can be express as:

$$N_{\text{event}} = \sigma_{\text{event}} \cdot \int \mathcal{L} dt \equiv \sigma_{\text{event}} \cdot L \quad (3.2)$$

431 where L is the integrated luminosity with respect to time, σ_{event} is referred to the
 432 cross section of a specific physics process. The integrated luminosity takes the units of
 433 cm^{-2} which equals to the unit femtobarn (fb).

434 At the LHC, thousands of magnets around the accelerator are operated at a very
 435 low temperature of 271.3°C to maintain its superconducting state which allow them to
 436 conduct electricity without loss of energy. Hence, a system of liquid helium is used for
 437 cooling the accelerator and supply services.

438 Besides, superconducting radio frequency cavities which resonate electromagnetic
 439 fields are employed to accelerate the protons. Instead of having continuous beams, the
 440 protons are made into bunches, so that the collisions are taken place at discrete intervals
 441 between two beams with 115 billion protons per bunch at the frequency of 25 ns.

442 3.2 The ATLAS detector

443 The ATLAS detector [32] is the largest volume detector ever constructed for general-
 444 purpose particle research at the LHC. It has the shape of a cylinder with 44 meters long,
 445 7000 tonnes in weight and 25 meters in diameter, sitting in a cavern underground. It
 446 is designed to collect evidence of the properties of SM and search for new predictions
 447 made by particle physics beyond the SM.

448 To record the energy, momentum and trajectory of particles after collisions, the
 449 detector consisting of 6 different detecting subsystems placed in layers surrounding the
 450 interaction point to measure them individually and effectively.

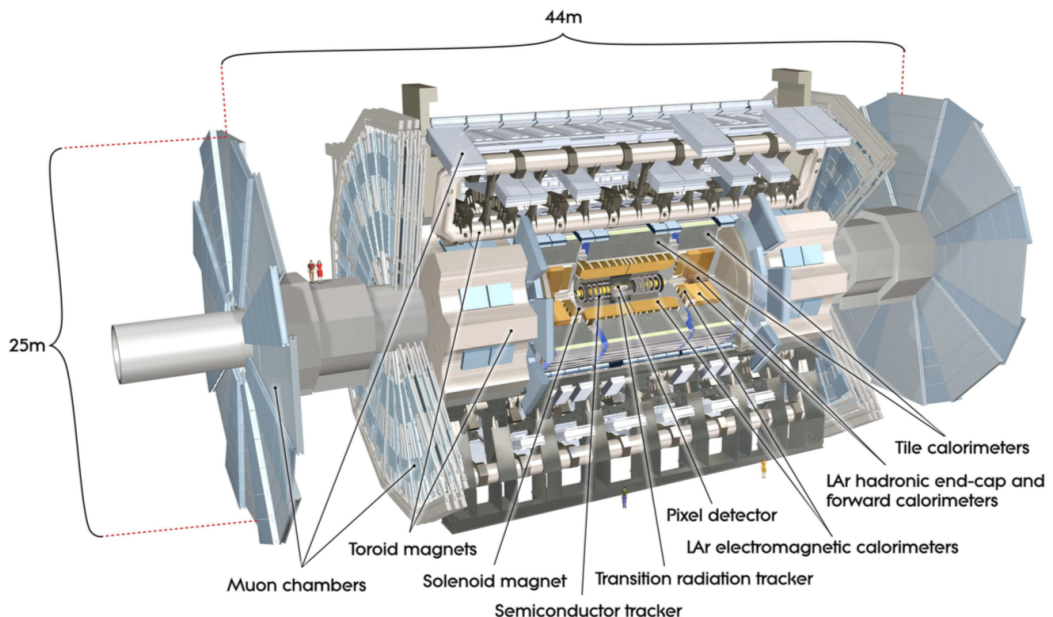


Figure 3.3 Cut-away view of the ATLAS detector

451 An overall layout of the ATLAS detector is shown in Figure 3.3.

452 **3.2.1 Inner detector**

453 Charged particles above a certain p_T threshold are detected by the ATLAS Inner
454 Detector (ID) which immersed in a 2 T solenoidal field, covered the pseudorapidity range
455 $|\eta| < 2.5$. Appearing as tracks in the ID, an excellent momentum resolution as well as
456 both primary and secondary vertex of them are provided by the ID. Within the range
457 $|\eta| < 2.0$, electron identification is also provided.

458 The layout of the ID is shown in Figure 3.4 in cylindrical coordinate: $r = \sqrt{x^2 + y^2}$,
where x -axis alongside the LHC ring and y -axis is perpendicular to the x -axis.

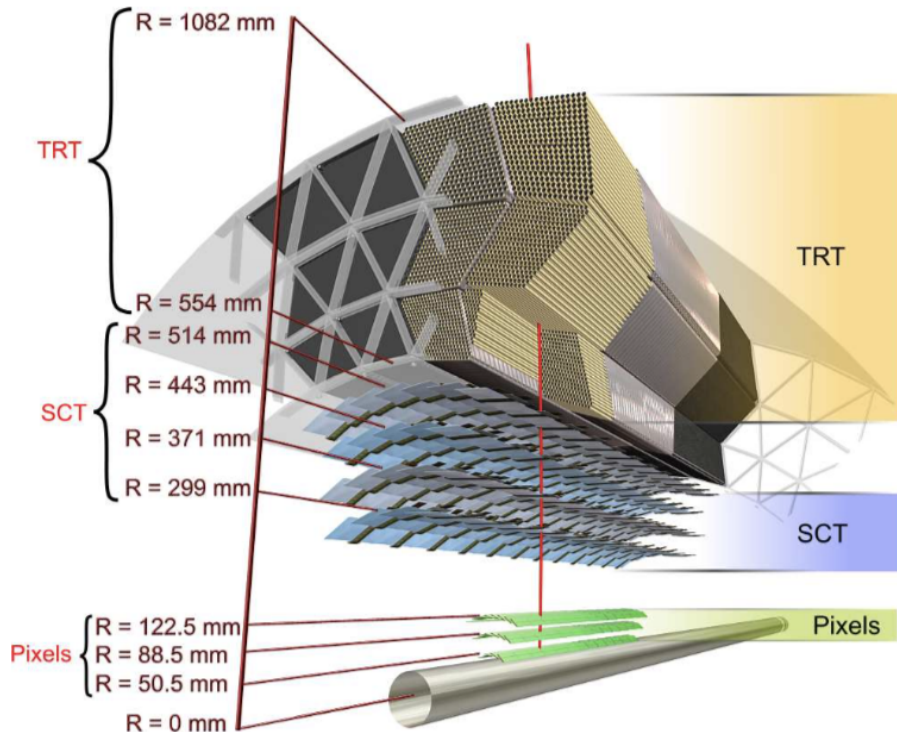


Figure 3.4 Cut-away view of the ATLAS ID. Sensors and structural elements traversed by a charged track of 10 GeV p_T in the barrel inner detector along with their envelopes in r .

459
460 A cylindrical container around the ID has a length of 3512 mm each way and a
461 radius of 1150 mm, tracks of 10 GeV traverse the sensors and structural elements in the
462 barrel and end-cap regions, respectively.

463 Within the inner region, a series of discrete space points provided by the silicon

464 pixel detector and stereo pairs of silicon microstrip semiconductor tracking (SCT) lay-
465 ers gives high-resolution pattern recognition abilities. By increasing radial distances,
466 the transition radiation tracker (TRT) provides extra pattern recognition and momentum
467 resolution capabilities.

468 **The pixel detector**

469 A series of high-granularity measurements is provided by the pixel detector [2]
470 which is composed of the innermost sub-detector of the ID, it is designed as close
471 to the interaction point as possible. Three sub-sections: two end-cap perpendicular
472 to the beam axis and a barrel alongside the beam axis as a concentric cylinder with
473 four layers (average radii of 33.25, 50.5, 88.5 and 122.5 mm, respectively) in it.

474 The innermost pixel layer (or B-layer, IBL) is essential to b-tagging performance
475 and supersymmetry searches as it cover the full acceptance of short-lived parti-
476 cles such as B hadrons and τ leptons from the beginning of Run-2 to enhance the
477 measurement of the secondary vertex. Besides, a new readout sensor and chip
478 responsible for higher radiation damage and higher hit rate, respectively, is em-
479 ployed in the IBL compared to the other three layers in the barrel region. A new
480 n-in-n planar and 3D silicon sensors with hit efficiency of greater than 97% is de-
481 veloped as well. The better impact parameter resolution is achieved by reducing
482 the pixel size of the chip down to $50 \times 250 \mu\text{m}^2$. Around 80 million readout sec-
483 tions counting them all provide the great hit resolution of $10 \mu\text{m}$ in radius plane
484 and $115 \mu\text{m}$ alongside the z-axis in the pixel detector.

485 **The semiconductor tracker**

486 Surrounding the pixel detector is the SCT which encompasses silicon based semi-
487 conductor sensing components in barrel and end-cap geometries. Four silicon mi-
488 crostrip layers, located at radii of 300, 373, 447 and 520 mm, in the barrel region
489 of the SCT provide high granularity points. The mean size of each strip pitch is
490 $80 \mu\text{m}$ for the rectangular barrel sensors as daisy-chained with 6 cm-long. For
491 the end-cap sensors, nine disks cover $|\eta| < 2.5$ are chosen. As a result, there are
492 thus 768 readout strips with $6.36 \times 6.40 \text{ cm}^2$ in size in total, with additional two
493 strips at the edge of the sensor. 6.1 m^2 of silicon detectors with 6.2 million readout
494 channels as a whole intergrated the SCT.

495 **The transition radiation tracker**

496 The outermost layer of the ID is the TRT which encompasses polyimide drift(straw)
497 tubes that designed to enable as much less wall thickness and material as possible
498 while maintaining the good experimental properties. With 4 mm in diameter and
499 150 cm in length, 73 layers of 144 cm alongside the beam with 50 thousands tubes
500 and 37 cm tubes consisting 160 tubes planes in the end-cap with 320 thousands
501 radial tubes.

502 The xenon-based gas filled up in a given tube provides the track hit of a particle as
503 it ionized as the emitting electrons drifting to the center wire of the tube volume.
504 An average of 36 hits per charged-particle track is given by the TRT, The result-
505 ing electrical signals are obtained by converting the drifting charge currents. In
506 total 420 thousands of electronics channels in which a good spatial resolution and
507 drift-time measurement are provided by the TRT, enhancing the precision mea-
508 surements of momentum in the ID.

509 **3.2.2 Calorimeters**

510 Outside of the ID lies the ATLAS calorimeters system which is designed to obtain
511 the energy lost of the particles that travel through the detector components. Multiple
512 layers of high-density material are placed to consume the energy of the incoming par-
513 ticles inside the materials and stop them from further moving. An “active” medium
514 is left inside the layers that allows experimental physicists measure the energy of those
515 particles.

516 Two types of calorimeters are employed in the ATLAS calorimeters system: the en-
517 ergy of electrons and photons are measured by the electromagnetic calorimeters as they
518 create reaction with matter. Hadronic showers that created by the interaction between
519 hadrons and atomic nuclei, are sampled by the hadronic calorimeters. Muons and neutrini-
520 nos can not be stopped by the calorimeters as they interact only weak force but the track
521 footprints could be seem in the calorimeters. The layout of the calorimeters is shown in
522 Figure 3.5.

523 The electromagnetic (EM) calorimeter covers a range of $|\eta| < 3.2$ by combining
524 the one barrel and two end-cap modules as cylindrical cryostat, with an outer radius of
525 2.25 m, an end-cap thickness of 0.632 m and a length of 3.17 m. The hadronic calorime-
526 ter covers the central barrel region of $|\eta| < 1.0$ and two extended barrels in a region of
527 $0.8 < |\eta| < 1.7$. with a radius of 2.28 m at the inside and 4.25 m at the outside. Fig-

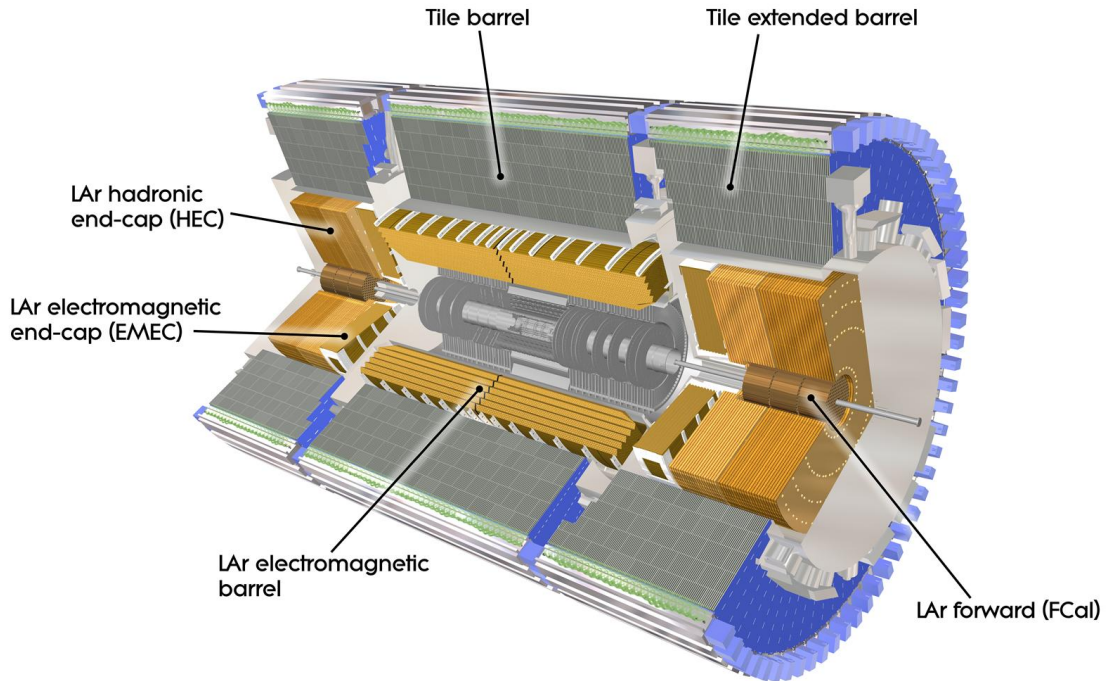


Figure 3.5 Outline of the ATLAS Run 2 trigger and data-acquisition system.

528 Figure 3.6 demonstrates the positions of the end-cap of the calorimeters including the EM
 529 and Hadronic calorimeters.

530 **The electromagnetic calorimeter**

531 The EM calorimeter that surrounds the ATLAS ID is designed for the high-
 532 granularity measurements of the energy of photons, electrons and hadrons with
 533 Liquid Argon (LAr) sandwiched between the multiple layers ionised. It converts
 534 the incoming particles into electric currents by absorbing the energy of these par-
 535 ticles as they interact with the metal with the bremsstrahlung phenomenon. A pair
 536 of electron-positron produced by an electron radiation in the EM calorimeter can
 537 initiate further electron-positron pairs (as showers) until the energy of the parti-
 538 cles fall below the certain threshold, the dominate process thus become ionisation
 539 in the LAr where drifting electrons are produced. Furthermore, the missing trans-
 540 verse energy can be obtained by subtracting the total energy of the known particles,
 541 which contributes to the analysis of neutrinos and new particles.

542 At -184 °C where the argon exists in liquid form, the calorimeter is kept as the

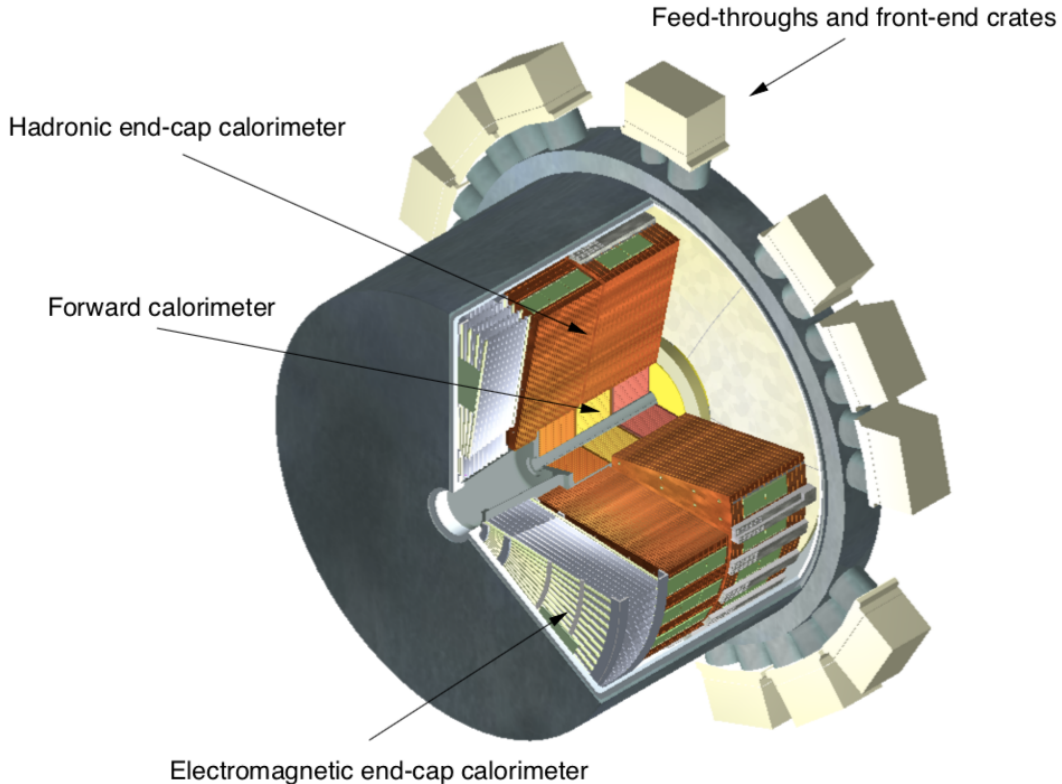


Figure 3.6 Cut-away view of an end-cap cryostat of the ATLAS calorimeter system.

543 cables that transverse electronic signals are sealed in vacuum and connected to the
 544 warmer area where located the readout system.

545 **The hadronic calorimeter**

546 Surrounded the EM calorimeter, lies the tile hadronic calorimeter where hadrons
 547 that contain strong force thus could not fully deposit their relatively large energy in
 548 the EM calorimeter are absorbed by the tile calorimeter. Steel and plastic scintillat-
 549 ing tiles are placed in layers in order to record the trajectories of incoming particles
 550 as hadronic showers are formed by the interactions of the particles with the ma-
 551 terials and emitting particles continue interacting with materials in the hadronic
 552 calorimeter and more particles are produced in steel layers. On the other hand,
 553 photons are produced by the plastic scintillators where electric currents are gained
 554 according to the energy of the particle.

555 By enveloping the EM calorimeter, a hadronic shower that contained EM showers
 556 can be fully absorbed by the great thickness in the hadronic calorimeter. Around

557 420 thousands of plastic scintillator tiles are placed in sync, leading a weight of
 558 2.9 thousands tonne in total.

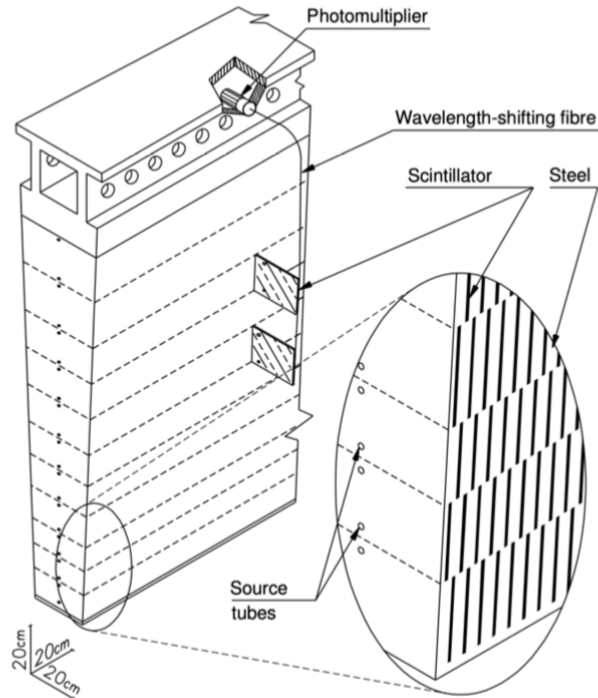


Figure 3.7 A schematic view of a tile calorimeter components of optical readout tiles and scintillating tiles.

559 As illustrated in Figure 3.7, photomultiplier tubes (PMT) are placed around the
 560 outer radii of the tile calorimeter and connected with wavelength-shifting fibres
 561 by which scintillation light is transferred. Projective geometry is designed for
 562 the whole readout system as the energy of most hadronic showers is deposited in
 563 the first or last two layers. Though the coarser granularity of the readout cells
 564 of hadronic calorimeter has been compared to the EM calorimeter, the hadronic
 565 calorimeter is qualified for the measurement of transverse momentum and jet re-
 566 construction.

567 In the forward regions, the hadronic calorimeters are integrated with LAr calorime-
 568 ters due to higher radiation exposition compared to the barrel regions. There are
 569 two calorimeters that were developed to tackle such issue: the hadronic end-cap
 570 calorimeter (HEC) that covers $1.5 < |\eta| < 3.2$ and the forward calorimeter (FCal)
 571 that covers $3.1 < |\eta| < 4.9$.

572 The HEC located further beside the EM end-cap calorimeter has two wheels in
573 each end-cap. LAr is used for filling up 8.5 mm between copper layers in the HEC,
574 by which the active medium is provided. The readout electrodes are provided in
575 separate drift zones in order to secure the stability of the whole system. The FCal
576 has three wheels placed alongside the z-direction: one electromagnetic layer (FCal
577 1) and two hadronic layers (FCal 2 and FCal 3). LAr is also used as an active
578 medium in all of the layers. As for the absorber, copper is employed in FCal 1 as
579 it has heat removal properties. Tungsten is used in both FCal 2 and FCal 3 in order
580 to constrain the lateral spread of hadronic showers.

581 **3.2.3 Muon spectrometer**

582 The muon spectrometer (MS), specially designed for the muon detection is located
583 in the outermost section of the ATLAS in order to provide sufficient measurement of
584 high-momentum muons which are almost "invisible" to the ID and calorimeters due to
585 little energy deposit when traveled through them. By deflecting the trajectories of
586 muons, the MS employs the magnetic field by a barrel toroid magnet system in $|\eta| < 1.4$
587 and end-cap toriod systems in $1.6 < |\eta| < 2.7$.

588 Four subsections of the MS: add up to 4000 separate muon chambers. Thin Gap
589 Chambers (TGC) and Resistive Plate Chambers (RPC) account for triggering and the
590 second coordinate measurement of muons. TGC is set at the end of the detector whereas
591 RPC which provides 5,000 V/mm electric field is placed in the central region. Monitored
592 Drift Tubes (MDT) is designed for the curve of muon tracks measurement with fine tube
593 resolution of 80 μm . Cathode Strip Chambers (CSC) accounts for measuring coordi-
594 nates precisely located at ends of detector with a fine resolution of 60 μm . Figure 3.8
595 demonstrates the MS with all four subsections. In total three separate points within the
596 muon trajectory are measured to reconstruct the momentum of the muon.

597 **3.2.4 Trigger and data acquisition**

598 At the LHC, approximately 1.7 billion proton-proton collisions occur per second at
599 an integrated luminosity of 140 fb^{-1} . However, many of these collisions are unlikely to
600 produce characteristics of interest. As a result, large numbers of events can be discarded
601 without affecting the search for new physics. The trigger and data acquisition systems
602 are introduced to eliminate the irrelevant data so that only events of suitable quality and

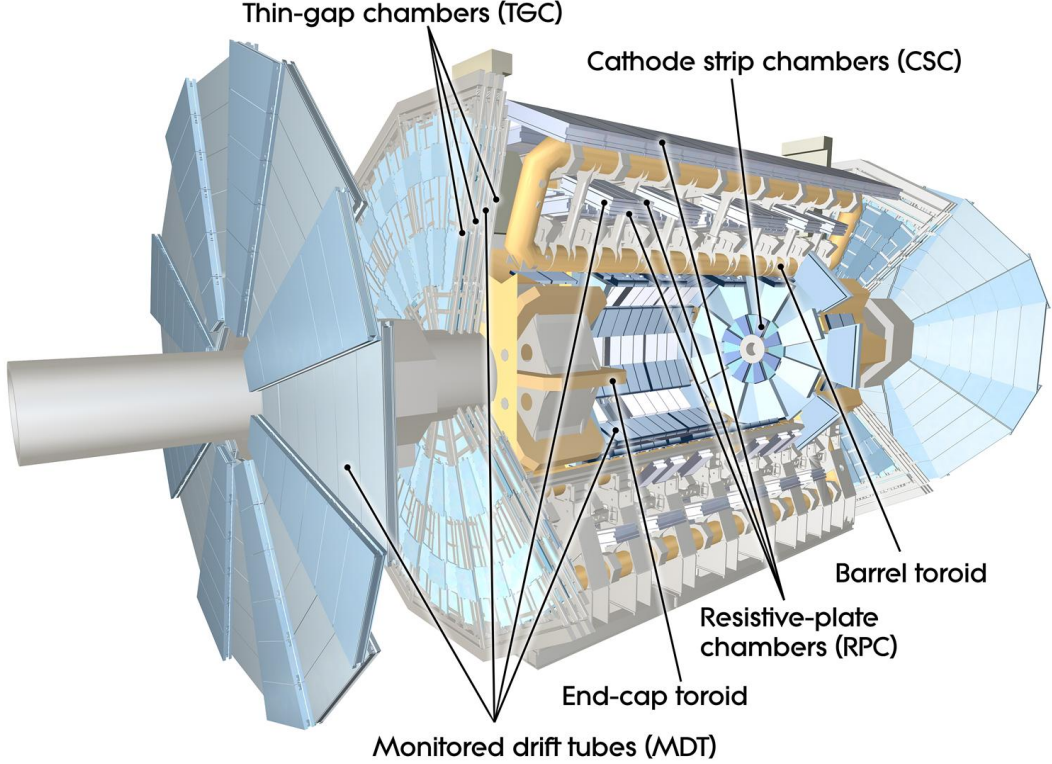


Figure 3.8 Cut-away view of the ATLAS Muons Spectrometer with subsections labeled.

603 quantity are recorded.

604 During the year of 2015-2018, the trigger system in ATLAS selected significant
 605 events in a two staged process, as illustrated in Figure 3.9: The first-level (L1) trigger is
 606 implemented on hardware, and reduced event rates from 40 MHz to 100 kHz in less than
 607 $2.5 \mu\text{s}$ right after the data happened. Working with the electrical information provided
 608 by the calorimeters and the MS, the L1 trigger employs custom-made electronics to filter
 609 and store the events in the readout sections as buffers before passing them to the High-
 610 Level trigger (HLT) [22]. Certain physics objects such as photons, jets and leptons are
 611 identified in the L1 trigger, in which energy depositions of electrons and photons in the
 612 EM calorimeter and jets in the hadronic calorimeter are provided. Information of tracks
 613 in high-momentum muons is recorded in the layers of the MS and forwarded to the L1
 614 trigger.

615 The events are further reduced from 100 kHz to 1 kHz in merely 250 microseconds
 616 by the second level trigger: HLT. Based on the offline software, the HLT utilize fast
 617 selection algorithms to analyse and reject events in the early stage, resulting in better

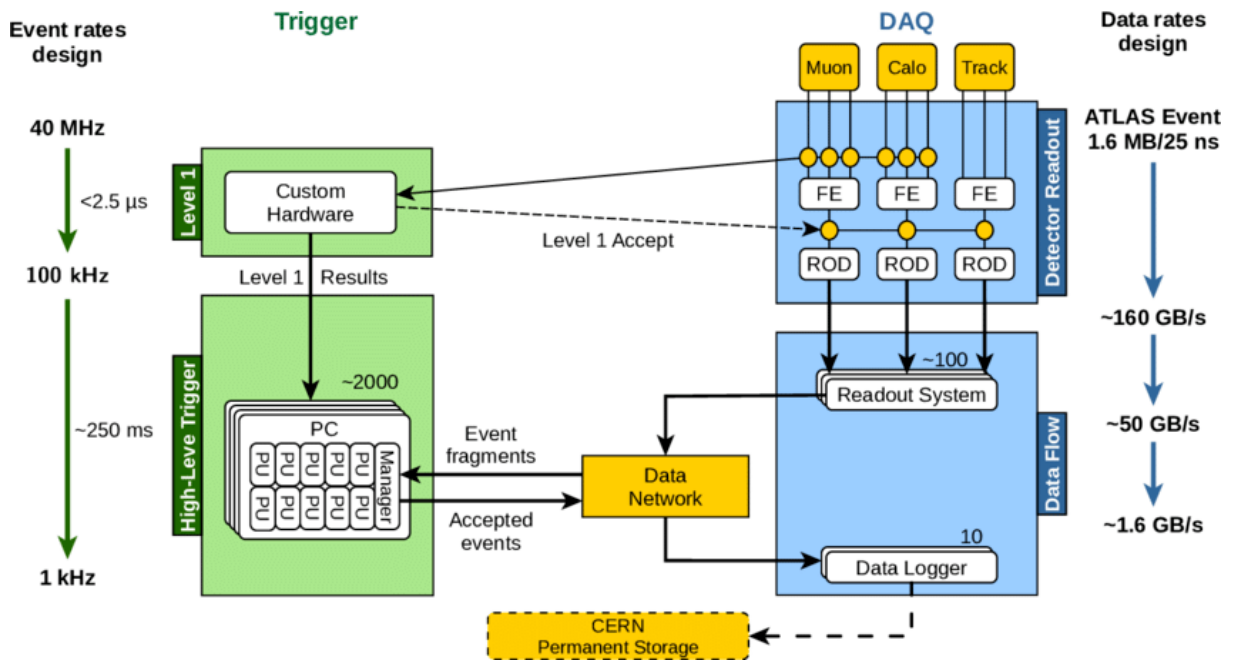


Figure 3.9 illustration of the ATLAS Run 2 trigger and data acquisition system.

precision and intense CPU usage of about 1.6 GB per second. The accepted data from the HLT will be passed to permanent storage at CERN via Data Logger [31].

4 Jets in ATLAS

In the LHC, a large number of quarks and gluons are produced during the inelastic proton-proton collisions, resulting in jets. These collimated outcome particles are hadronised because of colour confinement in the QCD process. As a result of this, only colour-neutral jets clustered by particles can be seen in the detector.

The information of jets is crucial to most of the analysis such as the measurements of the SM particles and searches for the BSM phenomena. Good qualities of jets, for example the high efficiency of jet reconstruction, jet energy calibration including energy scale and energy resolution, are thus important to the analysis.

4.1 Jet reconstruction

Jets are defined in two way: Monte Carlo (MC) simulated jets at particle level and detector level jets with the information from the ID and calorimeters. The production and hadronisation processes of jets are illustrated in Figure 4.10.

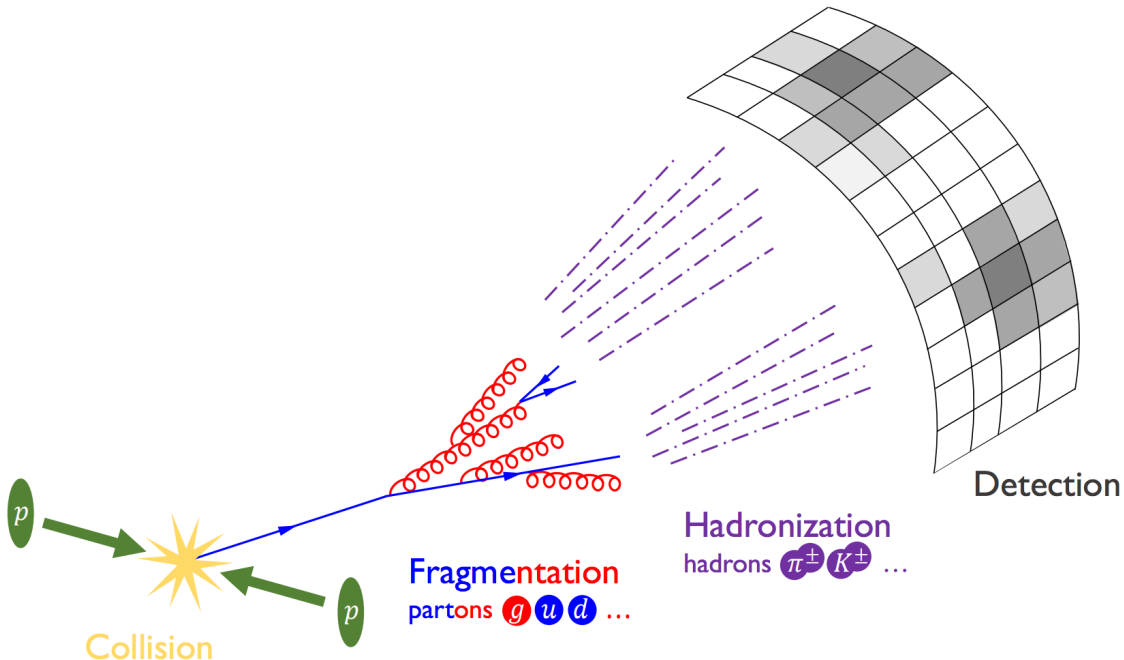


Figure 4.10 illustration of jets produced by pp collision and hadronised before seen by the detector.

Jets from the MC simulation are defined as truth-particle jets which have lifetimes

longer than 10 ps as stable particles. Truth-particles indicate the ideal measurement from a detector under perfect-condition and high resolution without defects or the effects from pile-up (background interactions per bunch-crossing in the LHC). Whereas track jets are constructed with the use of charged information in the ID, and calorimeter jets with the use of energy information in the calorimeters.

There are several types of jets aim for different analysis depended on the constituents and algorithm used for reconstructing the jets. ATLAS previously used topo-cluster jets, which is a group of topological related cells in calorimeter with significantly high energy deposits. A pile-up suppressed algorithm is applied to select certain cells with low noise. Cell above certain signal-to-noise (S/N) threshold (usually by four times its standard deviation) are used to seed the algorithm. By neighbouring the seed a topo-cluster is defined. In the hard-scatter process, jets of interest are expected to produced from the primary interaction point (known as vertex). The primary vertex is defined if there are at least two tracks with the highest sum of squared track momentum associated to it.

Jets are constructed from any set of four-vectors. EMTopo jets are the jets that use topo-cluster initially calibrated to electromagnetic (EM) scale in the calorimeters. A local cluster weighting (LCW) scale is also used for calibrating hadronic clusters by applying weights for low hadronic interaction response. Besides, particle flow (PFlow) [15] jets are built by combining the information from both the ID and the calorimeter, where the energy deposited from the calorimeter are removed by the momentum in the ID by a cell-based energy subtraction algorithm. The inputs to the particle flow algorithm are the separate topo-clusters with local energy maxima, respectively.

A recombination algorithm called anti- k_t algorithm is employed to build the jets with a radius parameter R in rapidity-azimuth ($y - \phi$) plane around a cluster. The algorithms are defined as follows:

$$d_{ij} = \min \left(k_{ti}^{2p}, k_{tj}^{2p} \right) \frac{\Delta_{ij}^2}{R^2} \quad (4.1)$$

$$\Delta_{ij}^2 = (y_i - y_j)^2 + (\phi_i - \phi_j)^2 \quad (4.2)$$

$$d_{iB} = k_{ti}^{2p} \quad (4.3)$$

660 where the distance d_{ij} between any pair of particles i and j is given by the minimum
 661 transverse momenta k_t of the two particles. The geometrical distance Δ_{ij} represents the
 662 separation of a pair of particles in $(y - \phi)$ plane. Radius parameter R indicates the size
 663 of the final jets. The distance d_{iB} between any detected particle i and the beam B is also
 664 given. Parameter p indicates the relative power of energy with respect to geometrical
 665 scales and is used to distinguish the different types of algorithms.

666 When p is set to 0, the Cambridge-Aachen (CA) algorithm is given as the dis-
 667 tance d_{ij} and d_{iB} only based on spatial separation and are independent of the transverse
 668 momenta. This algorithm is usually used for large-radius jets and jet substructure per-
 669 formance study.

670 For the k_t algorithm, p is set to 1 so that the distance d_{ij} is dominated by the min-
 671 imum k_t . This algorithm is preferred for clusters that are soft and collinear splits are
 672 merged first, resulted in irregular footprint with the most interesting splits.

673 The algorithm [39] on the other hand set $p = -1$, leaving the distance $d_{ij} \propto \min\left(\frac{1}{k_{ti}^2}, \frac{1}{k_{tj}^2}\right)$
 674 shorten as the transverse momenta of two particles increase. This is widely used in the
 675 LHC for hard clustering as it is less vulnerable to the effects from the pile-up and resulted
 676 in circular footprint as shown in Figure 4.11 for $R = 1.0$.

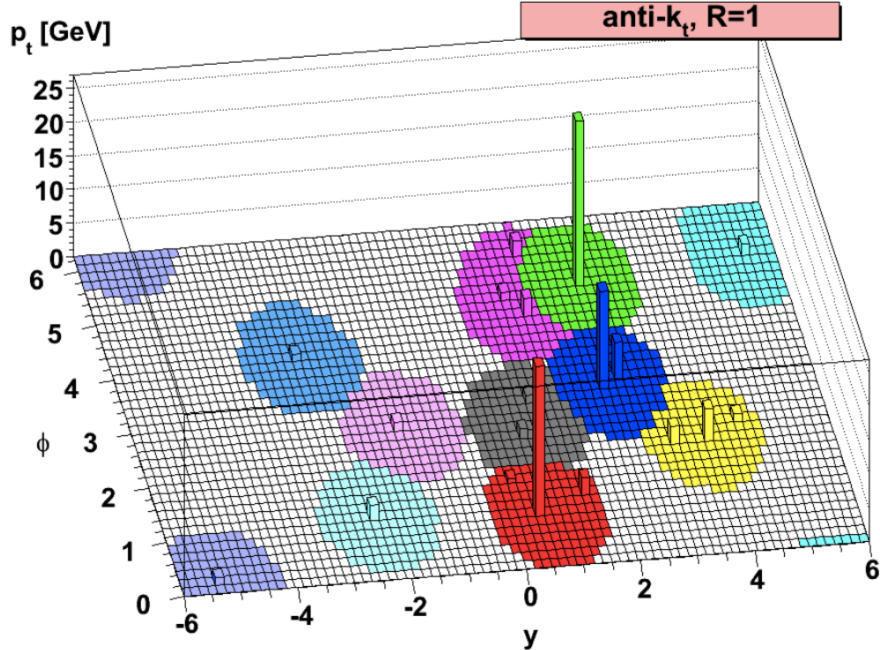


Figure 4.11 Plot of parton-level jets clustered using algorithms with radius parameter set to 1.

677 For most of ATLAS analysis, jets with $R = 0.4$ are used for quarks and gluons

analysis. Other ones such as $R = 1.0$ are also widely used to study energetic particles like W and Z bosons. $R = 0.2, 0.6, 1.2, 1.5$ and variable radii are also analysed.

The $R = 0.4$ PLow jets are used in the quark/gluon taggers calibration described in this thesis.

4.2 Jet calibration and cleaning

The motivation of jet calibration [13, 14] is to correct the translation from received signals to initial partons for several detector effects, including energy deposited in dead or beyond areas in the detectors, low response to hadronic reactions, pile-up, radiations that outside jet cone, etc. The calibration process is thus needed to account for the energy of jets to that of MC simulated jets at particle-level.

Calibration is performed to topological clusters at the EM scale where the sum of the energies in all constituent cell are taken, or at the LCW scale where low hadronic response in the ATLAS calorimeters is taken into account. The diagrams 4.12 shows the calibration scheme for small- R jets.

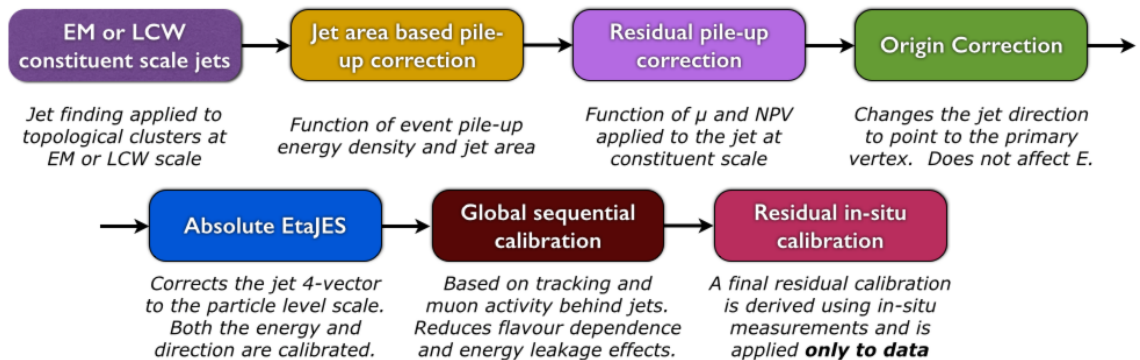


Figure 4.12 Overview scheme of jet calibration in the ATLAS.

4.2.1 Pile-up corrections

In order to eliminate a great amount of energy deposits from pile-up, a jet area-based subtraction of pile-up contribution to the p_T of each jet per event is applied as the start of the calibration chain.

After all pile-up corrections are applied, the jet p_T is given by:

$$p_T^{\text{corr}} = p_T^{\text{reco}} - \rho \times A - \alpha \times (N_{\text{PV}} - 1) - \beta \times \mu \quad (4.4)$$

where p_T^{reco} indicates the reconstructed jet p_T before any pile-up correction is applied. The jet area A is defined by certain number of ghost tracks associated with a jet after clustering thus can quantify the liability of a jet to pile-up. The pile-up p_T density ρ is used to evaluate the contribution from pile-up in the y - ϕ plane. To calculate the density ρ of each jet in the distribution p_T/A , a k_t algorithm with radius $R = 0.4$ is employed to reconstruct jet from positive-energy topo-clusters within the range of $|\eta| < 2$. The calculation of ρ performed in such η range for pile-up measurement is due to the fact that ρ tend to be zero beyond $|\eta| \approx 2$ as a result of lower occupancy in coarser segmentation in the forward region. Therefore, pile-up sensitivity in the forward region is not fully described after such correction.

An additional residual correction is thus applied from the MC simulation to account for the difference between the reconstructed jet p_T and truth jet p_T as a function of the number of reconstructed primary vertices in the event N_{PV} and the mean number of interactions per bunch crossing μ , which are sensitive to in-time and out-of-time pile-up, separately.

Both the initial values of α and β coefficients are derived in bins of truth jet p_T and geometric centre of the detector $|\eta_{\text{det}}|$. A logarithmic dependence on truth jet p_T is observed.

4.2.2 Jet energy scale and η calibration

Following the pile-up mitigation, the absolute jet energy scale and η calibration are introduced to correct the four-momentum of the reconstructed jet to the truth-particle jets, accounting for defecting calorimeter response, energy losses when particles passed through certain materials, boundary effects and biases in the reconstructed jet in different η due to the transition between the granularities and technologies changes in calorimeter.

Since the detector responses differ across the detector η range, the reconstructed jets are thus divided into small bins of η_{det} and the energy of the truth jet E^{truth} as the response distribution for fixed E^{truth} is Gaussian. The average jet energy response \mathcal{R} is defined as $E^{\text{reco}}/E^{\text{true}}$ using the mean of a Gaussian fit in η_{det} and E^{truth} bins, and is further parameterized as a function of E^{reco} . Such response for PFlow jets is higher than that for EMtopo jet at low energies as the tracking information is considered.

Besides Jet energy scale (JES) correction, the bias from the η of the reconstructed jet to that of the truth jet is taken into account. The bias is defined as a significant devi-

729 ation from zero in the signed difference between the reconstructed jet η^{reco} and truth jet
 730 η^{truth} , separately. Then a second correction is applied as such difference is parameterized
 731 as a function of η_{det} and E^{truth} .

732 The calibration is derived as a function of energy and η from the MC samples which
 733 do not have the effects from pile-up, and only correct the jet p_T and η instead of full four-
 734 momentum. The EMtopo and PFlow jets after full JES and η calibration are regarded as
 735 EM+JES scale and PFlow+JES scale, respectively. Small non-closures beyond $|\eta_{det}| \approx$
 736 3.2 in the calibration are seen due to approximate treatment of hadronic showers in the
 737 forward region, lead to an additional systematic uncertainty.

738 4.2.3 Global sequential calibration

739 The global sequential calibration (GSC), based the global jet observables such as
 740 the fraction of jet energy measured in the different layer of hadronic and the EM
 741 calorimeters, the tracking information associated with the jets, and the number of muon
 742 track segment. For each observable, a series of multiplicative corrections are applied on
 743 the four-momentum as a function of p_T^{truth} and $|\eta_{det}|$. Considered any observable x , the
 744 correction is derived from the inverted jet response \mathcal{R} :

$$C(x) = \frac{\mathcal{R}^{-1}}{\langle \mathcal{R}^{-1}(x) \rangle} \quad (4.5)$$

745 where $\langle \mathcal{R} \rangle$ is the average jet response.

746 As a result, the fluctuations in the jet particle composition are reduced and the jet
 747 resolution can be improved without changing the average jet energy response which
 748 depends on the flavour and the energy distribution of the constituent particles. The shape
 749 of a jet varies between quark- and gluon-initiated jets as hadrons are often included in a
 750 quark-initiated jet with higher fraction of the jet p_T with higher calorimeter response.

751 After applied GSC for PFlow jet, the average jet p_T response on each observable is
 752 reduced to lower than 2% with small deviations from correlations between observables.

753 The fractional jet resolution $\sigma_{\mathcal{R}}/\mathcal{R}$ is derived from the jet resolution $\sigma_{\mathcal{R}}$, which is
 754 defined by the standard deviation of a Gaussian fit to the distribution of jet p_T response.
 755 This fractional jet resolution is used to determine the size of the fluctuations in the jet
 756 energy reconstruction.

757 **4.2.4 Residual *in situ* calibration**

758 The final step of the jet calibration is performed only in data to account for the
759 differences of jet response measurement in data and the MC, the derived ratio of it is
760 used as a correction in data. The differences are introduced by the inadequate nature of
761 the detector materials and the imperfect simulation of the real physics processes. Such
762 differences can be quantified by weighting the p_T of a jet to other reference objects that
763 are well-measured. The correction factor can be denoted as follows:

$$c = \frac{\mathcal{R}_{\text{in situ}}^{\text{data}}}{\mathcal{R}_{\text{in situ}}^{\text{MC}}} \quad (4.6)$$

764 the response $\mathcal{R}_{\text{in situ}}$ represents the average ratio of the jet p_T to the reference object
765 p_T in bins of reference object p_T , where the average value is founded from peak value
766 of a Gaussian fit to the distribution. The double ratio is robust to secondary effects thus
767 more reliable in term of the measurement of jet energy.

768 Three stages are carried out in such *in situ* calibration. First, η -intercalibration is
769 performed on the energy scale of forward jets ($0.8 \leq |\eta_{\text{det}}| < 4.5$) to match the central jets
770 ($|\eta_{\text{det}}| < 0.8$) using the jet p_T in dijet events. Then $Z+\text{jet}$ and $\gamma+\text{jet}$ analyses balance the
771 measurement of p_T response of a well-calibrated Z boson or photon. Finally, a multijet
772 balance (MJB) analysis is employed to calibrate low- p_T jets to a very high- p_T jet. Both
773 MJB and $Z/\gamma+\text{jet}$ analyses are used only for jets in the central region ($|\eta| < 1.2$). All
774 three *in situ* calibrations are done sequentially so that the systematic uncertainties can be
775 propagated from each to the next. The systematic uncertainties in each calibration pro-
776 cess come from three sources: the MC modelling of physics processes, the uncertainties
777 in the measurement and from topology obtained by different event selections.

778

5 The calibration of quark/gluon jets taggers

779 The classification of jets originated from a quark or a gluon is useful for improving the
780 SM measurements and searches for BSM physics at the LHC. According to the QCD,
781 gluons are in the adjoint representation of the $SU(3)$ gauge group thus carry both colour
782 and anti-colour quantum numbers, whereas quarks are in the fundamental representation
783 and have only a single colour number [7]. As a result, a gluon-initiated jet (gluon-jet)
784 tend to have more constituents and a broader radiation pattern than a quark-initiated jet
785 (quark-jets).

786 The manifestation of colour charges is intrinsic to quarks and gluons; however,
787 the confinement phenomenon inherent in QCD theory indicates that only colour neutral
788 hadrons can be observed in the detector. Such principle brings significant challenges
789 for the identification of quark- or gluon-jets in ATLAS. The identification method relies
790 on the number of charged tracks within the jets and the reconstruction algorithm for
791 it. The calibration described in this paper demonstrates the measurement of the tagging
792 efficiencies of the aforementioned jet taggers. The more advanced boosted decision tree
793 (BDT) algorithm is employed to constructed the jet tagging variable based on the charge
794 multiplicity inside jets. A matrix method is established with the use of quark/gluon
795 fraction in quark-/gluon-enriched subsamples, defined by the pseudorapidity of jets. The
796 scale factors extracted from the difference between data and simulation are provided
797 for tagger working points corresponding to 50%, 60%, 70% and 80% fixed quark-jet
798 efficiencies for both quark- and gluon-jets, respectively.

799 In addition to earlier investigations that concentrated on single-variable taggers
800 within a lower p_T range [16, 23], this research emphasizes the development of a novel
801 q/g tagger that incorporates multiple jet substructure parameters. Additionally, it aims
802 to expand the application of q/g tagging to a broader energy spectrum.

803 **5.1 Data and Monte Carlo samples**

804 **5.1.1 Data**

805 The data recorded in 2015-2018 with integrated luminosity of 140 fb^{-1} (full Run 2
806 data)[17] is used in this study. The data samples are processed through the un-skimmed
807 DAOD_JETM1 derivation scheme in order to obtain multi-jet events. The lowest un-

prescaled small- R single-jet trigger is employed for this analysis. The jet p_T threshold for the trigger in this analysis is 420 GeV, keeping the selection consistent across years, together with additional requirements that ensure events of good qualities are used [11].
 The additional selections are:

- Good Run List (GRL): Make sure a steady state of all relevant detectors so that physics processes recorded by them are good.
- LAr: Liquid Argon Calorimeter error rejected.
- Tile: Tile Calorimeter error rejected.
- SCT: SCT single event upsets rejected.
- Core: Incomplete event build rejected.
- Primary Vertex: the highest $\sum p_T^2(\text{trk})$ vertex has at least two tracks associated with it
- Trigger: Passes the lowest unprescaled single-jet trigger, HLT_j420

Additional kinematic selection criteria are discussed in Section 5.2.

5.1.2 Monte Carlo simulation

For this calibration, multi-jet events are generated and modelled with several MC simulations, processed through the same DAOD_JETM1 derivation scheme. For the nominal result, PYTHIA 8.230 [79] MC generator is used with leading-order (LO) matrix element (ME) for dijet production. Parton density functions (PDFs) are considered for systematic uncertainties evaluation as the PDF set [74] is used for PYTHIA 8.230 with the A14 tune [12]. Alternative samples with different choices of parton shower modelling, ME generation, and the simulation of the multi-parton interactions are included to estimate the systematic uncertainties.

Two set of MC samples generated using SHERPA 2.2.5 [35] are used with the same ME for the (2→2) process at LO, to provide the uncertainties of hadronisation modelling [77, 83]. The CT10 PDF [55] sets are included in both SHERPA samples where one based on the cluster hadronisation whereas the other used SHERPA interface to the Lund string fragmentation [78] model as PYTHIA 8.230.

836 Two set of MC samples generated using HERWIG 7.1.3 [34] are used for parton
 837 shower uncertainties as one uses angular ordering shower whereas the other one uses
 838 dipole shower. These samples are produced at next-to-leading order (NLO) with a PDF
 839 set of MMHT [61].
 840

841 Another set of multijet samples that produced with POWHEG [72, 57, 4] interfaced
 842 to PYTHIA at NLO accuracy is employed with NNPDF2.3 LO PDF [80] set, to estimate
 843 the effects from the ME uncertainty as different perturbative scales in the ME and parton
 844 distribution functions are included. The renormalization and factorisation scales are set
 845 to the p_T of the underlying Born configuration. These samples included different pertur-
 846 bative scales in the ME and parton distribution functions are used for the estimation of
 ME uncertainty.
 847

A list of the MC samples used is given in table 5.1.

PDF set	Generator	Cross-section	Parton shower	Hadronisation
NNPDF2.3	PYTHIA 8.230	LO	p_T -ordered	String
CT10	SHERPA 2.2.5	LO	p_T -ordered	Cluste
CT10	SHERPA 2.2.5	LO	p_T -ordered	String
MMHT	HERWIG 7.1.3	NLO	Dipole	Cluster
MMHT	HERWIG 7.1.3	NLO	Angular-ordered	Cluster
NNPDF2.3	Powheg+PYTHIA	NLO	p_T -ordered	String

Table 5.1 The MC simulation used for the multi-jet processes in this calibration. The PDF sets, generators for a hard process, the order in α_s of cross-section calculations and the simulator of parton showers, and hadronisation are shown.

848 5.2 Object and Event selection

849 In order to perform the calibration of the quark-/gluon-jet tagger, it is requisite to
 850 establish two distinct subsamples. One subsample should be predominantly composed of
 851 quark-jets, called quark-enriched sample, while the other should predominantly consist
 852 of gluon-jets, as gluon-enriched sample. These subsamples are gained from the dijet
 853 events. This section describes the reconstruction and selection of jet objects used in this
 854 calibration, as well as the approach to construct quark- and gluon-enriched subsamples.
 855

855 **5.2.1 Physics object definition**

856 The PFlow jets that are reconstructed with the algorithm with a radius parameter
 857 R set to 0.4. An overall jet energy calibration described in section 4.2 has been done
 858 to rectify residual detector effects and pile-up. In order to ensure a good quality jet, an
 859 event-based jet cleaning with standard loose cut is applied to reject events with flawed
 860 leading or subleading jet.

861 Tracks that reconstructed [21] from the ID are required to have $p_T > 500$ MeV, and
 862 within the ID range $|\eta| < 2.5$. Additional criteria such as primary vertex are required to
 863 ensure selected tracks originating from the collision and prevent the mis-reconstructed
 864 tracks from pile-up hits in the detector. The alignment of tracks with calorimeter-based
 865 jets is executed through the application of the ghost-association technique. This entails
 866 a repetition of the jet clustering procedure augmented by the inclusion of 'ghost' repre-
 867 sentations of registered tracks [37]. These ghost tracks share the same direction as their
 868 actual counterparts but possess an infinitesimally small p_T , thereby ensuring that they do
 869 not induce any alterations to the intrinsic characteristics of the calorimeter-based jets. A
 870 criterion for track-jet correspondence is established: a given track is associated to a jet if
 871 its corresponding ghost track is contained in the jet after reclustering.

872 Jet reconstructed from the simulated MC is known as "truth jets" [13], with the
 873 same $R = 0.4$ algorithm as PFlow jets. Geometric correspondence between truth jets
 874 and PFlow jets is established via angular proximity, adhering to the criterion $\Delta R < 0.4$.
 875 Each truth jet is bestowed with a flavour label, referred to as a truth label [16, 23]. The
 876 truth flavour label attributed to a jet is defined by the flavour of the highest-energy parton
 877 situated within a cone of size $\Delta R < 0.4$ around the jet's axis, prior to the process of hadro-
 878 nisation in the parton shower. Following this definition, jets arising from the splintering
 879 of gluons into b - or c -quark pairs are labelled as heavy flavour jets. These heavy flavour
 880 jets are often identifiable by the long-lived or leptonically decaying hadrons. Therefore,
 881 no distinct discriminant tailored for heavy-flavour quarks is investigated within the cur-
 882 rent framework [40, 19]. Jets will be unlabelled if there is no corresponding truth parton
 883 with $p_T > 1$ GeV is found within the cone surrounding the truth jet. These instances of
 884 unlabelled jets commonly emerge as a consequence of pile-up effects, and less than 1%
 885 of the dataset used. They are thus ignored [20].

5.2.2 Event Selection and definition of quark and gluon-enriched samples

Events are chosen by the single-jet trigger, HLT_j420. The jet p_T is required to be greater than 500 GeV, as more quark-jets and better resolution on the jet constituents are given. Only the leading two jets with the highest p_T are used, as dijet events, and are required to be $|\eta| < 2.5$ so that their charged constituents are collected within the coverage of the ID. To maintain the equilibrium in p_T and suppress non-isolated jets, a criterion demands that the ratio of the p_T of the leading jet to that of the sub-leading jet remains within 1.5. The two leading p_T jets serve as the cornerstone for the formulation of quark-enriched and gluon-enriched subsamples.

The quark-enriched sample is derived from the jet with higher $|\eta|$ among the leading two jets, while the gluon-enriched sample is extracted from the jet with lower $|\eta|$. This selection strategy capitalizes on the intrinsic behaviour of PDFs at higher proton momentum fraction range, where there exists a higher likelihood of encompassing valence quark-jets. Consequently, jets situated in more forward regions (higher $|\eta|$) have a higher probability of being quark-jets, while jets positioned closer to the central region (lower $|\eta|$) manifest an increased likelihood of corresponding to gluon-jets [18].

Selection	Multi-jet sample
Trigger	HLT_j420
Number of jets	≥ 2
$p_T(j_1)$	> 500
$p_T(j_2)$	> 500
$p_T(j_1)/p_T(j_2)$	< 1.5
$ \eta(j_1) $	< 2.1
$ \eta(j_2) $	< 2.1
Target parton	Quark(Higher $ \eta $) or Gluon (Lower $ \eta $)

Table 5.2 The selections to retrieve quark/gluon-enriched samples. " j_i " represents the i -th jet in p_T -ordering.

The distribution of leading and subleading jets p_T in dijet event after selections is shown in Figure 5.13 for both MC and data.

5.3 Quark/gluon tagging variables

According to QCD, the colour factor of gluons is larger than that of quarks by factor 9/4 ("Casimir ratio") [7], which makes gluons emit more particles in the hadronisation

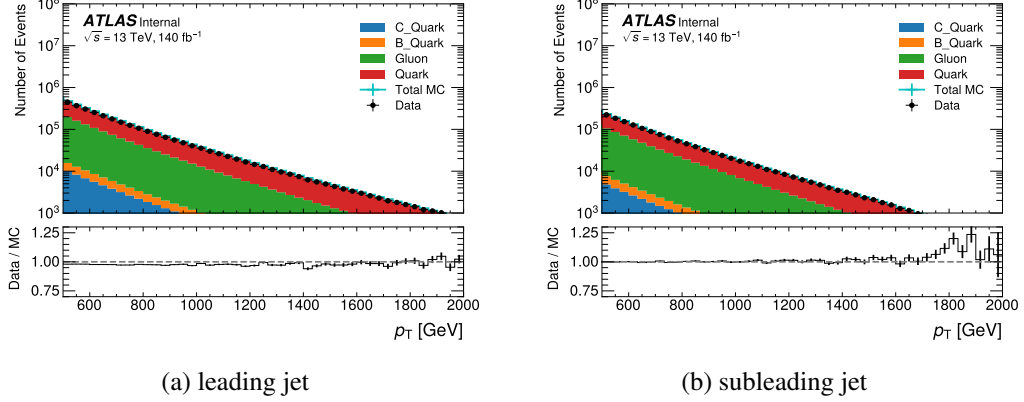


Figure 5.13 The p_T distribution of the leading jets and sub-leading jets with PYTHIA samples for dijet event.

than quarks. As a result, a gluon-initiated jet has more charged multiplicity associated and its width is larger than that of a quark-initiated jet. Therefore, the information of the track multiplicity inside a jet is crucial to distinguish quarks from gluons.

The q/g tagging variables used in this study are based on the track multiplicity and are specified as : number of tracks (N_{trk}), jet width (W_{trk}) [16, 67], and two point energy correlation function ($C_1^{\beta=0.2}$) [70, 68] computed from the associated tracks. The expressions are defined as follows:

N_{trk}

N_{trk} is a number of tracks associated with the jet.

$$N_{\text{trk}} = \sum_{\text{trk} \in \text{jet}} \quad (5.1)$$

W_{trk}

W_{trk} is a track- p_T -weighted width of the jet divided by the scalar sum of track transverse momenta. It is defined as

$$W_{\text{trk}} = \frac{\sum_{\text{trk} \in \text{jet}} p_{T,\text{trk}} \Delta R_{\text{trk},\text{jet}}}{\sum_{\text{trk} \in \text{jet}} p_{T,\text{trk}}}, \quad (5.2)$$

where $p_{T,\text{trk}}$ is a p_T of a charged track reconstructed by the ID and $\Delta R_{\text{trk},\text{jet}}$ is a distance in the $\eta - \phi$ plane between the track and the jet axis.

$C_1^{\beta=0.2}$

922 Two point energy correlation function is defined as

$$C_1^{\beta=0.2} = \frac{\sum_{i,j \in jet}^{i \neq j} p_{T,i} p_{T,j} (\Delta R_{i,j})^{\beta=0.2}}{\left(\sum_{trk \in jet} p_{T,trk} \right)^2}, \quad (5.3)$$

923 where i and j denote tracks associated with the jet and the sum runs over all the
 924 combination of two tracks. The β is fixed to 0.2, which is known to be suitable for
 925 q/g tagging.

926 **5.3.1 The BDT tagger**

927 Multivariate Analysis (MVA) is a technique introduced to discriminate signal from
 928 background, one type of classification algorithm in MVA is the BDT. A tree structure is
 929 built to classify datasets through a sequence of branching binary decisions. Data with
 930 desirable features is kept by discriminating algorithm whereas others are rejected. Each
 931 decision point made construct a node at each level of the decision tree, and a score is
 932 assigned to every classifier that goes into the boosting process based on its error rate.
 933 One decision node can have two or more branches to split the datasets. Such procedure
 934 is iterated from top to down so that a termination condition such as the minimum number
 935 of samples in a node or a maximum depth in a tree depth is met. A diagram of a single
 936 decision tree is shown in Figure 5.14. After all series of cuts are applied, the BDT is
 937 defined. Therefore, a cut based on the BDT score can be employed as the most correct
 938 classification of datasets.

939 The BDT tagger is constructed by the combination of tracking-related observables:
 940 N_{trk} , W_{trk} , $C_1^{\beta=0.2}$ and p_T of a jet are included as the distribution of the track multiplicity
 941 is affected by them. In this study, the BDT score is used to classify quark- or gluon-jets
 942 from the multi jet samples, with the truth-labelled information from MC to train until a
 943 quark signal efficiency larger than 90% is reached.

944 The BDT tagger is trained using the LGBMClassifier from lightGBM [64] frame-
 945 work, and hyper-parameter tuning is performed with Optuna [3]. The MC PYTHIA sam-
 946 ples are employed.

947 An individual score is allocated to each BDT within the boosting procedure, factor-
 948 ing in its error rate. This BDT score serves as the criterion for classifying a given jet as
 949 either a quark-jet or a gluon-jet.

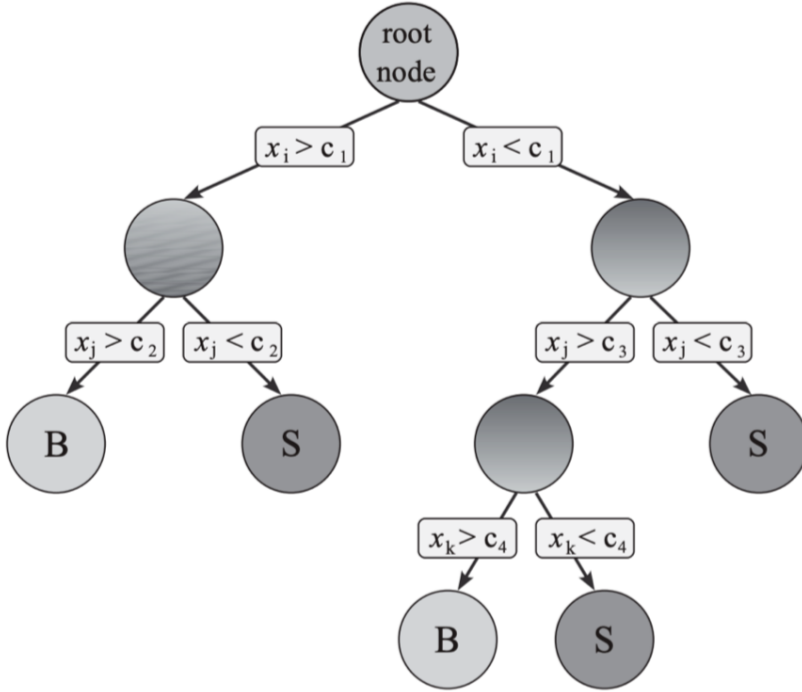


Figure 5.14 A scheme of a single decision tree with a depth of three

5.3.1.1 Feature selections

Drawing upon the features employed during the training process, an exploration of the correlation matrix is undertaken to assess the interdependence among jet attributes, including p_T , $|\eta|$, and jet substructure variables N_{trk} , W_{trk} , $C_1^{\beta=0.2}$, and the BDT. Figure 5.15 shows N_{trk} , W_{trk} and $C_1^{\beta=0.2}$ exhibit notable interrelationships among themselves, displaying relatively robust correlations. In contrast, p_T and η display a diminished level of correlation. The distributions of all single jet substructure variables and BDT score with systematic uncertainty in forward and central regions are shown in Figure 5.16. The distributions of all single jet substructure variables and BDT score with systematic uncertainty of quark- and gluon-jets in different p_T ranges from the MC simulation are shown in Figure 5.17.

Rather than employing multiple BDTs for different p_T ranges, an universal BDT can be trained using events in all p_T ranges. Given the intrinsic correlation between N_{trk} and the jet p_T , a natural way to choose features is including p_T in addition to three q/g tagging variables. Concerning the remaining variable, η , two comparative scenarios are juxtaposed: one involves its inclusion, and the other pertains to its exclusion. This comparison facilitates an assessment of whether or not to incorporate $|\eta|$.

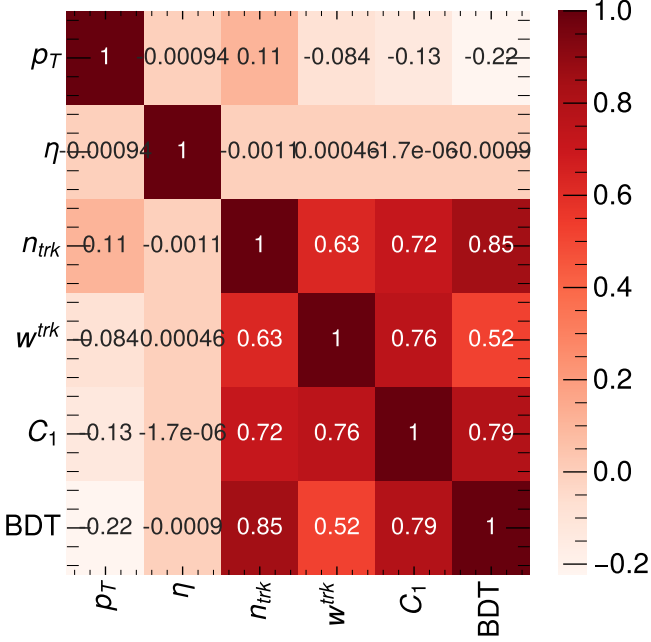


Figure 5.15 correlation matrix of jet variables.

- 967 1. p_T , N_{trk} , W_{trk} and $C_1^{\beta=0.2}$
 968 2. p_T , $|\eta|$, N_{trk} , W_{trk} and $C_1^{\beta=0.2}$

969 The result depicted in Figure 5.18 shows a distinct discrepancy when $|\eta|$ is encom-
 970 passed within the training. This violates the assumptions that the partons distribution in
 971 more forward and more central regions should not change. Specifically, the distribution
 972 of BDT scores for forward quarks substantially diverges from that of central quarks, a
 973 trend that is similarly observed for gluons. Moreover, adopting the BDT tagger that in-
 974 corporates $|\eta|$ would result in inadequate performance for jets situated within the central
 975 region when this tagger is applied to a pure sample of quark-jets (e.g., $Z+jet$ samples).
 976 In the present analysis, the BDT is endowed with the spectra of p_T , N_{trk} , W_{trk} , and $C_1^{\beta=0.2}$,
 977 as exemplified in scenario 1. At detector-level, however, the observed radiation pattern
 978 within jets no longer remains unaffected by $|\eta|$, owing to variances in the detector ma-
 979 terial and technology. To counteract this effect, a subsequent re-weighting procedure is
 980 implemented, described in Section 5.5.

981 **5.3.1.2 Training weights**

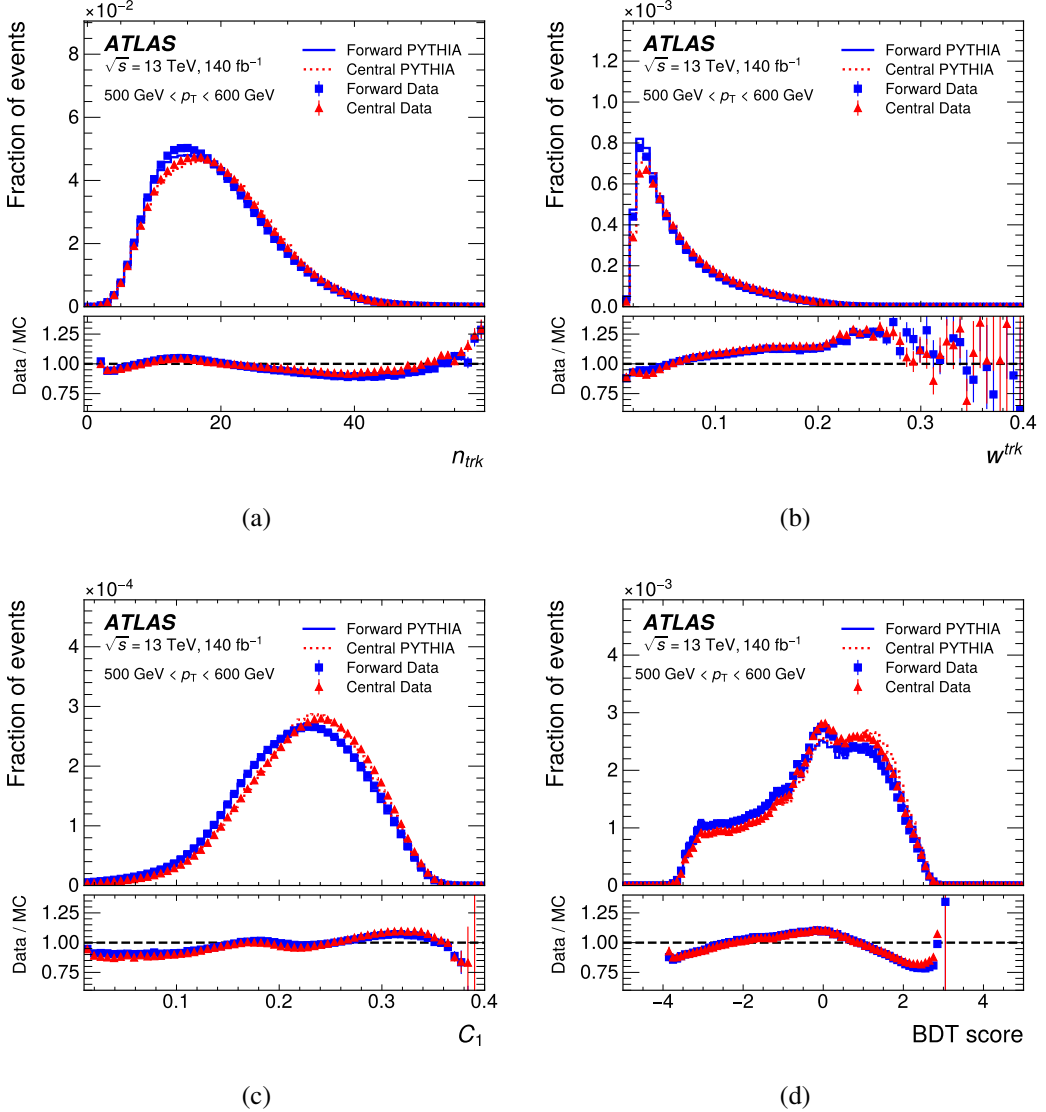


Figure 5.16 The distributions of N_{trk} (a), W_{trk} (b), C_1 (c) and BDT score (d) in the forward and central regions in data (closed symbols) and the PYTHIA MC (lines) are shown in the upper panels. The bottom panels show the ratio of the data and the MC. The distributions shown are for jet p_T in the range between 500 GeV and 600 GeV. The vertical error bars show the statistical uncertainty.

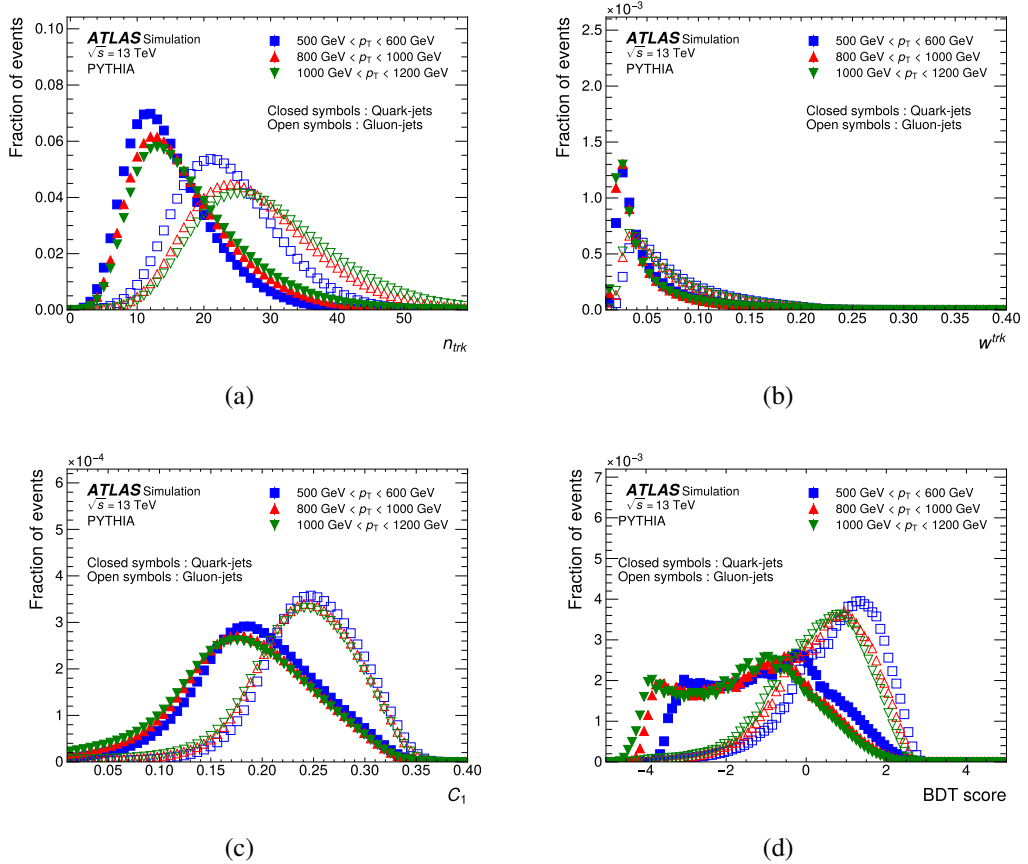


Figure 5.17 The distributions of N_{trk} (a), W_{trk} (b), C_1 (c) and BDT score (d) in the quark-jets (closed symbols) and gluon-jets (open symbols) in given p_T regions using the PYTHIA MC samples.

The calibration of quark/gluon jets taggers

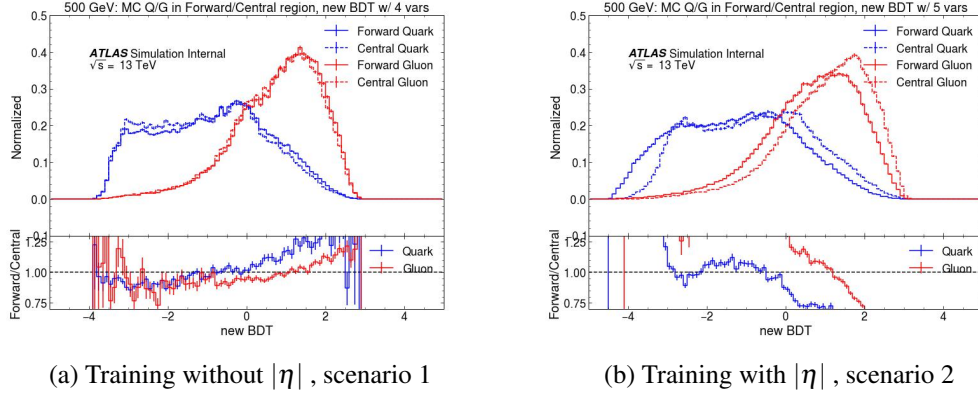


Figure 5.18 The comparison of BDT distribution for different scenarios in the jet p_T range from 500 to 600 GeV.

An additional data processing step is conducted to modify the event weights, such that a flat distribution of the p_T spectrum is given. This adjustment is motivated by the observation that higher p_T jets have less probability to occur, so the training on the higher p_T jets need to be emphasise. This newly introduced weight, referred to as the "flat p_T -weight" within this context, is exclusively employed during the training process. Conversely, for other scenarios, such as assessing tagger performance on validation datasets and subsequent calibration endeavours, the original event weights based on physical considerations remain employed.

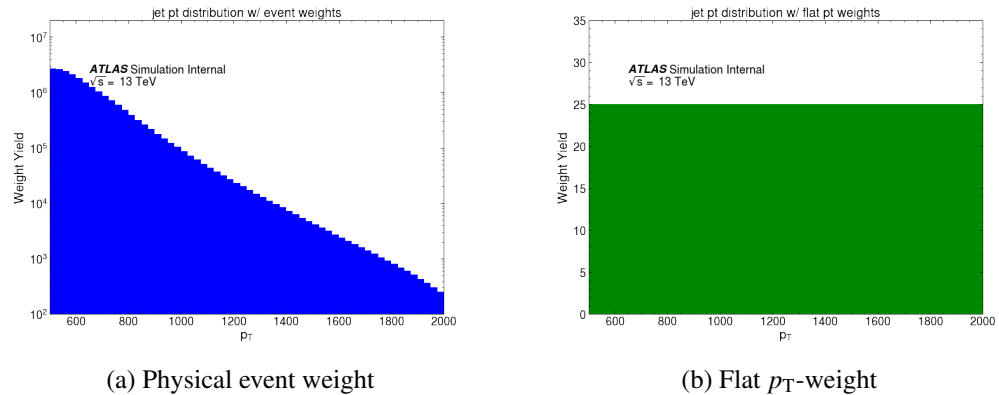


Figure 5.19 The comparison of jet p_T distributions with different weights.

990 5.3.1.3 Training Configuration

991 Approximately 30% of the data from each period of the MC PYTHIA 8 A, D, E is
 992 randomly allocated for the training investigation, constituting an aggregate of roughly 60
 993 million jets. The dataset division for training, validation, and testing is structured in a
 994 ratio of 80% for training, 10% for validation, and 10% for testing.

995 Optuna is employed to conduct a search for optimal hyperparameters. Following the
 996 hyperparameter tuning process, the most optimal model is achieved after 100 iterations
 997 of such procedure. The optimised parameters are listed:

- 998 • bagging_fraction 0.9176347488279626
- 999 • bagging_freq 2
- 1000 • feature_fraction 0.9084973008559477
- 1001 • lambda_11 0.0016400096502256838
- 1002 • lambda_10 0.006327330258011633
- 1003 • min_child_samples 13
- 1004 • num_leaves 224

1005 The performance of a classification model at all classification criteria can be illus-
 1006 trated using a receiver operating characteristic (ROC) curve. The idea is to compare
 1007 the true positive rate (TPR, also known as sensitivity, recall or probability of detection)
 1008 against the false positive rate (FPR, also known as the probability of false alarm) at dif-
 1009 ferent criteria given. Consider a binary classification case, where the outputs are either
 1010 labelled as positive (p) or negative (n), in total there are four possible outputs from a two-
 1011 class prediction problem. A true positive (TP) is given if the output from a prediction is
 1012 p and the actual value is also p, otherwise a false positive (FP) is assigned if the actual
 1013 value is n. Conversely, a true negative (TN) is given if both the prediction outcome and
 1014 the actual value are n, whereas a false negative (FN) is assigned if the actual value is p.
 1015 TPR as a synonym for recall is defined as:

$$TPR = TP / (TP + FN) \quad (5.4)$$

1016 while the FPR is defined as:

$$FPR = FP / (FP + TN) \quad (5.5)$$

1017 In this analysis, the prediction true is defined by higher $|\eta|$ jet and prediction neg-
 1018 ative is defined by lower $|\eta|$ jet. The actual truth value is given by the quark jet from
 1019 the MC truth information, whereas the actual negative value is given by the gluon truth
 1020 information. Thus the quark efficiency is the TPR and the gluon rejection is FPR. An
 1021 Area Under the ROC Curve (AUC) is used to evaluate the performance of a classifier,
 1022 the better performance is indicated by higher AUC values.

1023 Several ROC plots are made to compare different features and the BDT in different
 1024 p_T ranges. To check whether the BDT tagger is overtrained, the shape comparison is
 1025 shown in Figure 5.20, between training dataset and validation dataset. No overtraining
 1026 is observed as the distribution of training dataset is very similar to that of testing dataset.

1027 Figure 5.21 shows the ROC curve for all single jet variables and the BDT-tagger
 1028 in given p_T ranges in forward and central regions. Figure 5.22 shows the AUC of both
 N_{trk} -only tagger and the BDT-tagger as a function of jet p_T .

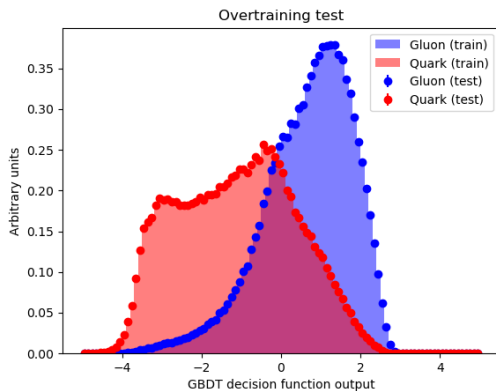
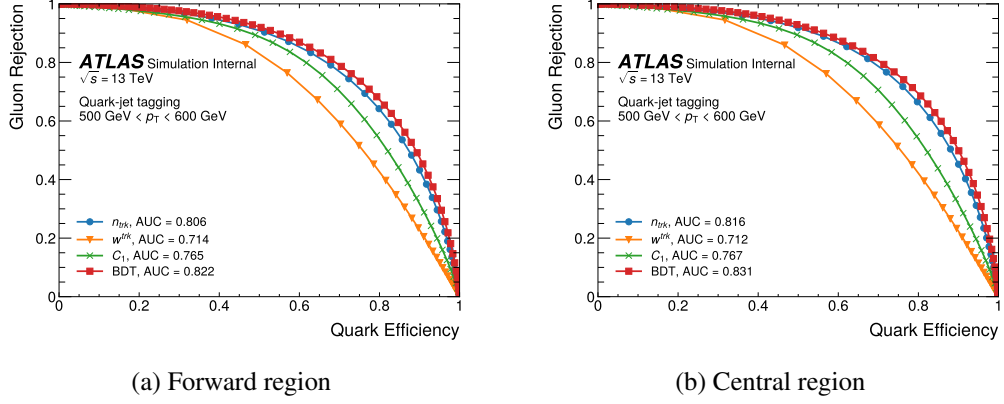
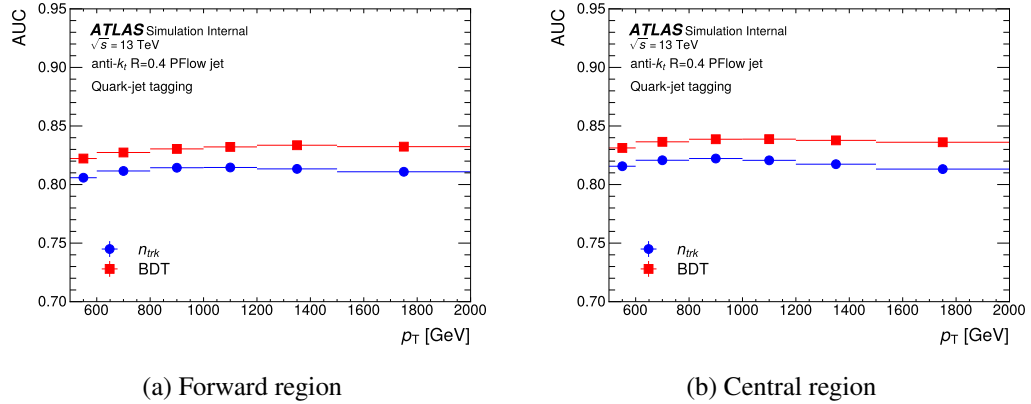


Figure 5.20 Overtraining validation

1029
 1030 The N_{trk} -only tagger is found to be the most sensitive observable than other indi-
 1031 vidual jet substructure variables for q/g tagging, W_{trk} and $C_1^{\beta=0.2}$ are less sensitive to the
 1032 number of tracks inefficiencies because they are defined as ratios, the BDT-tagger which
 1033 include the W_{trk} and $C_1^{\beta=0.2}$ has better AUC than N_{trk} -only tagger across all jet p_T ranges.
 1034 This indicates that the BDT-based tagging mechanism has a heightened capacity to dis-
 1035 criminate against gluon-jets at the same level of efficiency in identifying quark-jets with
 1036 N_{trk} -only tagger . Both taggers are calibrated in this paper, more details are presented in
 1037 the next section.


 Figure 5.21 The ROC Curve for different taggers in the given jet p_T .

 Figure 5.22 The AUC for different taggers across jet p_T .

1038 5.4 Matrix Method

1039 The distribution of q/g tagging variables depend strongly on jet p_T . Thus a matrix
 1040 method [23] approach used to extract the shape of the q/g tagging variables is performed
 1041 on each p_T bin defined in Table 5.3 for quark- and gluon-jets, separately.

1042 To measure the performance of the q/g taggers under study, samples exclusively
 1043 composed of either quark-jets or gluon-jets are needed. In order to deduce the distribu-
 1044 tion shapes of the q/g tagging variables pertaining to quark- and gluon-jets within the
 1045 empirical data, a methodology that capitalizes on samples possessing varying q/g ratios is
 1046 employed. This approach, known as the matrix method [23], facilitates the extraction of
 1047 the distinct distributions of q/g tagging variables for the aforementioned jet categories.

1048 Pure quark- or gluon-jets can be extracted from forward and central jet samples

p_T bin boundary [GeV]					
500-600	600-800	800-1000	1000-1200	1200-1500	1500-2000
Forward & Central $ \eta $ jet samples in multi-jet					

Table 5.3 The p_T range division for the calibration of the q/g tagging variables and samples used in extraction of pure quark and gluon jets.

1049 following the matrix:

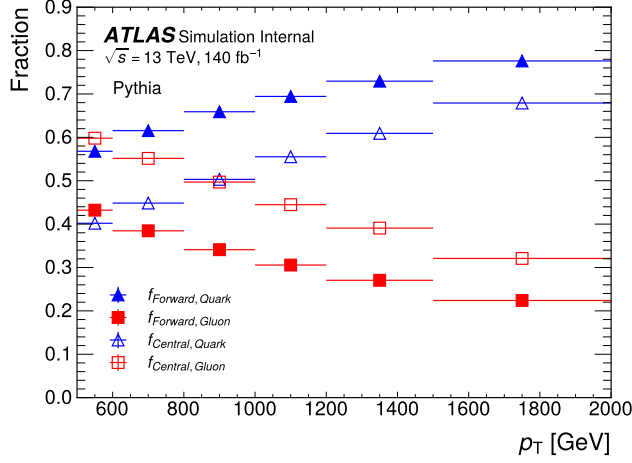
$$\begin{pmatrix} p_F(x) \\ p_C(x) \end{pmatrix} = \underbrace{\begin{pmatrix} f_{F,Q} & f_{F,G} \\ f_{C,Q} & f_{C,G} \end{pmatrix}}_{\equiv F} \begin{pmatrix} p_Q(x) \\ p_G(x) \end{pmatrix} \quad (5.6)$$

$$\begin{pmatrix} p_Q(x) \\ p_G(x) \end{pmatrix} = F^{-1} \begin{pmatrix} p_F(x) \\ p_C(x) \end{pmatrix}. \quad (5.7)$$

1050 where $p_{Q,G}(x)$ represents the distributions of the q/g tagging variable x in pure
 1051 quark- and gluon-enriched jet samples, $p_F(x)$ and $p_C(x)$ show the distributions of jet
 1052 variables in forward and central regions, respectively, $f_{F/C,Q/G}$ are the fractions of quarks
 1053 and gluons in a forward or central region. The inverse matrix of F is thus constructed
 1054 and used to extract pure quark/gluon $p_{Q,G}$. Data is used to obtain the distributions of
 1055 the quark- and gluon-enriched samples, MC is used to calculate the fraction of quarks
 1056 and gluons in them as shown in Figure 5.23, as well as the distributions of q/g tagging
 1057 variables. The matrix is calculated in each x bin and each jet p_T range.

1058 Figure 5.24 illustrates the fraction of light and heavy quark- and gluon-jets in the
 1059 PYTHIA 8 dijet sample. These fractions are depicted in a stacked format, summing up to
 1060 a cumulative value of 1. It should be noted that the involvement of heavy flavour quarks
 1061 constitutes a minor fraction, amounting to a few percent, and is deemed negligible for
 1062 the later study. Previous investigations [ref21] have established that any discrepancies
 1063 among the fractions derived from various MC event generators remain minimal. Fur-
 1064 thermore, the shapes of distributions obtained from the MC simulations generally exhibit
 1065 congruence with those observed within the data. The distributions of N_{trk} and BDT score
 1066 in higher and lower jet regions are shown in Figure 5.25 and Figure 5.26 in jet p_T range
 1067 500 GeV - 600 GeV. The shapes of distributions obtained from the MC simulations is
 1068 generally consistent with that from data.

The calibration of quark/gluon jets taggers



(a)

Figure 5.23 Fractions of quark-jets and gluon-jets in forward jet and central jet regions from PYTHIA dijet process. These values are used as elements in F matrix in Equation 5.6.

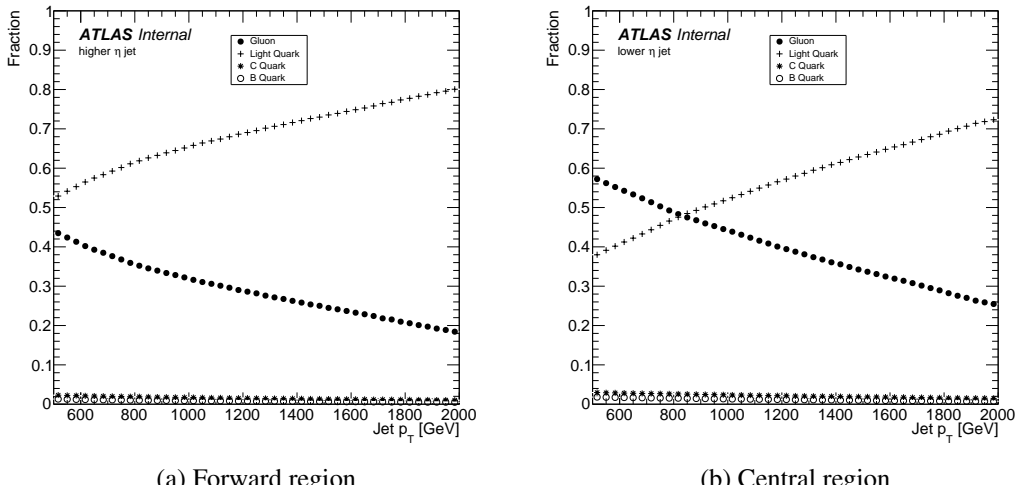


Figure 5.24 Flavor composition of forward (a) or central (b) multi-jet events.

The calibration of quark/gluon jets taggers

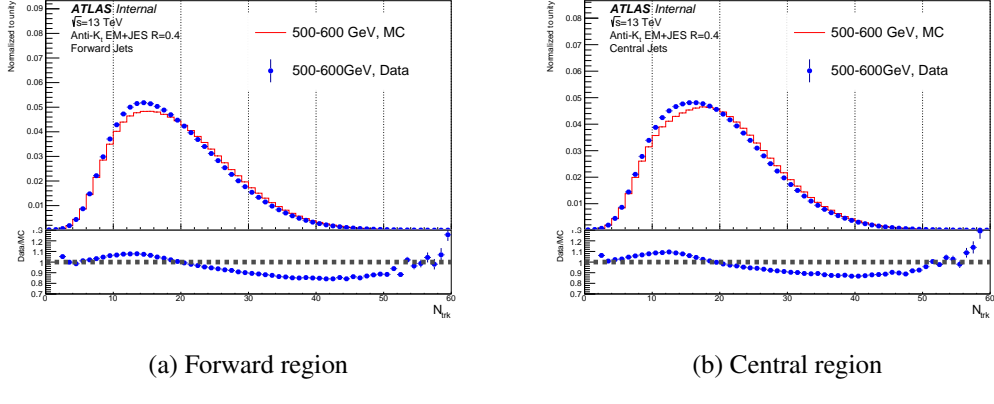


Figure 5.25 The N_{trk} distribution of the leading two jets with PYTHIA 8 in the MC and data.

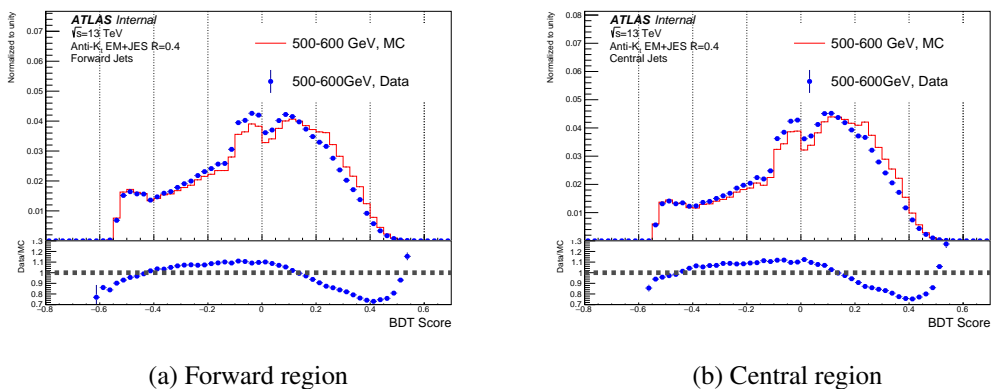


Figure 5.26 The BDT score distribution of the leading two jets with PYTHIA 8 in the MC and data.

1069 5.5 MC non-closure

1070 The matrix method is valid under the assumption that the shapes of $p_Q(x)$ and $p_G(x)$
 1071 remain consistent, regardless of whether the jets are situated in the central or forward
 1072 regions. Jet fragmentation at a pp collider is expected to be predominantly influenced
 1073 by the jet p_T and is generally considered independent of η , considering the underlying
 1074 parton type. Consequently, an approach aimed at extracting distributions associated with
 1075 the radiation patterns of quark-jets and gluon-jets should be valid at the particle level. At
 1076 the detector level, however, the measured radiation pattern within jets no longer retains its
 1077 η -independence. This is due to variations arising from differences in detector materials
 1078 and technologies, leading to distinctions between the central and forward regions in terms
 1079 of response. As a consequence of these effects, the matrix method experiences deviations
 1080 from closure, indicating a disparity between the expected and actual outcomes.

1081 The distributions of N_{trk} have been seen to have systematic difference for the truth-
 1082 labelled quark/gluon jets in the quark-enriched and gluon-enriched regions in each p_T bin.
 1083 To rectify this discrepancy and ensure alignment in the distribution of jet tagging vari-
 1084 ables between the central and forward regions, a re-weighting procedure is implemented.
 1085 This procedure involves applying adjustments to account for the observed differences.
 1086 For each event, the central jet is weighted by a re-weighting factor :

$$w_{Q/G}(x; p_{T,j}) = \frac{p_{Q/G, \text{forward}}(x; p_{T,j})}{p_{Q/G, \text{central}}(x; p_{T,j})} \quad (5.8)$$

1087 where q/g tagging variable x is calculated in each jet p_T bin for quark and gluon jets,
 1088 respectively. By default the re-weighting factor derived from truth-labelled quark-jets is
 1089 implemented for both types of jets, whereas the re-weighting factor derived from truth-
 1090 labelled gluon-jets is used as an alternative to evaluate the systematic uncertainty from
 1091 the re-weighting procedure, known as MC non-closure systematic uncertainty for the
 1092 calibration.

1093 The distributions of N_{trk} in extracted pure quark- and gluon-jets and truth-labelled
 1094 MC before re-weighting as shown in Figure 5.27. After the re-weighting the distributions
 1095 of N_{trk} are shown in Figure 5.28. The non-closure is at few percent level and is taken
 1096 as MC non-closure systematic uncertainty.

The calibration of quark/gluon jets taggers

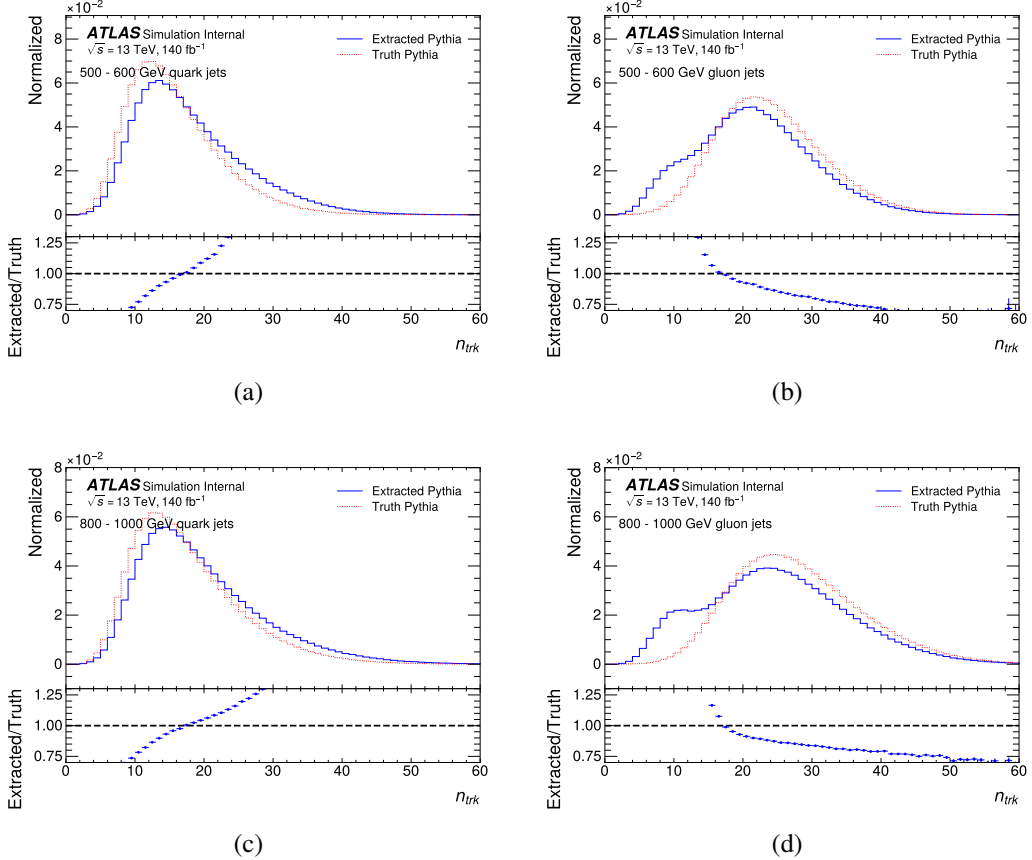


Figure 5.27 Before re-weighting: the N_{trk} distributions of quark-jet (a) (c) and gluon-jet in (b) (d) from PYTHIA 8 sample. Dashed and solid-line show the N_{trk} distributions in the truth MC and extracted MC, respectively. Bottom panels show the ratio of the extracted MC to the truth MC.

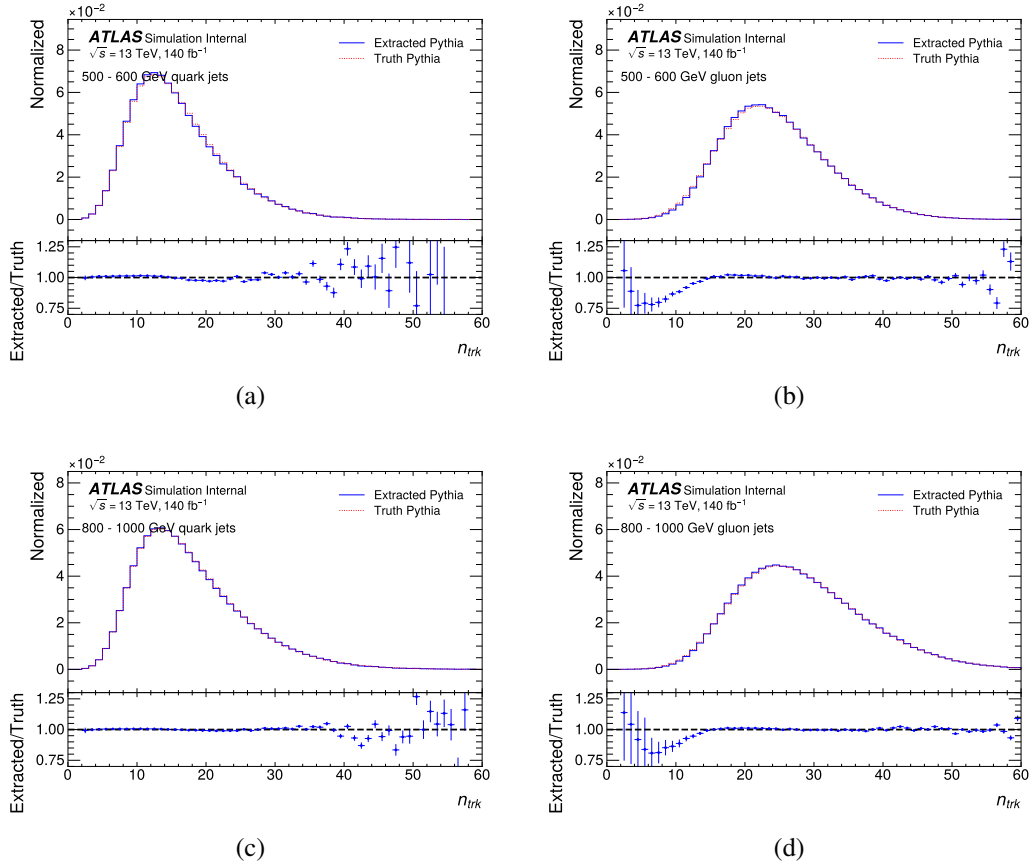


Figure 5.28 After re-weighting with quark factor: the N_{trk} distributions of quark-jet (a) (c) and gluon-jet in (b) (d) from PYTHIA 8 sample. Dashed and solid-line show the N_{trk} distributions in the truth MC and extracted MC, respectively. Bottom panels show the ratio of the extracted MC to the truth MC.

1097 **5.5.1 Closure test for BDT tagger**

1098 Similar to the distribution of N_{trk} , the distributions of BDT score for truth labelled-
 1099 jets exhibit systematic disparities in forward and central regions. Therefore, the same
 1100 re-weighting procedure as described is performed for BDT tagger as well. The MC non-
 1101 closure test is thus conducted by comparing the distributions of BDT score for extracted
 1102 and truth quark- and gluon-jets, separately, as shown in Figure 5.29. The distributions
 1103 of BDT before and after re-weighting are shown in Figure 5.30 and Figure 5.31. The
 1104 non-closure is about few percent level and taken as one systematic uncertainty.

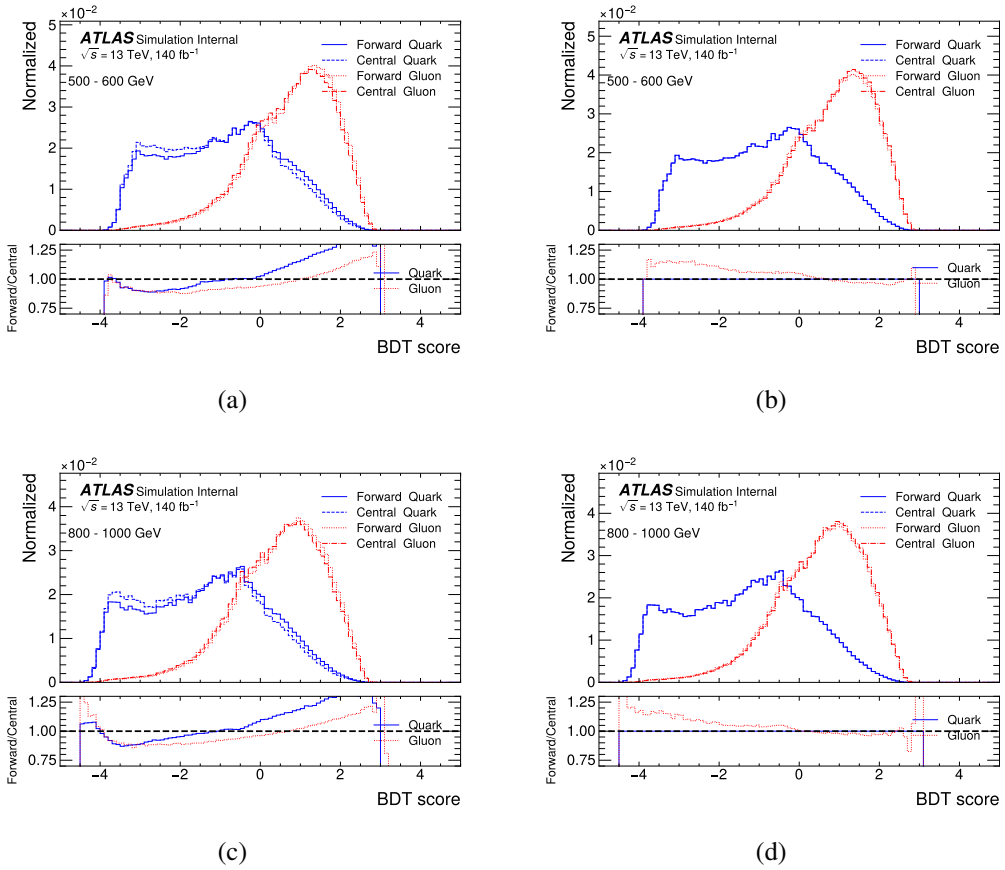


Figure 5.29 The distribution of BDT score for jets before (a) (c) and after (b) (d) re-weighting.

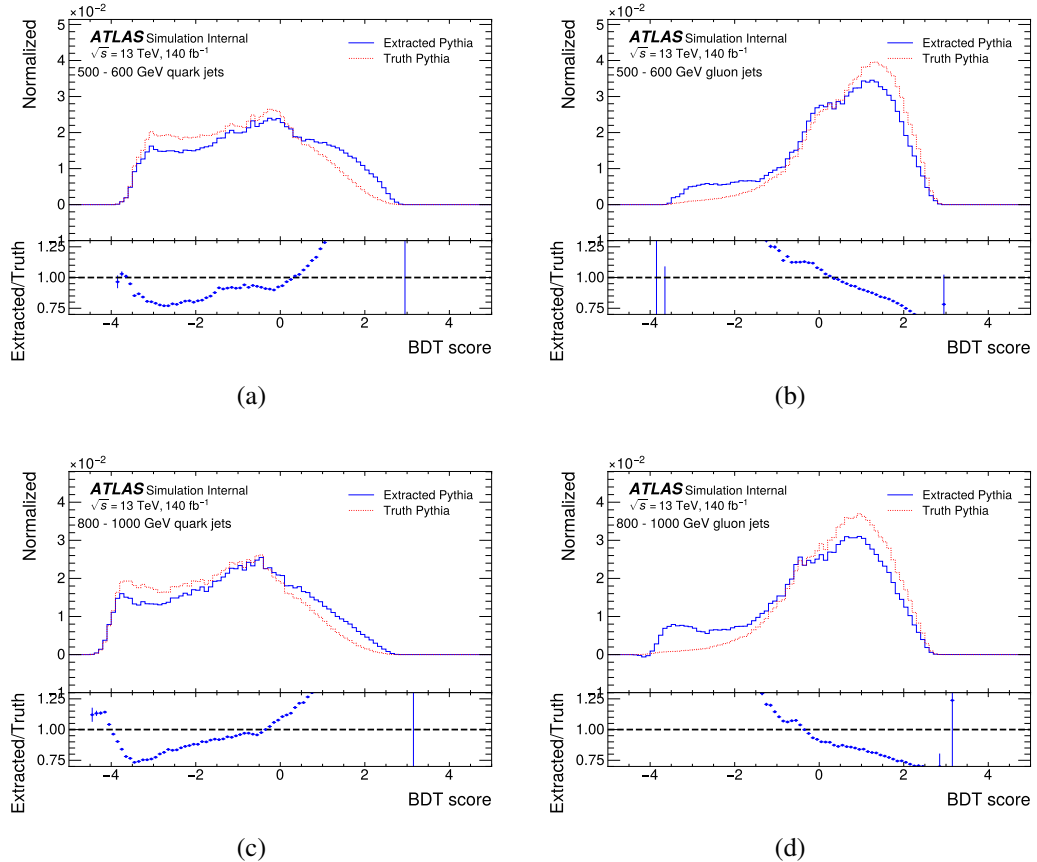


Figure 5.30 Before re-weighting: the MC-closure for quark-jet in (a) (c) and for gluon-jet in (b) (d) in BDT distributions from PYTHIA 8 sample. Dashed and solid-line histograms show the BDT distributions in the truth MC and extracted MC, respectively. Bottom panels show the ratio of the extracted MC to the truth MC.

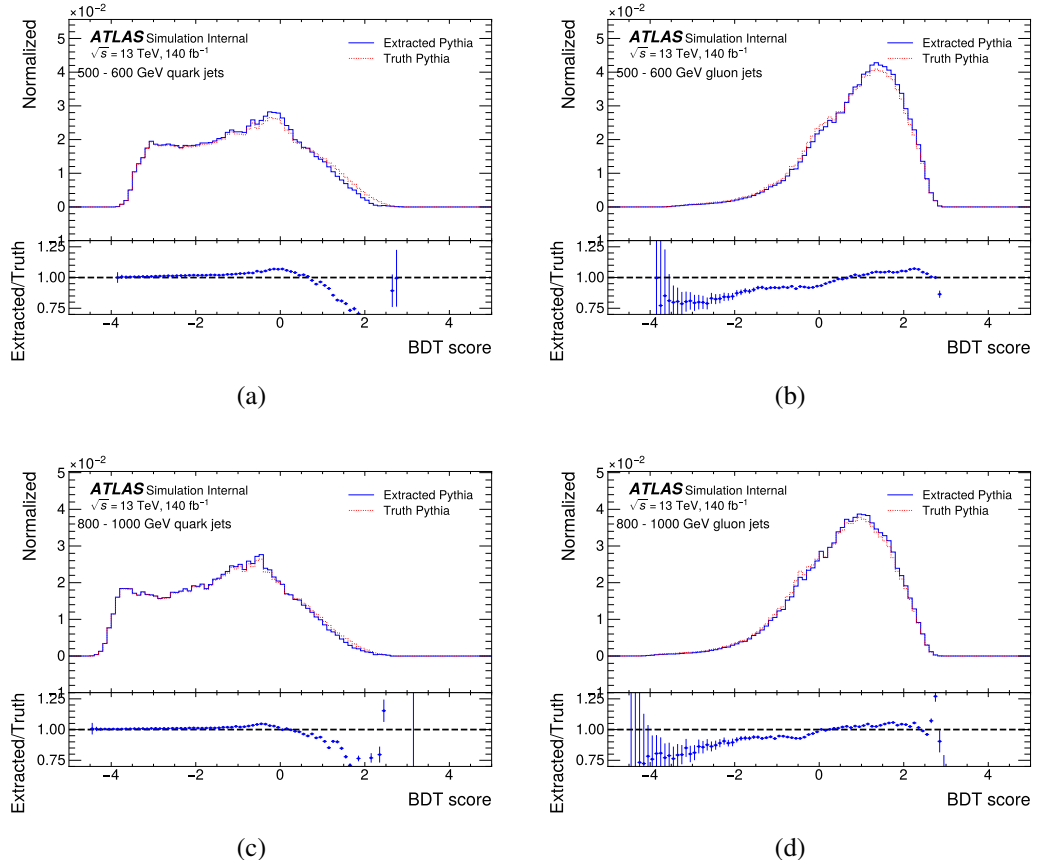


Figure 5.31 After re-weighting: the MC-closure for quark-jet in (a) (c) and for gluon-jet in (b) (d) in BDT distributions from PYTHIA 8 sample. Dashed and solid-line histograms show the BDT distributions in the truth MC and extracted MC, respectively. Bottom panels show the ratio of the extracted MC to the truth MC.

1105 **5.5.2 Summary for the MC Closure test**

1106 After applied the re-weighting factor to the jet tagging variables N_{trk} and BDT, the
 1107 distributions of extracted quark-and gluon-jets converge with those of truth jets. The
 1108 residual discrepancy, which has only few percent level to the total events is taken into
 1109 account as MC non-closure systematic uncertainty. No obvious dependency on jet η is
 1110 observed from the distributions of jet tagging variables.

1111 **5.6 Scale factor**

1112 The calibration of the q/g tagging variables is performed by applying binned scale
 1113 factor (SF) in the simulation for each quark- and gluon-jet, respectively. The scale factor
 1114 is obtained from distributions of the variables in quark- and gluon-jets from MC in order
 1115 to match the shape of the simulation to that of the data.

1116 The tagger working points (WP) are established for fixed quark-jets efficiency in
 1117 the nominal MC sample, for both taggers. At a given working point, the efficiencies for
 1118 quark- and gluon-jets are defined as follows:

$$\epsilon_{Q/G}(x^{WP}) = \int_{x < x^{WP}} p_{Q/G}(x) dx. \quad (5.9)$$

1119 Rejection factors corresponding to quark- and gluon-jets can also be given as:

$$\xi_{Q/G}(x^{WP}) = 1 / \int_{x > x^{WP}} p_{Q/G}(x) dx = 1 / (1 - \epsilon_{Q/G}(x^{WP})). \quad (5.10)$$

1120 Discrepancies observed between the quark-jet tagging efficiencies and gluon-jet re-
 1121 jections obtained from data and the corresponding values anticipated from the MC sim-
 1122 ulations are quantified using data-to-MC scale factors (SF). These factors are computed
 1123 separately for each q/g tagger in various p_T bins, at a fixed WP. The SF is defined using
 1124 Equation 5.9 and 5.10 for quark- and gluon-jets, respectively :

$$\text{SF}_Q(x^{WP}) = \frac{\epsilon_Q^{\text{Data}}(x^{WP})}{\epsilon_Q^{\text{MC}}(x^{WP})}. \quad (5.11)$$

$$\text{SF}_G(x^{WP}) = \frac{\xi_G^{\text{Data}}(x^{WP})}{\xi_G^{\text{MC}}(x^{WP})}. \quad (5.12)$$

1125 where $\varepsilon_{Q/G}^{\text{Data}}(x^{WP})$ and $\varepsilon_{Q/G}^{\text{MC}}(x^{WP})$ are $\varepsilon_{Q/G}(x^{WP})$ in data and MC, respectively. Same defi-
1126 nitions apply to $\xi_{Q/G}(x^{WP})$. The WPs corresponding to fixed quark-jets tagging efficien-
1127 cies of 50%, 60%, 70%, and 80% have been examined, revealing analogous trends in the
1128 characteristics of SFs.

1129 Figure 5.32 to 5.35 show the distribution of all jet tagging variables in quark- and
1130 gluon-jets after matrix method extraction in all different MC samples and data in given
1131 p_T range.

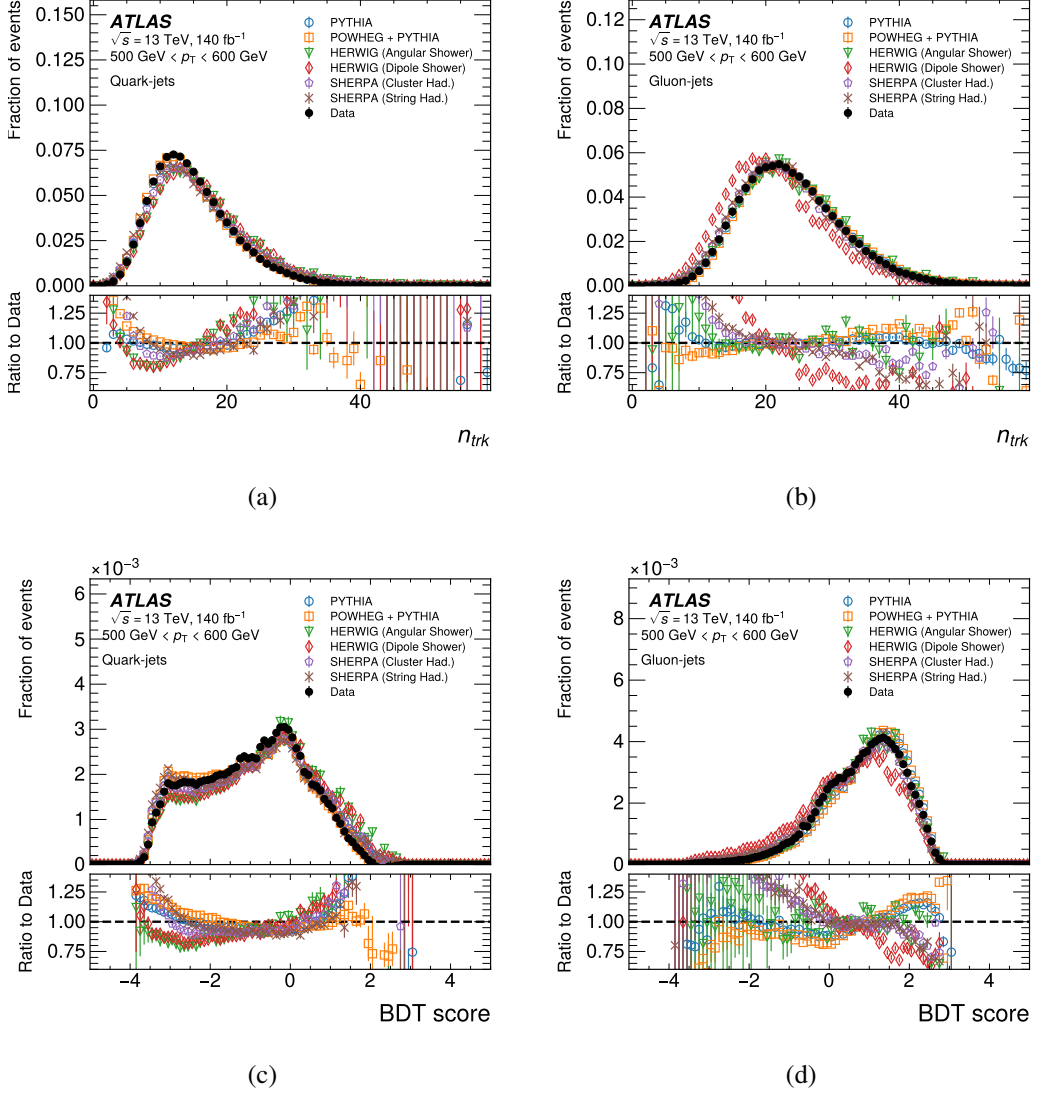


Figure 5.32 The distributions of N_{trk} (a,b) and BDT score (c,d) for quark-jets (left) and gluon-jets (right) using different generators (open symbols) and data (closed symbol) are shown in the upper panels. The lower panels show the ratio of each MC distribution and the data. The vertical error bars show the statistical uncertainty.

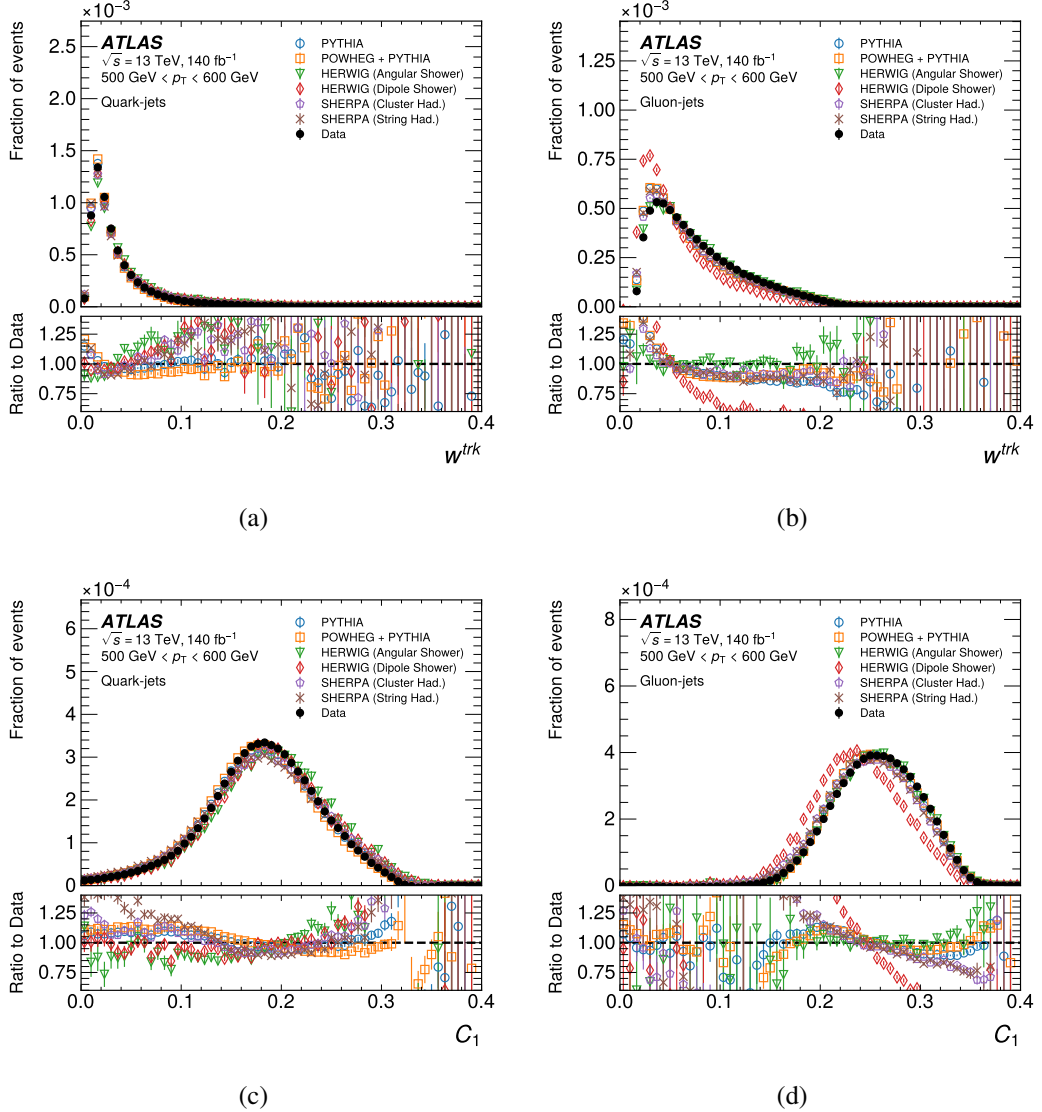


Figure 5.33 The distributions of W_{trk} (a,b) and C_1 (c,d) for quark-jets (left) and gluon-jets (right) using different generators (open symbols) and data (closed symbol) are shown in the upper panels. The lower panels show the ratio of each MC distribution and the data. The vertical error bars show the statistical uncertainty.

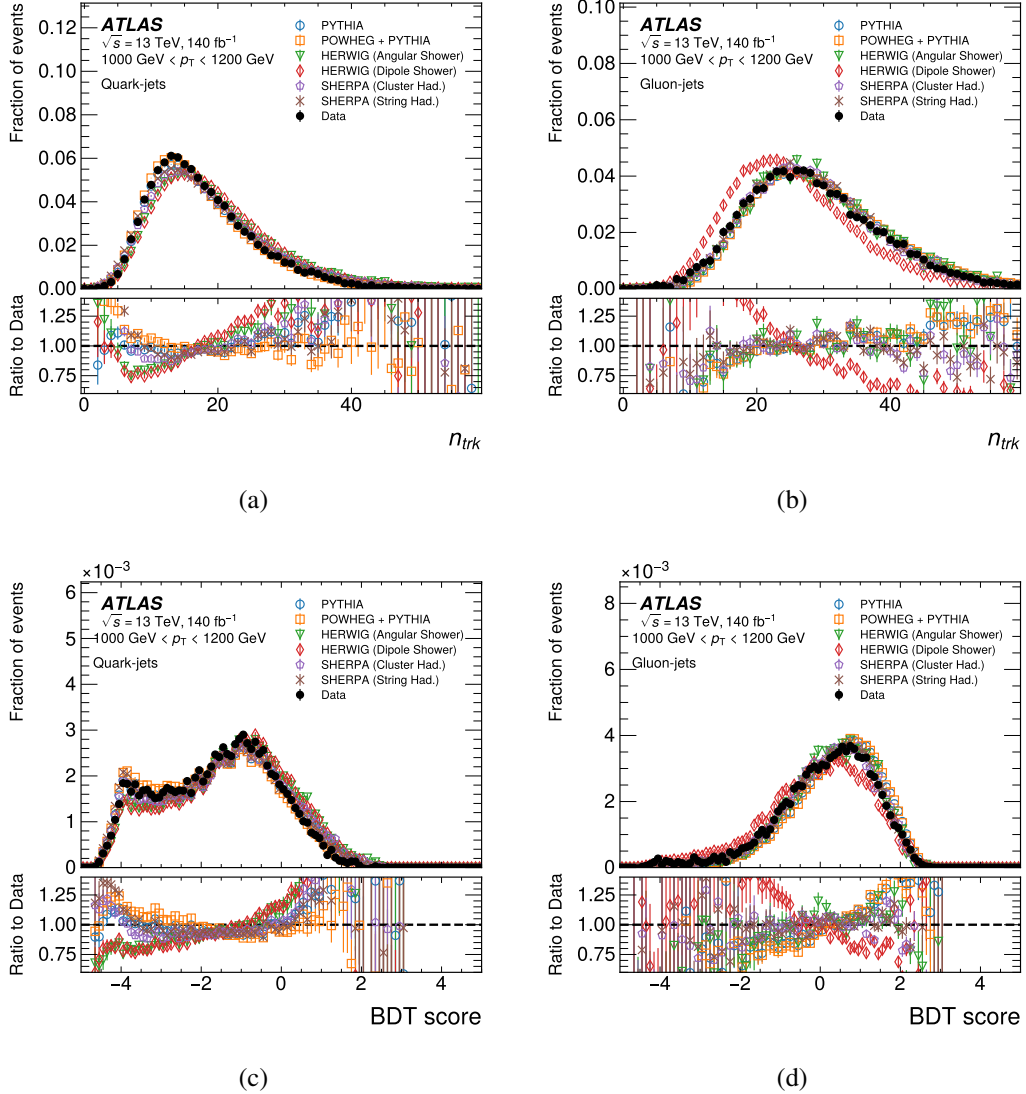


Figure 5.34 The distributions of N_{trk} (a,b) and BDT score (c,d) for quark-jets (left) and gluon-jets (right) using different generators (open symbols) and data (closed symbol) are shown in the upper panels. The lower panels show the ratio of each MC distribution and the data. The vertical error bars show the statistical uncertainty.

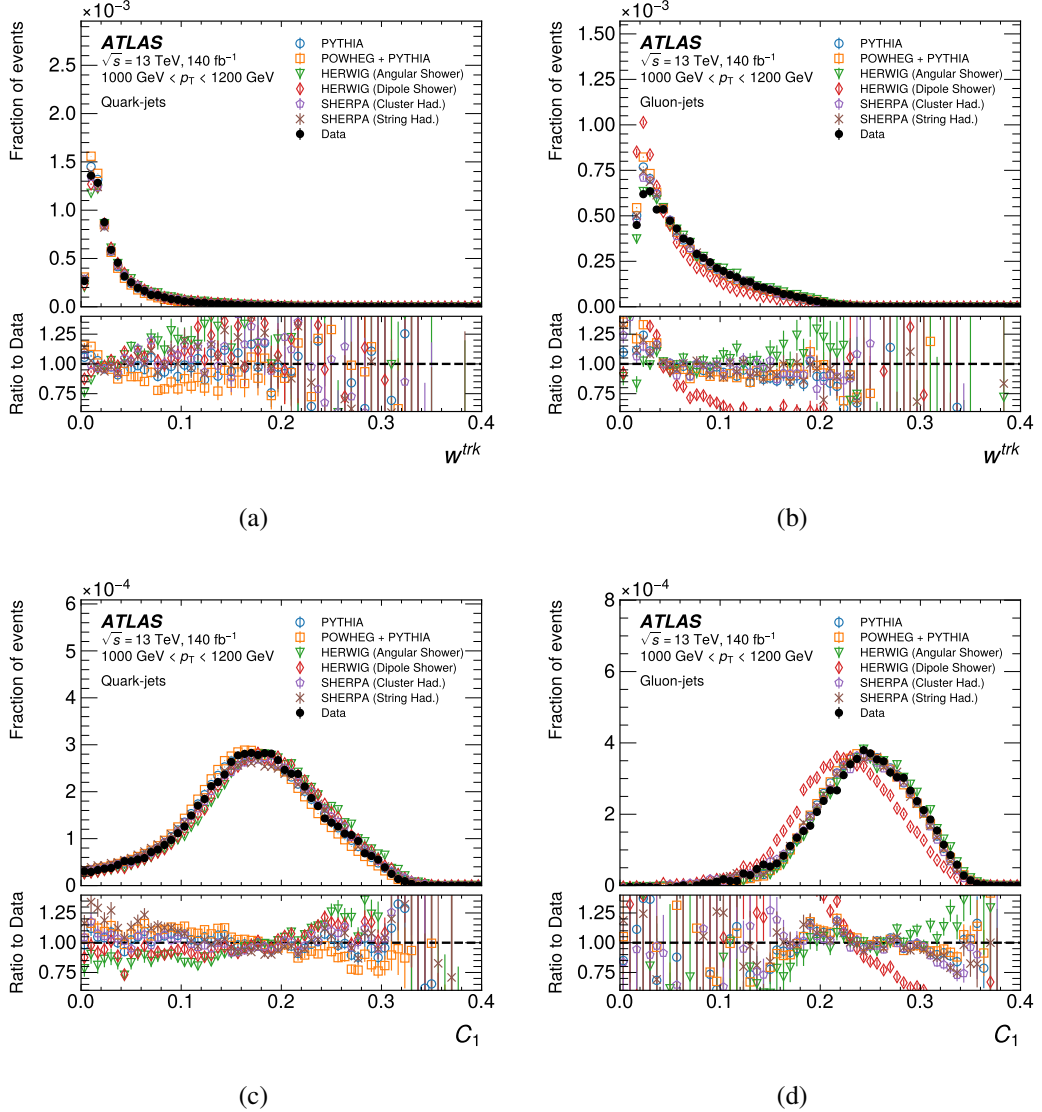


Figure 5.35 The distributions of W_{trk} (a,b) and C_1 (c,d) for quark-jets (left) and gluon-jets (right) using different generators (open symbols) and data (closed symbol) are shown in the upper panels. The lower panels show the ratio of each MC distribution and the data. The vertical error bars show the statistical uncertainty.

1132 Cut values corresponding to the 50% WP are summarised in Table 5.4 for the N_{trk} -
 1133 only tagger and Table 5.5 for the BDT-tagger. Figure 5.36 shows the gluon-jets efficiency
 1134 of both N_{trk} -only tagger and the BDT-tagger as a function of jet p_{T} , for the MC and data,
 1135 at four WPs.

1136 Both the N_{trk} -only and BDT-taggers demonstrate commendable performance on
 1137 data, with high quark signal efficiency across all p_{T} range. Notably, at the 50% work-
 1138 ing point, the N_{trk} -only tagger achieves approximately 90% rejection of gluon-jets, while
 1139 the BDT tagger surpasses this performance by rejecting around 93% of gluon-jets. The
 1140 BDT-tagger outperforms the N_{trk} -only tagger by exhibiting superior gluon-jets rejection
 1141 rates at the identical WP. This disparity in performance arises from the inclusion of a
 1142 more comprehensive set of jet substructure variables in the BDT approach. The discrep-
 1143 arity between the level of gluon-jet rejection observed in data and that predicted by the
 1144 MC samples increases as the jet p_{T} increases. This phenomenon is closely tied to the
 1145 dissimilarity between the modelling of gluons and their actual behaviour in data.

p_{T} [GeV]	500 - 600	600 - 800	800 - 1000	1000 - 1200	1200 - 1500	1500 - 2000
WP						
0.5	15.0	16.0	17.0	18.0	18.0	19.0
0.6	17.0	18.0	19.0	20.0	20.0	21.0
0.7	19.0	20.0	21.0	22.0	23.0	24.0
0.8	22.0	23.0	24.0	26.0	27.0	28.0

Table 5.4 Cut values of N_{trk} at different working point in each of jet p_{T} range

p_{T} [GeV]	500 - 600	600 - 800	800 - 1000	1000 - 1200	1200 - 1500	1500 - 2000
WP						
0.5	-0.8	-1.0	-1.2	-1.4	-1.6	-1.8
0.6	-0.4	-0.6	-0.8	-1.0	-1.2	-1.4
0.7	0.0	-0.2	-0.4	-0.6	-0.8	-1.0
0.8	0.4	0.2	0.0	-0.2	-0.3	-0.6

Table 5.5 Cut values of BDT at different working point in each of jet p_{T} range

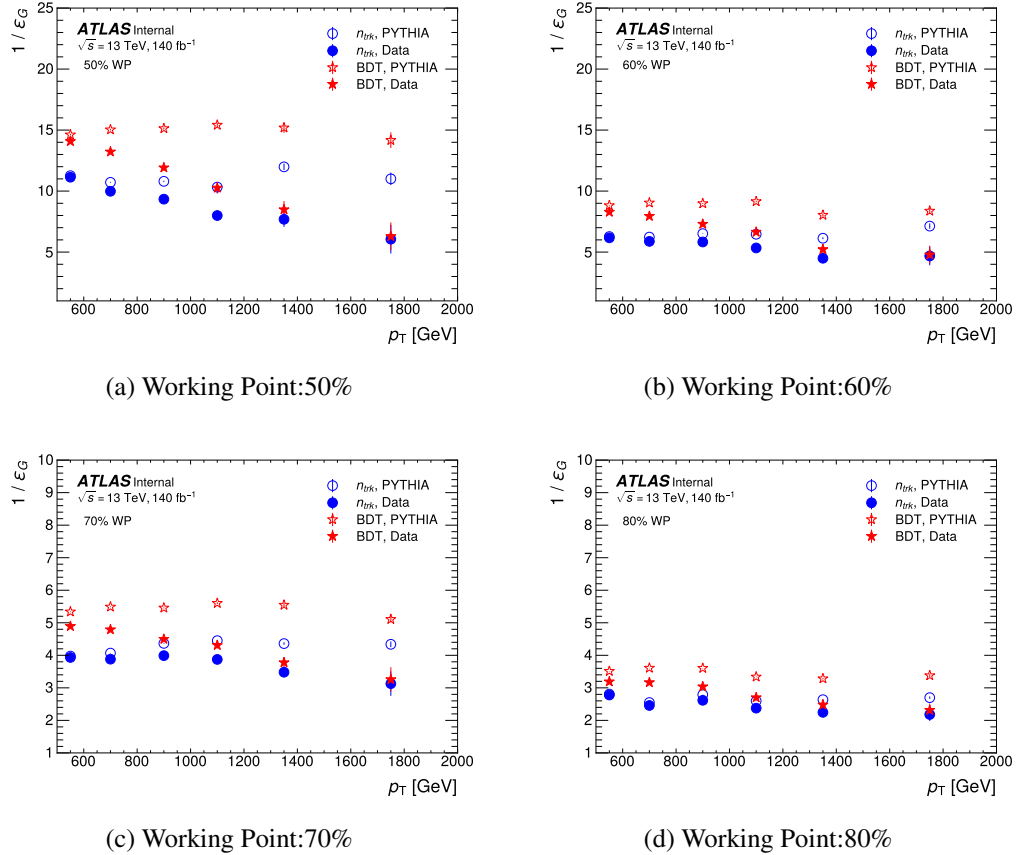


Figure 5.36 Inverse of the gluon-jet efficiency of N_{trk} (circles) and BDT (stars) as a function of jet p_T at the each WP in data (closed symbols) and the PYTHIA (open symbols) MC. The vertical error bars show the statistical uncertainty.

1146 **5.7 Systematic uncertainties**

1147 In this study, different types of systematic uncertainty are taken into account. The
1148 distribution of N_{trk} and BDT for truth-labelled quark-/gluon-jets are given by the MC
1149 simulation samples, therefore, theoretical uncertainties originate from aspects encom-
1150 passing the modelling of the MC simulation, such as choices involving parton showering,
1151 hadronisation, matrix element, PDFs, scale variations, and Splitting-Kernel effects. Fur-
1152 thermore, experimental uncertainties such as JES and JER, tracking reconstruction effi-
1153 ciencies are meticulously incorporated. The potential impact of methodological choices,
1154 including N_{trk} or BDT re-weighting, as well as the non-closure behaviour of MC simula-
1155 tions, is propagated to the resultant SFs.

1156 The nominal result in this analysis is provided using PYTHIA 8 MC samples, all
1157 other MC samples are considered as alternative samples to study corresponding system-
1158 atic uncertainty.

1159 **5.7.1 Parton shower modelling uncertainty**

1160 The different chose of algorithmic or parametric in the modelling of the parton
1161 shower could result in different SF result. This systematic uncertainty is estimated by
1162 comparing the SFs extracted from two MC samples with the same ME and hadronisation
1163 but different types of showers: HERWIG Angular-ordered and HERWIG Dipole samples.
1164 The corresponding fractions of quarks and gluons present in these two MC samples, are
1165 presented in Figure 5.37. The difference of extracted SFs between these two samples is
1166 less than 10% for quark signal efficiency and around 20% for gluon rejection efficiency.
1167 While the influence on quark scale factors is negligible, it takes on a dominant role in the
1168 context of gluon scale factors.

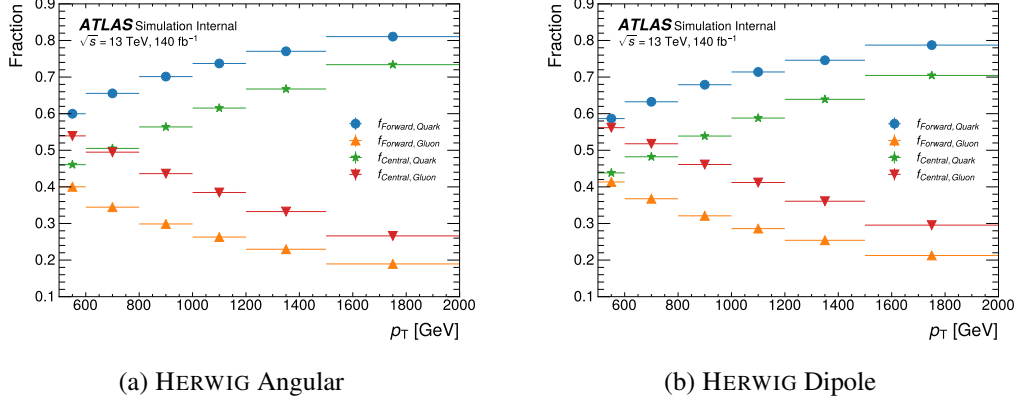


Figure 5.37 Fractions of quark- gluon-jets of HERWIG angular (a) and HERWIG dipole (b) samples.

1169 5.7.2 Hadronisation modelling uncertainty

1170 The uncertainty from hadronisation modelling is given by the difference between
 1171 the extracted SFs from the SHERPA MC samples with cluster-based hadronisation mod-
 1172 elling and string-based hadronisation modelling, separately. The corresponding fractions
 1173 of quarks and gluons present in these two MC samples are presented in Figure 5.38. The
 1174 uncertainty on the SFs range from 1% to 8% for both jet types.

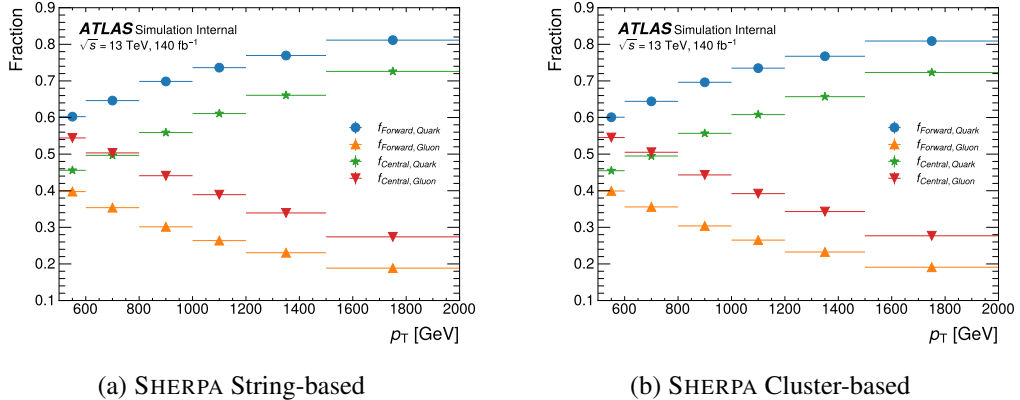


Figure 5.38 Fractions of quark- and gluon-jets in each SHERPA sample.

1175 5.7.3 Matrix element uncertainty

1176 The uncertainty introduced by different types of ME in the MC samples is taken
 1177 from the differences in the extracted SFs in two MC samples with different ME : POWHEG and
 1178 PYTHIA . The corresponding fractions of quarks and gluons present in the POWHEG sam-
 1179 ples are presented in Figure 5.39.

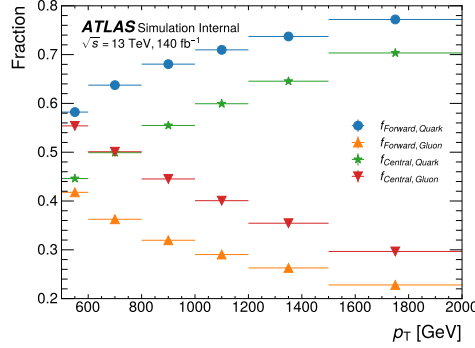


Figure 5.39 Fractions of quark jets and gluon jets in POWHEG samples.

1180 5.7.4 PDF uncertainty

1181 The uncertainty from the PDF set is evaluated using LHAPDF [1] package which
 1182 provides the PDF internal variations for each PDF set, a NNPDF2.3 set is chosen
 1183 to evaluate the various weights which depend on the momentum fraction. The PDF
 1184 uncertainty is given by changing the nominal PDF weight to the systematic variation,
 1185 then compare the SFs extracted from each of variations. The PDF uncertainty is around
 1186 5% - 7% level and almost negligible compared to others.

1187 5.7.5 Scale variation uncertainty

1188 The variation of the renormalisation (μ_R) and factorisation (μ_F) scales in QCD is
 1189 used to evaluate the uncertainty caused by missing higher order corrections. The nominal
 1190 PYTHIA sample is used for such estimation. In total there are 7 scale variations (μ_R, μ_F)
 1191 in (2,2), (2,1), (1,1), (1,2), (1,0.5), (0.5,1), (0.5,0.5) studied in this analysis. The scale
 1192 uncertainty is given by taking the maximum shift of the envelope with respect to the
 1193 nominal one at each working points. The total scale uncertainty is around 4% - 7%.

1194 **5.8 Splitting-Kernel variation uncertainty**

1195 All formulations of shower processes are constructed on the fundamental founda-
1196 tion of the universal behaviour exhibited by singular infrared (soft and/or collinear) lim-
1197 its within QCD. Nonetheless, when one ventures beyond these limits into the physical
1198 phase space where these kernels are employed as approximations, there are in principle
1199 infinitely many different radiation functions to choose from, sharing the same singular
1200 terms but having different non-singular ones. The Splitting-Kernel variations [71] are
1201 variations of the non singular part of the splitting functions, for initial-state radiation and
1202 final-state radiation. Such uncertainty is less than 1%.

1203 **5.9 Tracking uncertainty**

1204 he number of associated tracks is the most important input for both taggers, with
1205 tracking-related systematics exerting an impact on the measurement of SFs. he uncer-
1206 tainty associated with reconstructed tracks is partitioned into two components: the un-
1207 certainty pertaining to track reconstruction efficiency and the MC fake rate [21]. Both
1208 sources of uncertainty are factored in to recalibrate the count of tracks associated with
1209 jets.

1210 The track reconstruction efficiency uncertainty originates from material-related un-
1211 certainties, which constitutes the prevailing source, as well as from considerations related
1212 to the physics model. These uncertainties are estimated through a comparison of track
1213 efficiency across samples that encompass diverse detector modelling configurations. On
1214 the other hand, the MC fake rate is determined by contrasting the trends in a specific
1215 aspect of track multiplicity as a function of the average number of interactions per bunch
1216 crossing between empirical data and the MC simulation. The disparity in final SFs be-
1217 tween the nominal value and the outcome of the systematic variation contributes to the
1218 tracking systematic uncertainty. This uncertainty spans a range of approximately 1% to
1219 8%.

1220 **5.10 JES /JER uncertainty**

1221 The uncertainties associated with JES stem from the process of calibrating the trans-
1222 verse momentum balance between jets located in the central and forward regions, while
1223 also accommodating uncertainties linked to single-particle and test beam measurements.

1224 The JER uncertainties encompass the disparities between data and the MC. For each
 1225 JES/JER variation, a corresponding SF is derived, and the difference between the nom-
 1226 inal value and the variation is computed to determine the systematic uncertainty. The
 1227 cumulative JES/JER uncertainty amounts to approximately 0.2%.

1228 **5.10.1 N_{trk} / BDT re-weighting**

1229 The quark-enriched and gluon-enriched regions are defined by comparing the η of
 1230 leading and subleading jets, introduces to an η dependency from track reconstruction
 1231 process. A re-weighting factor defined by Equation 5.8 is applied on N_{trk} and BDT
 1232 taggers for each event to reduce the impact from different track multiplicity in different
 1233 η range. The re-weighting factors acquired from truth-labelled gluon jets are regarded
 1234 as an alternative source of contribution to the systematic uncertainty. It's worth noting
 1235 that the differences arising from the re-weighting procedure remain comparatively minor
 1236 (about 0.1% - 0.5%) in comparison to other sources of uncertainty.

1237 The distributions of N_{trk} and BDT for extracted quark and gluon-jets after re-weighting
 1238 with quark factor have been shown in the previous chapter. The truth distribution of
 1239 quark/gluon in forward/central jets using gluon factors are shown in Figure 5.40 for
 1240 N_{trk} and Figure 5.41 for BDT, respectively. Figure 5.42, Figure 5.43 shows the distribu-
 1241 tions of extracted quark and gluon-jets after reweighting with gluon factor.

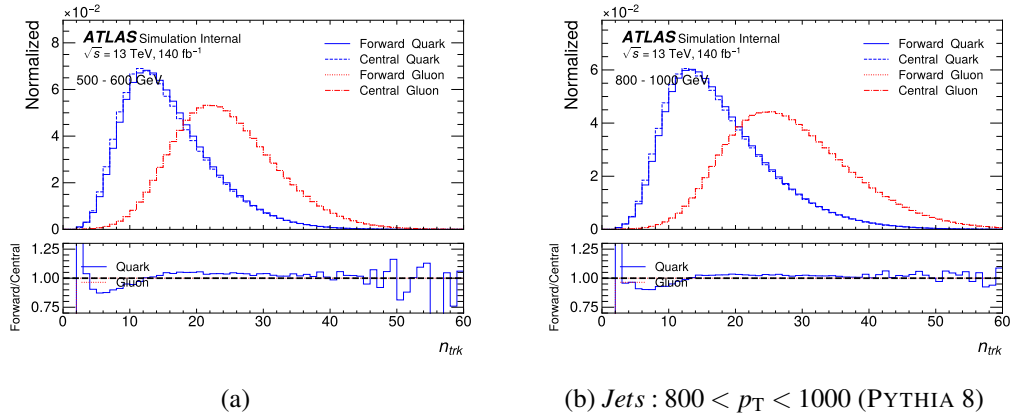


Figure 5.40 The distribution of N_{trk} for jets between 500-600 GeV (a) and 800-1000 GeV (b) after N_{trk} re-weighting using gluon factor.

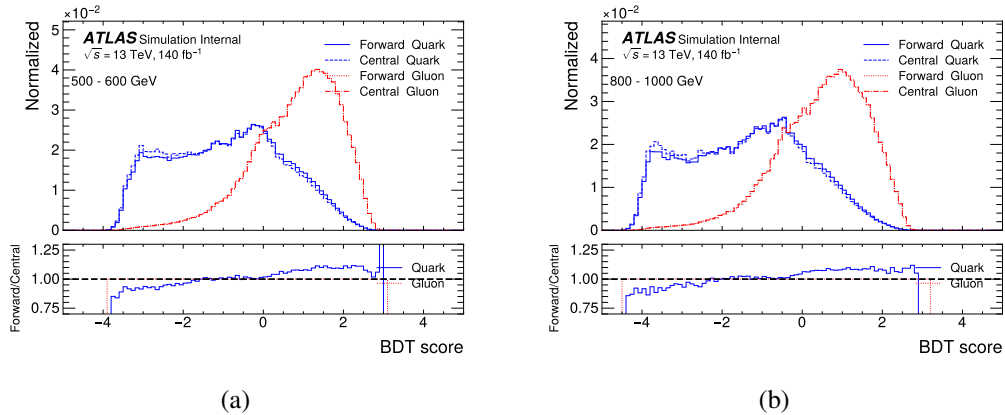


Figure 5.41 The distribution of BDT for jets between 500-600 GeV (a) and 800-1000 GeV (b) after re-weighting using gluon factor.

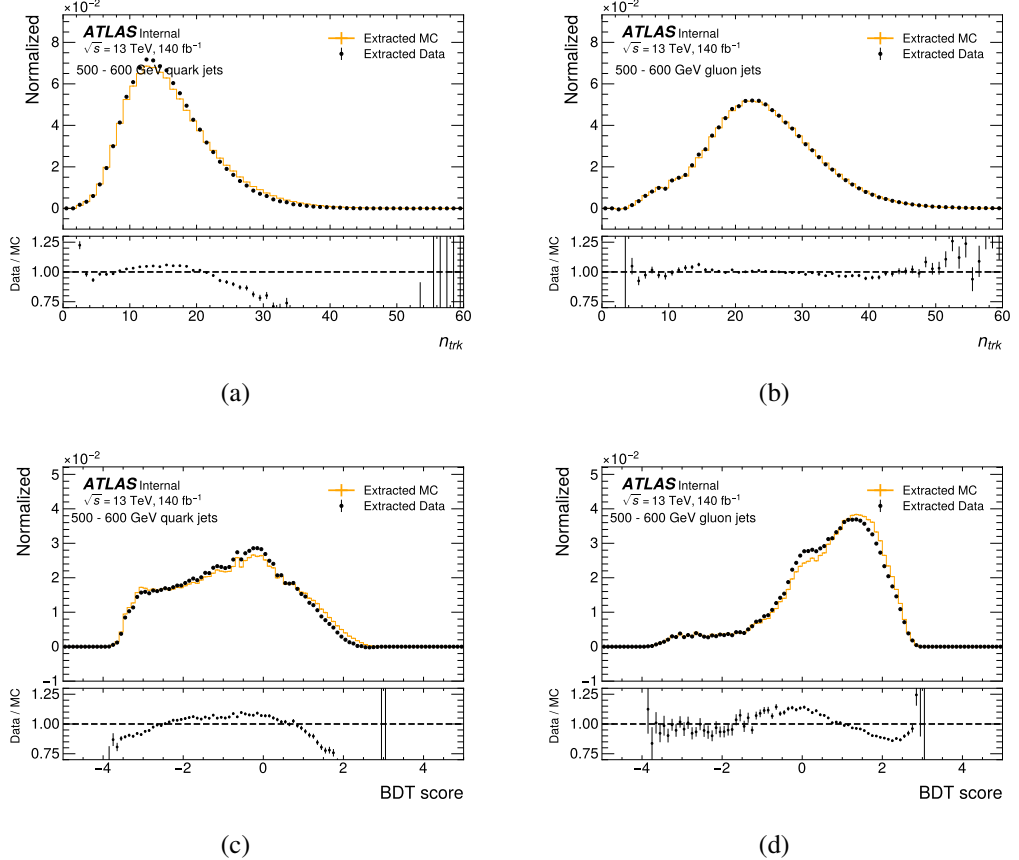


Figure 5.42 The N_{trk} (top) and BDT (bottom) distributions extracted by the matrix method from the data and MC of pure quark-jets (a) (c) and gluon-jets ?? (d) by PYTHIA 8. extracted by the matrix method from the data and MC. The gluon factor is applied. Solid-line histograms show the distributions of quark or gluon-jets defined by the jet parton flavour label in the MC. A bottom panel in each figure shows the ratio of the extracted data to the extracted MC by the matrix method.

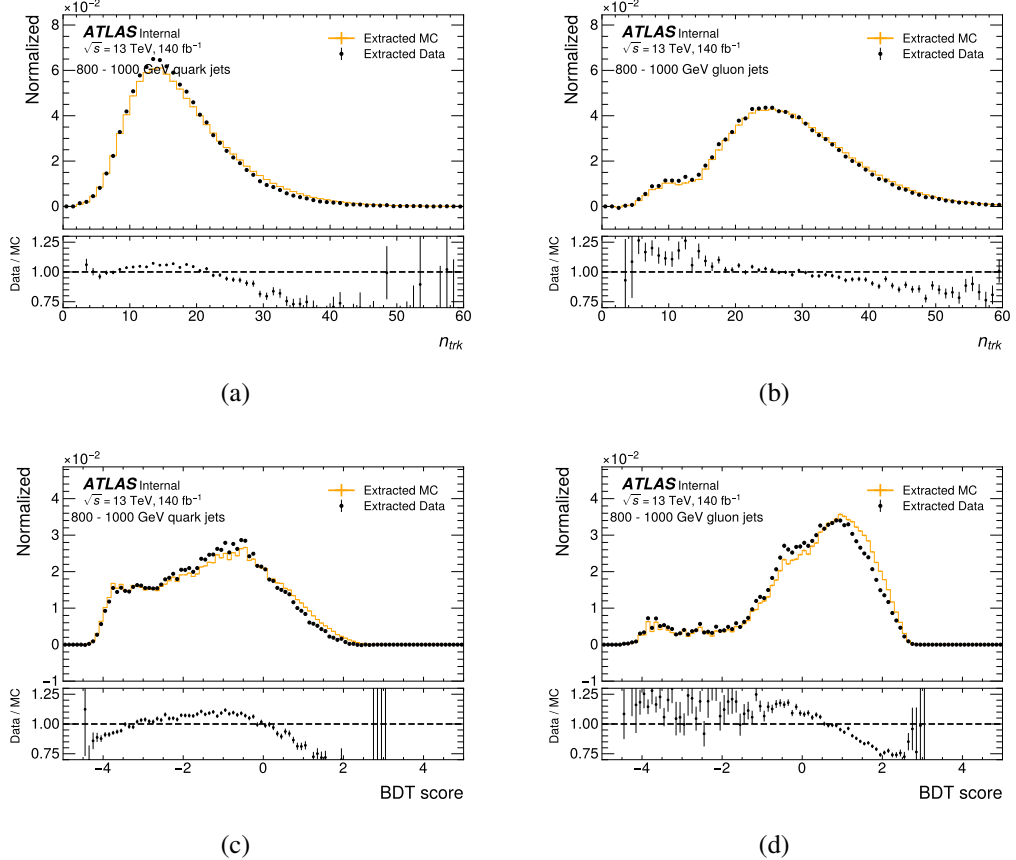


Figure 5.43 The N_{trk} (top) and BDT (bottom) distributions extracted by the matrix method from the data and MC of pure quark-jets (a) (c) and gluon-jets (b) (d) by PYTHIA 8. extracted by the matrix method from the data and MC. The gluon factor is applied. Solid-line histograms show the distributions of quark or gluon-jets defined by the jet parton flavour label in the MC. A bottom panel in each figure shows the ratio of the extracted data to the extracted MC by the matrix method.

 1242 **5.10.2 The MC non-closure**

1243 As described in Section 5.5, the MC closure test is conducted using MC samples
 1244 wherein each jet is assigned a truth label. After re-weighting, the distributions of N_{trk}
 1245 and BDT obtained through the matrix method exhibit consistency with the truth-labelled
 1246 ones for quark- and gluon-jets, respectively. The remaining difference for both taggers
 1247 is only 1% level.

 1248 **5.10.3 Statistical uncertainty**

1249 The estimation of statistical uncertainty involves a stepwise process. It commences
 1250 by varying the input data/MC distributions bin-by-bin, using Poisson/Gaussian distri-
 1251 butions wherein the number of data events within each bin serves as the central value.
 1252 These variations of the input histograms yield templates, subsequently employed as in-
 1253 puts for the template variations technique. This procedure is iterated 5000 times, with the
 1254 standard deviation of these uncertainties of all toys taken is used to derive the statistical
 1255 uncertainty of the SFs. This uncertainty is around 0.1%.

The distributions of SFs are shown in 5.44 for N_{trk} and 5.45 for the BDT.

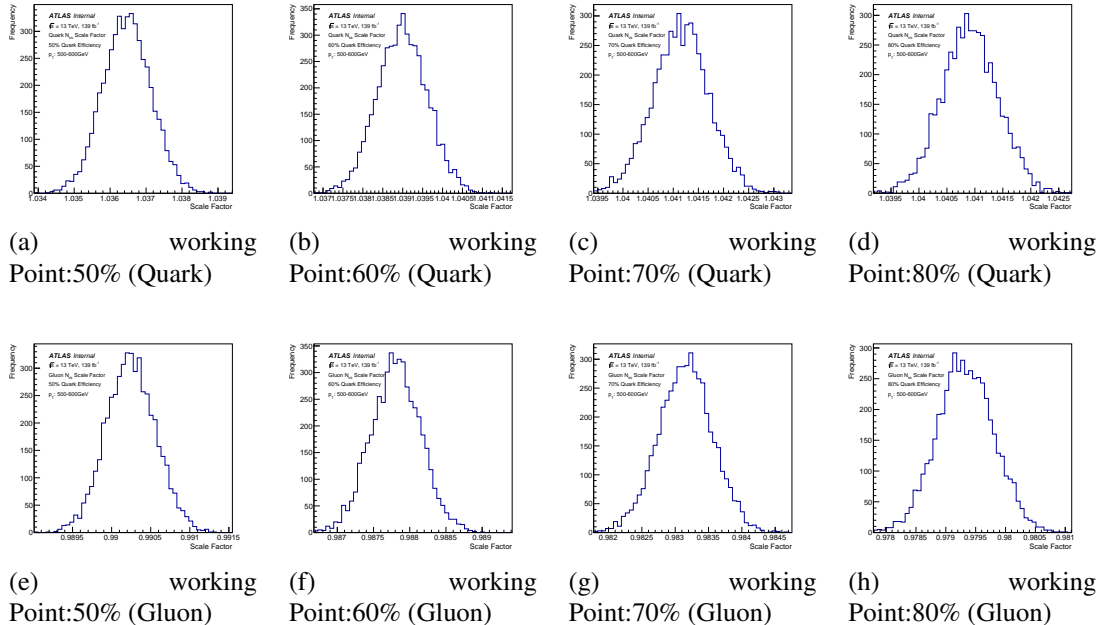


Figure 5.44 The distribution of SF by varying the input data distributions bin-by-bin using a Poisson distribution with the number of data events in each bin as the central value for 5000 times for working point of N_{trk} in jet p_T range 500-600 GeV.

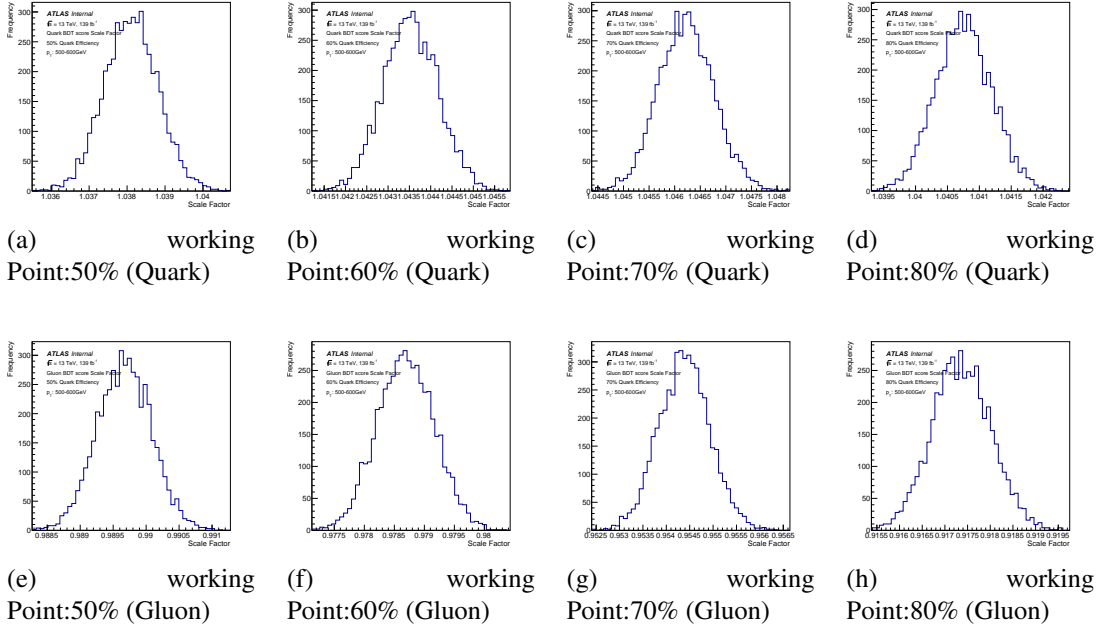


Figure 5.45 The distribution of SF by varying the input data distributions bin-by-bin using a Poisson distribution with the number of data events in each bin as the central value for 5000 times for working point of BDT in jet p_T range 500-600 GeV.

1256 5.11 Results

1257 Overall, both the N_{trk} -only tagger and the BDT-tagger exhibit commendable performance,
 1258 and can effectively distinguish quark-jet from gluon-jet with high efficiency. The
 1259 SFs for both quark- and gluon-jet fall within the range of approximately 0.9 to 1, indicating
 1260 a reasonable agreement. The systematic uncertainty for quark-jet SFs hovers around
 1261 10%, while for gluon-jet SFs it's approximately 20%. Detailed of each uncertainty are
 1262 shown in Section 5.7. The BDT-tagger showcases a slightly superior performance compared
 1263 to the N_{trk} only tagger, i.e. higher gluon-jet rejection at the same WP.

1264 The uncertainties of SF for each source of WP are estimated in each jet p_T range
 1265 are given from Table 5.6 to Table 5.13 for quark-jets. Table 5.14 to Table 5.21 show the
 1266 uncertainties of SF at each WP for gluon-jets. All systematics are ordered from largest to
 1267 smallest in p_T range 500 - 600 GeV. the systematic uncertainties associated with quark-
 1268 jet scale factors tend to be smaller than those linked to gluon-jet scale factors. Notably,

¹²⁶⁹ for both quark- and gluon-jets, these uncertainties are primarily governed by the source
¹²⁷⁰ of uncertainty stemming from parton showering.

Table 5.6 The quark scale factor (nominal) and the difference between the nominal and systematic variation results for 50% quark tag efficiency from $N_{\text{trk}}\text{tagger}$

	500-600	600-800	800-1000	1000-1200	1200-1500	1500-2000
nominal	1.02	1.04	1.04	1.03	1.02	1.01
scale variation	0.09	0.1	0.12	0.11	0.13	0.12
pdf weight	0.09	0.11	0.12	0.13	0.13	0.11
hadronization	0.09	0.07	0.06	0.05	0.04	0.04
tracking	0.08	0.07	0.06	0.05	0.05	0.04
matrix element	0.05	0.06	0.06	0.05	0.05	0.04
parton shower	0.02	0.03	0.05	0.06	0.07	0.08
MC nonclosure	0.02	0.04	0.04	0.03	0.02	0.01
splitting kernel	0.01	0.01	0.01	0.01	0.01	0.01
JES/JER	0.01	0.01	0.01	0.01	0.01	0.01
gluon reweight	0.01	0.01	0.01	0.01	0.01	0.01
Statistical	0.01	0.01	0.01	0.01	0.01	0.02
Total Uncertainty	0.19	0.19	0.21	0.21	0.22	0.19

Table 5.7 The quark scale factor (nominal) and the difference between the nominal and systematic variation results for 60% quark tag efficiency from $N_{\text{trk}}\text{tagger}$

	500-600	600-800	800-1000	1000-1200	1200-1500	1500-2000
nominal	1.03	1.04	1.04	1.03	1.01	1.01
pdf weight	0.09	0.1	0.12	0.12	0.12	0.1
tracking	0.08	0.07	0.06	0.05	0.05	0.04
scale variation	0.07	0.08	0.1	0.09	0.1	0.09
hadronization	0.06	0.05	0.04	0.04	0.03	0.03
matrix element	0.05	0.05	0.05	0.05	0.05	0.04
MC nonclosure	0.02	0.04	0.04	0.03	0.02	0.02
parton shower	0.02	0.03	0.03	0.04	0.06	0.08
splitting kernel	0.01	0.01	0.01	0.02	0.01	0.01
JES/JER	0.01	0.01	0.01	0.01	0.01	0.01
gluon reweight	0.01	0.01	0.01	0.01	0.01	0.01
Statistical	0.01	0.01	0.01	0.01	0.01	0.01
Total Uncertainty	0.16	0.17	0.18	0.18	0.18	0.17

Table 5.8 The quark scale factor (nominal) and the difference between the nominal and systematic variation results for 70% quark tag efficiency from N_{trk} tagger

	500-600	600-800	800-1000	1000-1200	1200-1500	1500-2000
nominal	1.03	1.04	1.04	1.03	1.02	1.0
pdf weight	0.08	0.09	0.11	0.11	0.11	0.08
tracking	0.07	0.06	0.05	0.05	0.04	0.03
scale variation	0.06	0.06	0.07	0.07	0.07	0.06
hadronization	0.05	0.04	0.04	0.03	0.03	0.02
matrix element	0.04	0.05	0.04	0.04	0.04	0.03
MC nonclosure	0.03	0.04	0.04	0.04	0.02	0.01
parton shower	0.02	0.02	0.02	0.03	0.04	0.05
splitting kernel	0.01	0.01	0.01	0.02	0.02	0.01
JES/JER	0.01	0.01	0.01	0.01	0.01	0.01
gluon reweight	0.01	0.01	0.01	0.01	0.01	0.01
Statistical	0.01	0.01	0.01	0.01	0.01	0.01
Total Uncertainty	0.14	0.14	0.16	0.16	0.15	0.13

 Table 5.9 The quark scale factor (nominal) and the difference between the nominal and systematic variation results for 80% quark tag efficiency from N_{trk} tagger

	500-600	600-800	800-1000	1000-1200	1200-1500	1500-2000
nominal	1.03	1.03	1.03	1.02	1.01	1.0
tracking	0.06	0.05	0.05	0.04	0.03	0.02
pdf weight	0.06	0.07	0.09	0.09	0.08	0.06
scale variation	0.03	0.04	0.05	0.04	0.04	0.05
MC nonclosure	0.03	0.04	0.04	0.03	0.02	0.01
hadronization	0.03	0.02	0.02	0.02	0.02	0.02
matrix element	0.03	0.04	0.03	0.03	0.03	0.02
parton shower	0.01	0.01	0.02	0.01	0.02	0.03
splitting kernel	0.01	0.01	0.01	0.02	0.02	0.01
JES/JER	0.01	0.01	0.01	0.01	0.01	0.01
gluon reweight	0.01	0.01	0.01	0.01	0.01	0.01
Statistical	0.01	0.01	0.01	0.01	0.01	0.01
Total Uncertainty	0.11	0.11	0.13	0.12	0.11	0.1

The calibration of quark/gluon jets taggers

Table 5.10 The quark scale factor (nominal) and the difference between the nominal and systematic variation results for 50% quark tag efficiency from BDT tagger

	500-600	600-800	800-1000	1000-1200	1200-1500	1500-2000
nominal	1.01	1.02	1.03	1.02	1.01	1.0
pdf weight	0.09	0.1	0.12	0.13	0.12	0.1
scale variation	0.09	0.1	0.12	0.12	0.13	0.1
hadronization	0.07	0.06	0.06	0.06	0.04	0.04
matrix element	0.05	0.06	0.06	0.05	0.05	0.04
tracking	0.05	0.05	0.05	0.04	0.04	0.04
MC nonclosure	0.01	0.01	0.02	0.01	0.01	0.01
parton shower	0.01	0.01	0.03	0.04	0.05	0.07
splitting kernel	0.01	0.01	0.01	0.01	0.02	0.01
gluon reweight	0.01	0.01	0.01	0.01	0.01	0.01
JES/JER	0.01	0.01	0.01	0.01	0.01	0.01
Statistical	0.01	0.01	0.01	0.01	0.01	0.02
Total Uncertainty	0.17	0.18	0.2	0.2	0.2	0.18

Table 5.11 The quark scale factor (nominal) and the difference between the nominal and systematic variation results for 60% quark tag efficiency from BDT tagger

	500-600	600-800	800-1000	1000-1200	1200-1500	1500-2000
nominal	1.02	1.03	1.04	1.03	1.02	1.01
pdf weight	0.09	0.1	0.11	0.12	0.12	0.1
scale variation	0.07	0.08	0.1	0.1	0.11	0.08
hadronization	0.06	0.05	0.05	0.05	0.03	0.04
tracking	0.05	0.05	0.05	0.04	0.04	0.04
matrix element	0.05	0.05	0.05	0.05	0.04	0.03
splitting kernel	0.01	0.01	0.01	0.01	0.02	0.01
gluon reweight	0.01	0.01	0.01	0.01	0.01	0.01
MC nonclosure	0.01	0.02	0.02	0.02	0.01	0.01
JES/JER	0.01	0.01	0.01	0.01	0.01	0.01
Statistical	0.01	0.01	0.01	0.01	0.01	0.01
parton shower	0.01	0.01	0.03	0.03	0.05	0.06
Total Uncertainty	0.15	0.16	0.18	0.18	0.18	0.15

The calibration of quark/gluon jets taggers

Table 5.12 The quark scale factor (nominal) and the difference between the nominal and systematic variation results for 70% quark tag efficiency from BDT tagger

	500-600	600-800	800-1000	1000-1200	1200-1500	1500-2000
nominal	1.03	1.04	1.04	1.03	1.02	1.02
pdf weight	0.08	0.09	0.1	0.11	0.1	0.08
scale variation	0.06	0.06	0.08	0.08	0.08	0.06
tracking	0.06	0.05	0.05	0.05	0.04	0.04
hadronization	0.05	0.04	0.04	0.04	0.03	0.03
matrix element	0.04	0.04	0.04	0.04	0.03	0.02
splitting kernel	0.01	0.01	0.01	0.02	0.01	0.01
parton shower	0.01	0.01	0.02	0.03	0.04	0.04
gluon reweight	0.01	0.01	0.01	0.01	0.01	0.01
JES/JER	0.01	0.01	0.01	0.01	0.01	0.01
MC nonclosure	0.01	0.02	0.03	0.02	0.01	0.01
Statistical	0.01	0.01	0.01	0.01	0.01	0.01
Total Uncertainty	0.13	0.13	0.15	0.15	0.15	0.12

Table 5.13 The quark scale factor (nominal) and the difference between the nominal and systematic variation results for 80% quark tag efficiency from BDT tagger

	500-600	600-800	800-1000	1000-1200	1200-1500	1500-2000
nominal	1.03	1.04	1.04	1.03	1.02	1.01
pdf weight	0.07	0.07	0.08	0.09	0.08	0.06
tracking	0.06	0.05	0.05	0.04	0.03	0.03
scale variation	0.04	0.05	0.06	0.06	0.05	0.05
hadronization	0.04	0.03	0.03	0.02	0.02	0.02
matrix element	0.03	0.04	0.03	0.03	0.02	0.02
splitting kernel	0.01	0.01	0.02	0.02	0.02	0.01
parton shower	0.01	0.01	0.02	0.02	0.02	0.03
gluon reweight	0.01	0.01	0.01	0.01	0.01	0.01
JES/JER	0.01	0.01	0.01	0.01	0.01	0.01
MC nonclosure	0.01	0.01	0.02	0.02	0.01	0.01
Statistical	0.01	0.01	0.01	0.01	0.01	0.01
Total Uncertainty	0.11	0.11	0.12	0.12	0.11	0.1

The calibration of quark/gluon jets taggers

Table 5.14 The gluon scale factor (nominal) and the difference between the nominal and systematic variation results for 50% gluon tag efficiency from N_{trk} tagger

	500-600	600-800	800-1000	1000-1200	1200-1500	1500-2000
nominal	0.99	0.98	0.98	0.96	0.94	0.92
parton shower	0.1	0.11	0.12	0.13	0.11	0.14
pdf weight	0.04	0.05	0.05	0.06	0.06	0.05
splitting kernel	0.02	0.01	0.01	0.01	0.01	0.01
tracking	0.01	0.02	0.02	0.02	0.02	0.01
hadronization	0.01	0.01	0.01	0.01	0.01	0.01
scale variation	0.01	0.01	0.01	0.01	0.01	0.01
MC nonclosure	0.01	0.01	0.02	0.04	0.06	0.07
matrix element	0.01	0.01	0.02	0.03	0.04	0.07
JES/JER	0.01	0.01	0.01	0.01	0.01	0.01
Statistical	0.01	0.01	0.01	0.01	0.01	0.02
gluon reweight	0.01	0.01	0.01	0.01	0.01	0.01
Total Uncertainty	0.11	0.12	0.13	0.15	0.15	0.18

Table 5.15 The gluon scale factor (nominal) and the difference between the nominal and systematic variation results for 60% gluon tag efficiency from N_{trk} tagger

	500-600	600-800	800-1000	1000-1200	1200-1500	1500-2000
nominal	0.99	0.98	0.97	0.95	0.92	0.91
parton shower	0.15	0.17	0.17	0.17	0.17	0.21
pdf weight	0.05	0.06	0.06	0.07	0.07	0.06
splitting kernel	0.03	0.01	0.01	0.01	0.01	0.02
scale variation	0.02	0.03	0.02	0.02	0.02	0.03
tracking	0.02	0.02	0.02	0.02	0.02	0.01
hadronization	0.01	0.01	0.01	0.01	0.01	0.01
MC nonclosure	0.01	0.02	0.02	0.04	0.07	0.08
matrix element	0.01	0.01	0.02	0.03	0.05	0.08
JES/JER	0.01	0.01	0.01	0.01	0.01	0.01
Statistical	0.01	0.01	0.01	0.01	0.01	0.03
gluon reweight	0.01	0.01	0.01	0.01	0.01	0.01
Total Uncertainty	0.17	0.18	0.18	0.2	0.2	0.25

The calibration of quark/gluon jets taggers

Table 5.16 The gluon scale factor (nominal) and the difference between the nominal and systematic variation results for 70% gluon tag efficiency from N_{trk} tagger

	500-600	600-800	800-1000	1000-1200	1200-1500	1500-2000
nominal	0.99	0.97	0.96	0.94	0.91	0.87
parton shower	0.21	0.22	0.23	0.24	0.25	0.31
pdf weight	0.06	0.06	0.07	0.08	0.08	0.07
splitting kernel	0.04	0.01	0.01	0.01	0.01	0.01
scale variation	0.04	0.04	0.03	0.04	0.03	0.04
tracking	0.02	0.02	0.02	0.02	0.01	0.01
hadronization	0.01	0.01	0.01	0.01	0.01	0.01
MC nonclosure	0.01	0.02	0.03	0.05	0.08	0.12
matrix element	0.01	0.01	0.02	0.03	0.06	0.09
JES/JER	0.01	0.01	0.01	0.01	0.01	0.01
gluon reweight	0.01	0.01	0.01	0.01	0.01	0.01
Statistical	0.01	0.01	0.01	0.01	0.01	0.03
Total Uncertainty	0.23	0.24	0.24	0.26	0.28	0.35

Table 5.17 The gluon scale factor (nominal) and the difference between the nominal and systematic variation results for 80% gluon tag efficiency from N_{trk} tagger

	500-600	600-800	800-1000	1000-1200	1200-1500	1500-2000
nominal	0.98	0.97	0.95	0.93	0.89	0.85
parton shower	0.32	0.31	0.33	0.37	0.37	0.45
scale variation	0.07	0.07	0.05	0.07	0.07	0.05
splitting kernel	0.07	0.02	0.02	0.03	0.01	0.02
pdf weight	0.06	0.07	0.07	0.09	0.09	0.08
tracking	0.01	0.01	0.01	0.01	0.01	0.01
MC nonclosure	0.01	0.03	0.04	0.06	0.1	0.15
matrix element	0.01	0.01	0.02	0.04	0.07	0.11
hadronization	0.01	0.01	0.01	0.01	0.01	0.01
JES/JER	0.01	0.01	0.01	0.01	0.01	0.01
gluon reweight	0.01	0.01	0.01	0.01	0.01	0.01
Statistical	0.01	0.01	0.01	0.01	0.01	0.03
Total Uncertainty	0.34	0.33	0.34	0.39	0.41	0.49

The calibration of quark/gluon jets taggers

Table 5.18 The gluon scale factor (nominal) and the difference between the nominal and systematic variation results for 50% gluon tag efficiency from BDT tagger

	500-600	600-800	800-1000	1000-1200	1200-1500	1500-2000
nominal	1.0	0.99	0.98	0.96	0.94	0.92
parton shower	0.09	0.08	0.1	0.1	0.1	0.13
pdf weight	0.04	0.04	0.05	0.05	0.06	0.04
splitting kernel	0.03	0.02	0.02	0.02	0.01	0.02
scale variation	0.01	0.01	0.01	0.01	0.01	0.03
MC nonclosure	0.01	0.02	0.03	0.05	0.06	0.09
hadronization	0.01	0.01	0.01	0.01	0.01	0.01
tracking	0.01	0.01	0.01	0.01	0.01	0.01
matrix element	0.01	0.01	0.02	0.02	0.04	0.07
gluon reweight	0.01	0.01	0.01	0.01	0.01	0.01
JES/JER	0.01	0.01	0.01	0.01	0.01	0.01
Statistical	0.01	0.01	0.01	0.01	0.01	0.02
Total Uncertainty	0.11	0.1	0.11	0.13	0.14	0.18

Table 5.19 The gluon scale factor (nominal) and the difference between the nominal and systematic variation results for 60% gluon tag efficiency from BDT tagger

	500-600	600-800	800-1000	1000-1200	1200-1500	1500-2000
nominal	0.99	0.98	0.97	0.95	0.93	0.91
parton shower	0.11	0.12	0.13	0.13	0.14	0.17
pdf weight	0.05	0.05	0.05	0.06	0.06	0.06
splitting kernel	0.05	0.03	0.03	0.03	0.01	0.04
MC nonclosure	0.02	0.03	0.04	0.06	0.08	0.1
scale variation	0.02	0.02	0.02	0.02	0.02	0.05
hadronization	0.01	0.01	0.01	0.01	0.02	0.01
tracking	0.01	0.01	0.01	0.01	0.01	0.01
matrix element	0.01	0.01	0.02	0.03	0.04	0.08
gluon reweight	0.01	0.01	0.01	0.01	0.01	0.01
JES/JER	0.01	0.01	0.01	0.01	0.01	0.01
Statistical	0.01	0.01	0.01	0.01	0.01	0.02
Total Uncertainty	0.13	0.14	0.15	0.16	0.18	0.23

The calibration of quark/gluon jets taggers

Table 5.20 The gluon scale factor (nominal) and the difference between the nominal and systematic variation results for 70% gluon tag efficiency from BDT tagger

	500-600	600-800	800-1000	1000-1200	1200-1500	1500-2000
nominal	0.98	0.97	0.95	0.93	0.89	0.86
parton shower	0.15	0.15	0.17	0.17	0.17	0.21
splitting kernel	0.07	0.05	0.05	0.04	0.03	0.05
pdf weight	0.05	0.06	0.06	0.07	0.07	0.06
MC nonclosure	0.05	0.05	0.07	0.09	0.12	0.15
scale variation	0.03	0.04	0.03	0.04	0.04	0.07
hadronization	0.02	0.01	0.01	0.01	0.01	0.01
tracking	0.01	0.01	0.01	0.01	0.01	0.01
matrix element	0.01	0.01	0.02	0.03	0.05	0.08
JES/JER	0.01	0.01	0.01	0.01	0.01	0.01
gluon reweight	0.01	0.01	0.01	0.01	0.01	0.01
Statistical	0.01	0.01	0.01	0.01	0.01	0.02
Total Uncertainty	0.18	0.18	0.2	0.21	0.23	0.29

Table 5.21 The gluon scale factor (nominal) and the difference between the nominal and systematic variation results for 80% gluon tag efficiency from BDT tagger

	500-600	600-800	800-1000	1000-1200	1200-1500	1500-2000
nominal	0.96	0.95	0.93	0.9	0.85	0.81
parton shower	0.19	0.18	0.21	0.2	0.22	0.28
splitting kernel	0.09	0.07	0.06	0.06	0.05	0.07
MC nonclosure	0.08	0.09	0.1	0.12	0.17	0.21
pdf weight	0.06	0.06	0.07	0.08	0.08	0.06
scale variation	0.05	0.05	0.05	0.05	0.07	0.08
hadronization	0.02	0.01	0.01	0.01	0.01	0.01
tracking	0.01	0.01	0.01	0.01	0.01	0.01
matrix element	0.01	0.01	0.02	0.03	0.06	0.09
JES/JER	0.01	0.01	0.01	0.01	0.01	0.01
Statistical	0.01	0.01	0.01	0.01	0.01	0.03
gluon reweight	0.01	0.01	0.01	0.01	0.01	0.02
Total Uncertainty	0.23	0.23	0.25	0.26	0.31	0.38

1271 Figure 5.46 to Figure 5.49 show the leading uncertainties with SFs for both tagger.
1272 The SFs for quark-jets and gluon-jets corresponding to the 50% quark-jets efficiency
1273 working point (WP) fall within the range of 0.92 to 1.02, while being subject to an ag-
1274 gregate systematic uncertainty of approximately 20%. Among the various sources of
1275 systematic uncertainty, theoretical modelling emerges as the dominant factor contribut-
1276 ing to the total uncertainty.

1277 To ascertain the robustness of the findings, tests are conducted to assess the stabili-
1278 ty of results across different regions of jet $|\eta|$. The SF measurements are recomputed
1279 through the normalization of jet $|\eta|$ in the quark-/gluon-enriched subsamples. The al-
1280 ternate results obtained in this manner are determined to be consistent with the nominal
1281 outcome, falling within the full range of reported uncertainties.

1282 Given the variations in the usage of different MC samples, a MC-to-MC SF is com-
1283 puted. This involves employing each alternative MC sample while treating the PYTHIA MC
1284 samples as pseudodata. This approach accommodates discrepancies arising from mod-
1285 elling difference between the PYTHIA and alternative MC samples. The MC-to-MC SFs
1286 for both jet taggers at each WP are shown in Figure 5.50 to Figure 5.53. Notably, there
1287 exists a large difference in gluon modelling between the HERWIG Dipole parton shower
1288 MC and the PYTHIA MC. This discrepancy is reflected in the relatively significant MC-
1289 to-MC SF, indicating substantial differences between these models.

The calibration of quark/gluon jets taggers

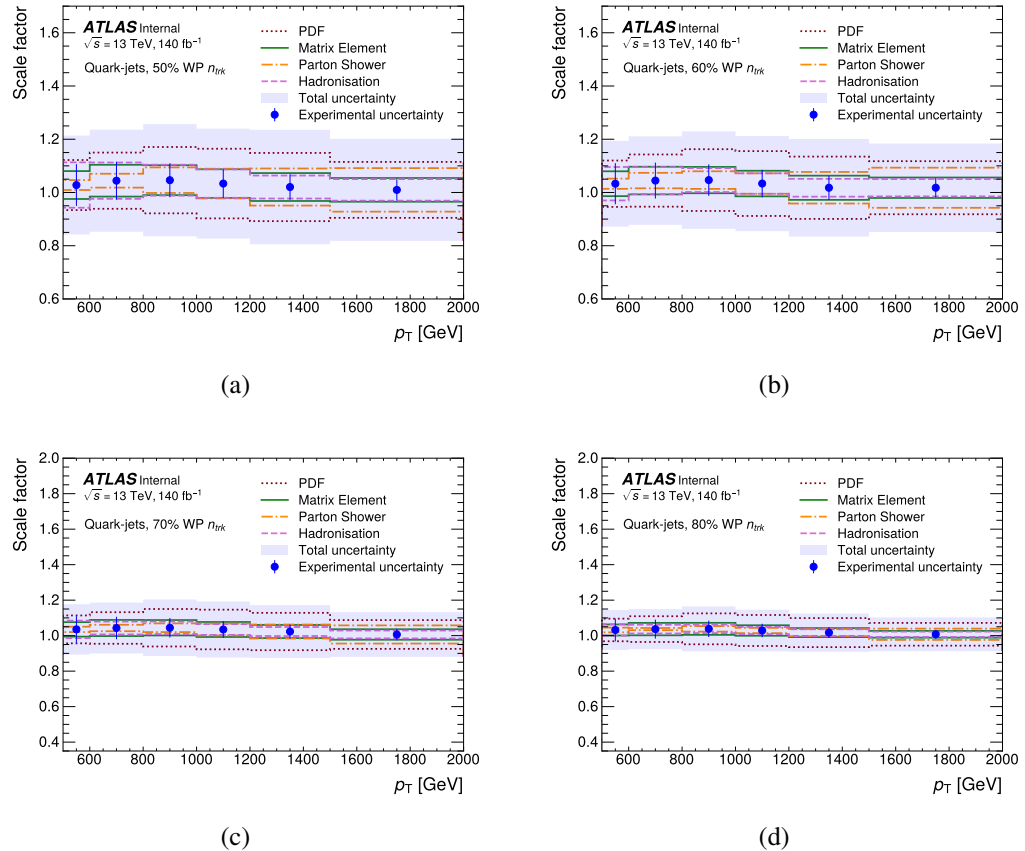


Figure 5.46 The SF with total and leading systematic uncertainty on the jet tagging variable N_{trk} obtained by PYTHIA 8 MCs as a function of jet p_T for quark-jets at each WP.

The calibration of quark/gluon jets taggers

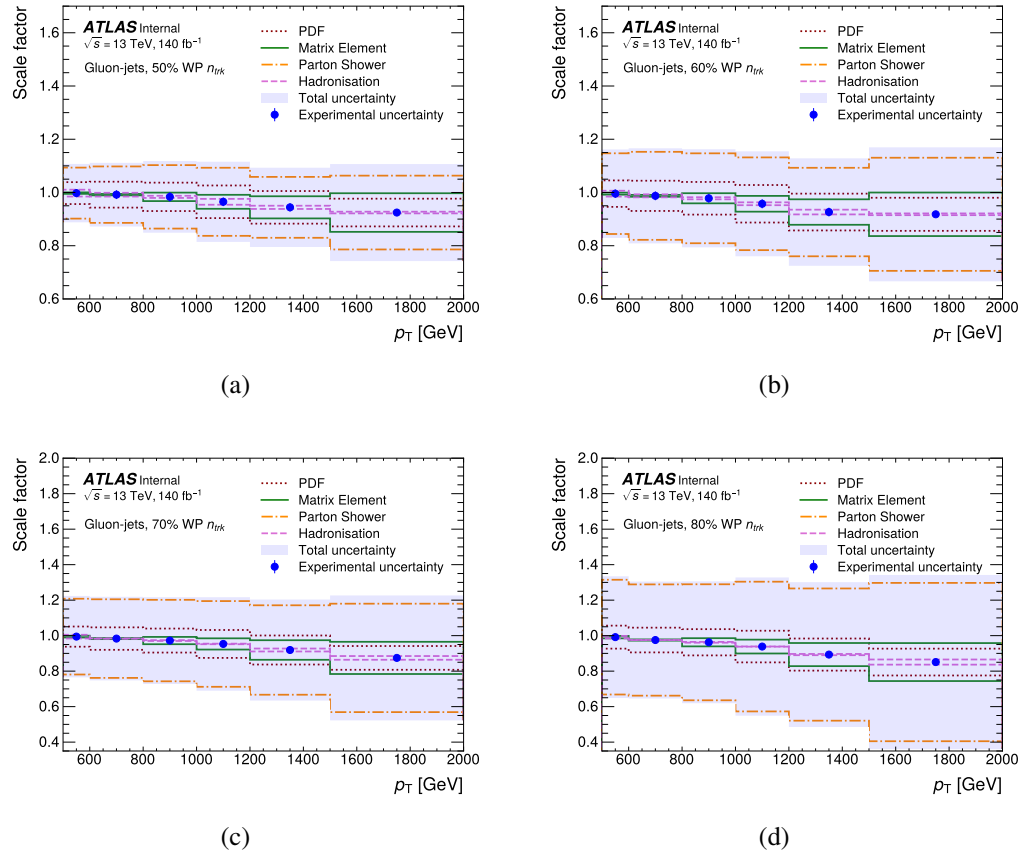


Figure 5.47 The SF with total and leading systematic uncertainty on the jet tagging variable N_{trk} obtained by PYTHIA 8 MCs as a function of jet p_T for gluon-jets at each WP.

The calibration of quark/gluon jets taggers

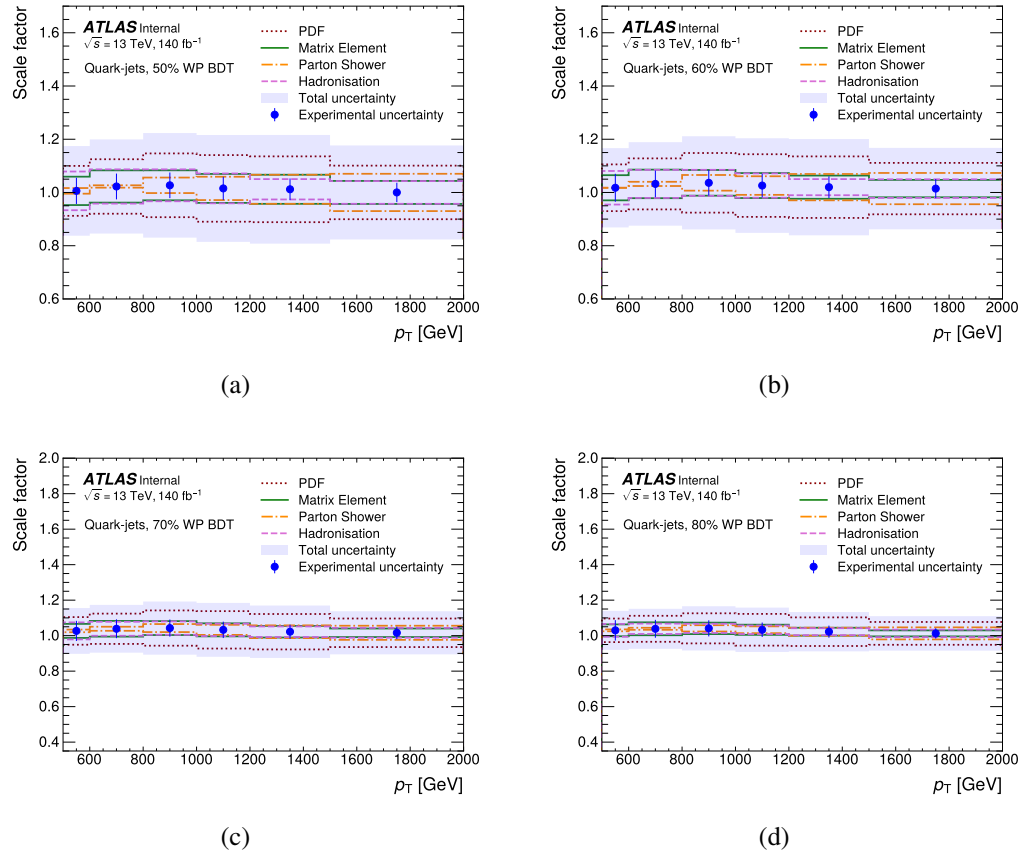


Figure 5.48 The SF with total and leading systematic uncertainty on the jet tagging variable BDT obtained by PYTHIA 8 MCs as a function of jet p_T for quark-jets at each WP.

The calibration of quark/gluon jets taggers

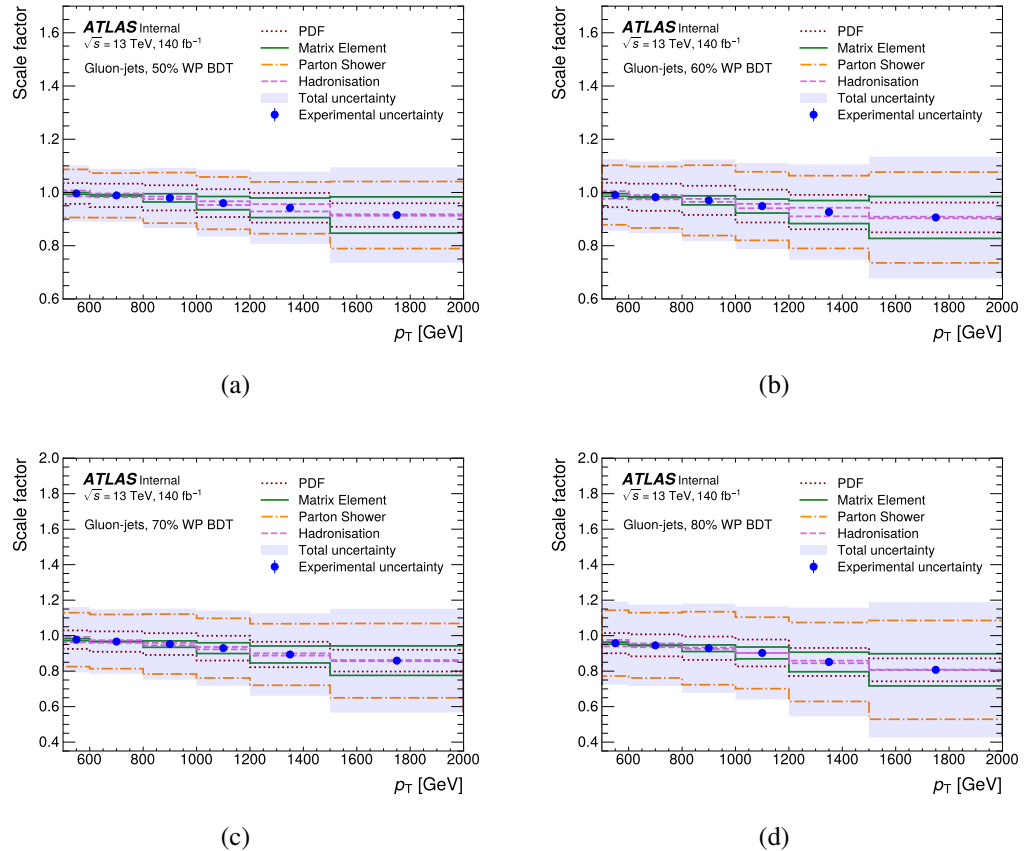


Figure 5.49 The SF with total and leading systematic uncertainty on the jet tagging variable BDT obtained by PYTHIA 8 MCs as a function of jet p_T for gluon-jets at each WP.

The calibration of quark/gluon jets taggers

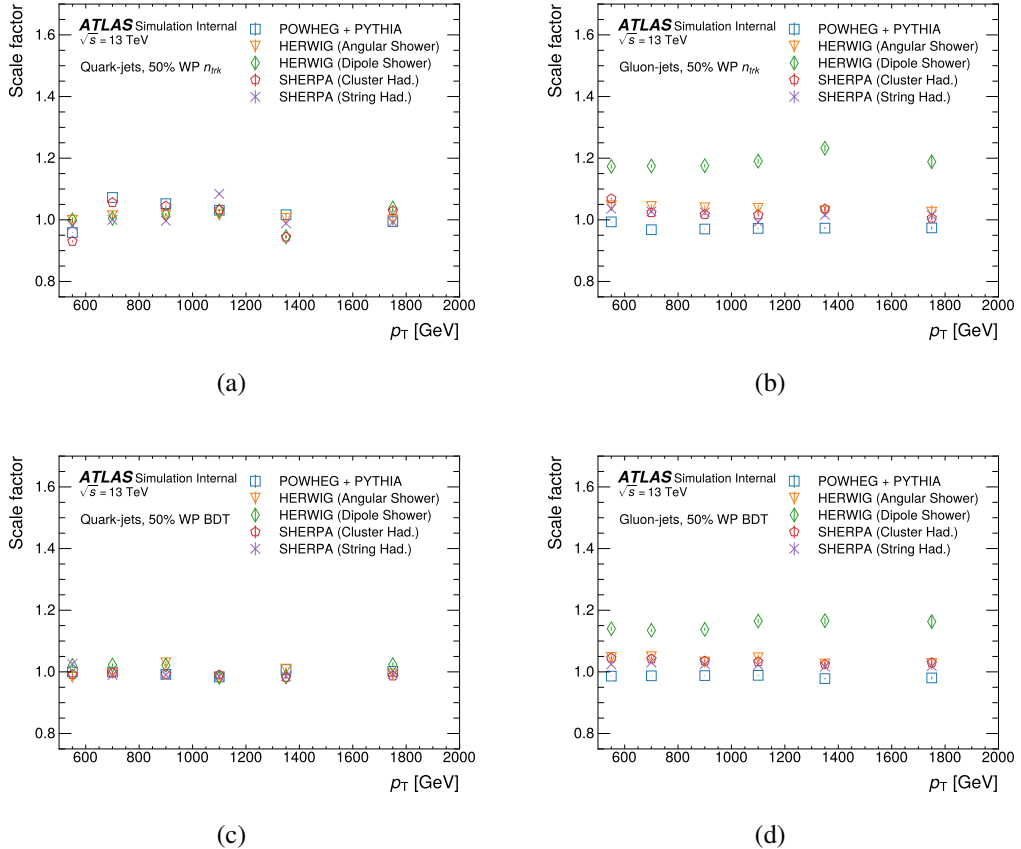


Figure 5.50 The MC-to-MC SF of the N_{trk} , (a) and (b), and BDT, (c) and (d), as a function of jet p_T for quark-jets (left) and gluon-jets (right) at the 50% WP. The vertical error bars show the statistical uncertainty.

The calibration of quark/gluon jets taggers

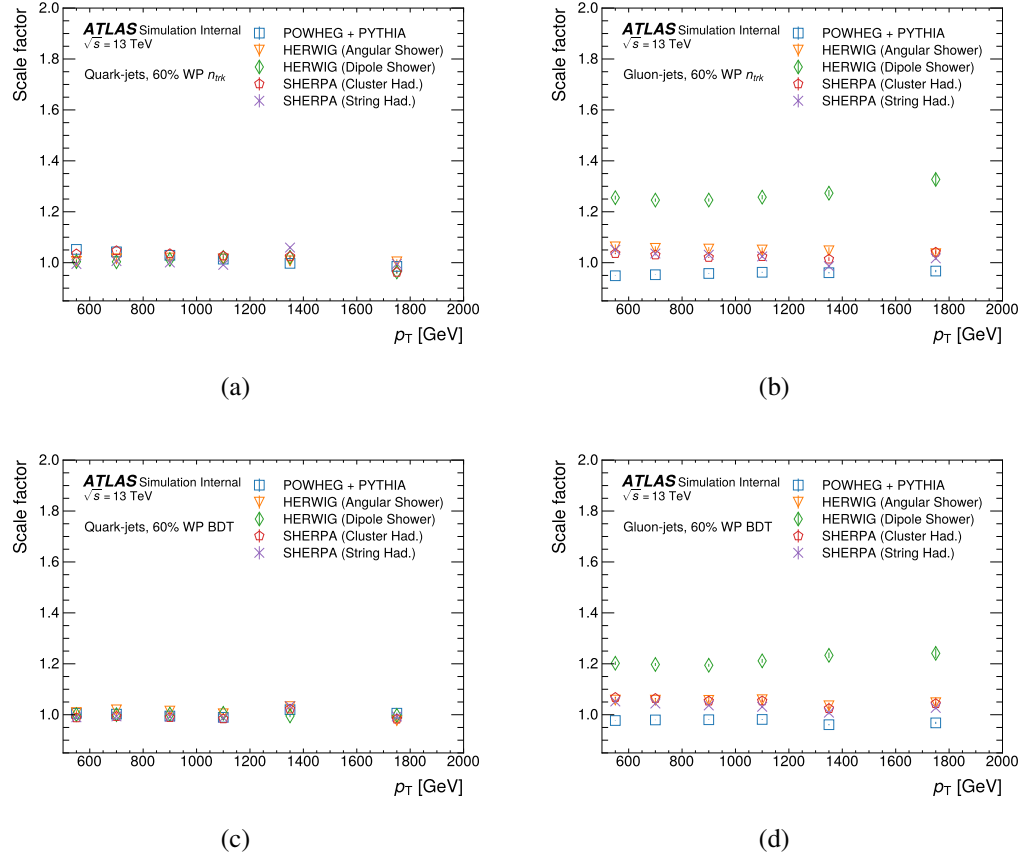


Figure 5.51 The MC-to-MC SF of the N_{trk} , (a) and (b), and BDT, (c) and (d), as a function of jet p_T for quark-jets (left) and gluon-jets (right) at the 60% WP. The vertical error bars show the statistical uncertainty.

The calibration of quark/gluon jets taggers

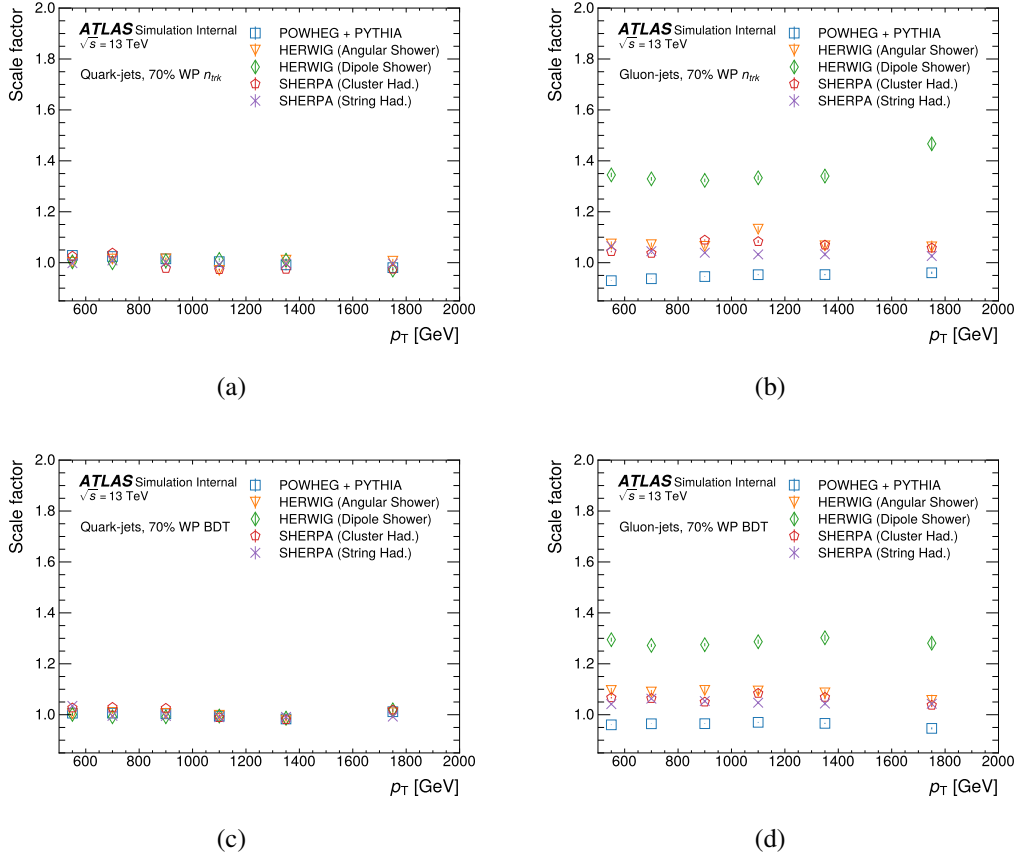


Figure 5.52 The MC-to-MC SF of the N_{trk} , (a) and (b), and BDT, (c) and (d), as a function of jet p_T for quark-jets (left) and gluon-jets (right) at the 70% WP. The vertical error bars show the statistical uncertainty.

The calibration of quark/gluon jets taggers

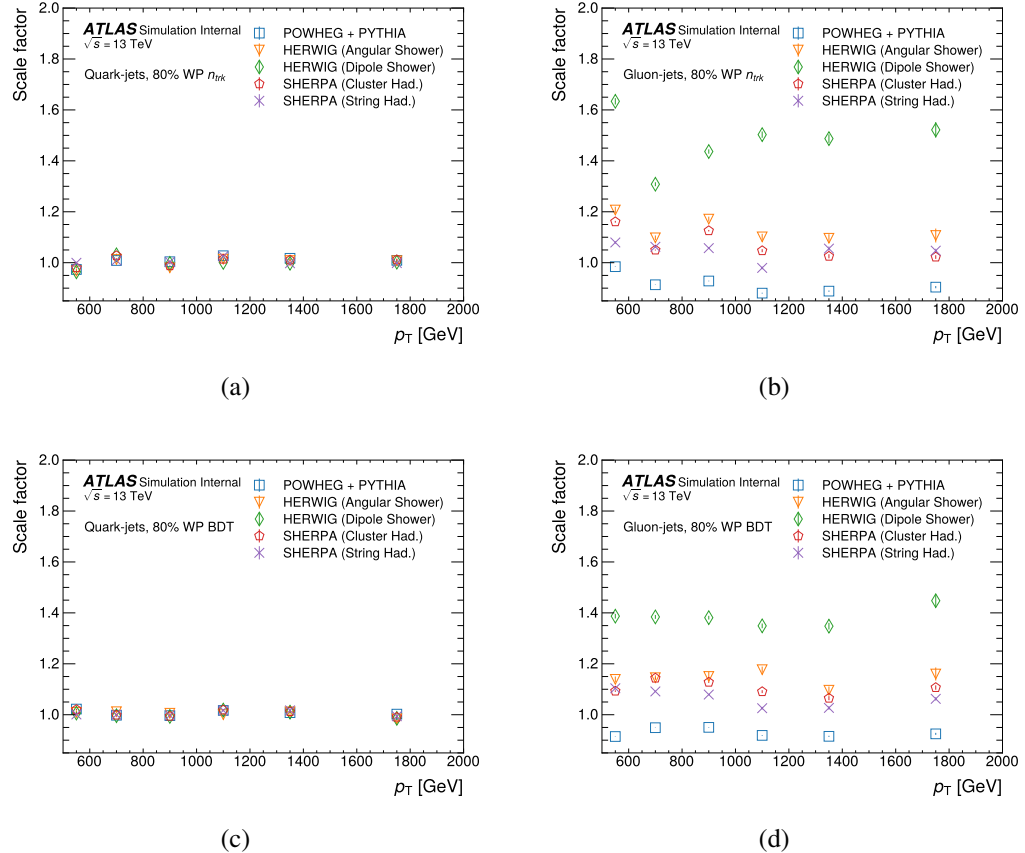


Figure 5.53 The MC-to-MC SF of the N_{trk} , (a) and (b), and BDT, (c) and (d), as a function of jet p_T for quark-jets (left) and gluon-jets (right) at the 80% WP. The vertical error bars show the statistical uncertainty.

1290

5.12 Conclusions

1291 The analysis focuses on evaluating the performance of jet taggers for quark- and
1292 gluon-jets using a dataset of 140 fb^{-1} obtained from pp collisions at a centre-of-mass en-
1293 ergy of $\sqrt{s} = 13 \text{ TeV}$, gathered by the ATLAS detector at the LHC. This study leverages
1294 the extensive dataset recorded between 2015 and 2018 to extend the taggers' applicabil-
1295 ity to high-energy jets. Two distinct jet tagging methods are explored: a tagger centred
1296 on the charged-particle jet constituent multiplicity (N_{trk}), and a BDT-based tagger, which
1297 integrates various individual jet substructure observables.

1298 The matrix method is adopted to estimate the distribution shapes of the tagging
1299 variables for quark- and gluon-jets. This entails combining information from samples
1300 enriched with quark- and gluon-jets, acquired from a selection of dijet events charac-
1301 terized by jet p_{T} ranging from 500 GeV to 2 TeV. The considered variables exhibit a
1302 satisfactory agreement with the MC simulations, with discrepancies relative to data mea-
1303 surements being less than 25% across various defined regions.

1304 The BDT-tagger demonstrates superior performance over the N_{trk} -only tagger in
1305 distinguishing quark-jets from gluon-jets within the jet p_{T} range of 500 GeV to 1200
1306 GeV. Above this range, the performance of the two taggers becomes comparable.

1307 The evaluation of tagger performance differences between data and MC samples
1308 is facilitated through the data-to-MC SFs. These factors are measured across varying
1309 jet- p_{T} intervals, exhibiting a range from 0.92 to 1.02, with a cumulative uncertainty of
1310 approximately 20%. The primary contributor to this uncertainty stems from divergent
1311 modelling choices within MC simulations, constituting approximately 18% for both tag-
1312 gers. To account for variations between different MC generators, MC-to-MC SFs are
1313 also presented, ranging from 0.9 to 1.1 for the majority of MC samples.

1314 The q/g taggers developed in this study and the associated measurement of their SFs
1315 hold relevance for various analyses. These applications encompass SM measurements
1316 that rely on accurate jet origin identification, as well as BSM physics searches that can
1317 capitalize on heightened sensitivity to the presence of new particles.

1318

6 Search for new phenomena in dijet events

1319 As described in Section 2, the heavy resonance predicted by many BSM play a key role
1320 in understanding many fundamental phenomena. The narrow heavy resonance which
1321 decays into two gluons final state at the LHC, appears to be two hadronic jets in the
1322 detector. Produced by the QCD processes, the dijet events have a smoothly falling dis-
1323 tribution of the invariant mass m_{jj} , whereas two jets appear to be a resonance in the
1324 m_{jj} spectrum. As a result, searches for dijet resonance are one of the flagship exotics
1325 analyses in ATLAS.

1326 Besides, on the assumption that the resonant sample can be classified according to
1327 the type of parton that initiated the jets, the sensitivity of searches for new resonance
1328 can be improved by identifying the types of partons through which the potentially new
1329 particle interact. One of simplest examples of such tagging is gluon-tagging one or more
1330 of the jets. The jet tagging procedure based on the number of charged tracks with trans-
1331 verse momentum p_T above 500 GeV is described in Section. 5. The m_{jj} spectrum of
1332 background is estimated from the data, which is used for the search in three categories:
1333 inclusive, single-gluon, and double-gluon tagged dijet systems. The inclusive m_{jj} spec-
1334 trum is thus considered as control region for quark/gluon studies.

1335 This chapter describes searches for new heavy particles decay in dijet final state
1336 as originating from gluons or quarks, a technique of quark/gluon tagging is employed
1337 to enhance the sensitivity to the results. The search performed uses full Run 2 data
1338 at $\sqrt{s} = 13$ TeV, with higher integrated luminosity compared to previous one (Run 1),
1339 significantly improvements in the understanding of systematic uncertainties are expected.
1340 On the other hand, cross section upper limits will be set if no significantly resonances
1341 are observed.

1342

The simplified procedures in this analysis is performed as following:

1343

- Search for high-mass resonances in the untagged (inclusive), single-gluon tagged,
1344 and two-gluon tagged categories with dijet events.
- If significant resonances are found, claim something interesting, else the upper
1345 limits are set.
- Model independent upper-limits are set on resonance cross sections in inclusive,
1346 single-gluon tagged, and two-gluon tagged categories.

- 1349 • For the specific resonance model, set lower limits on the relevant scales in inclu-
1350 sive, single-gluon tagged, and two-gluon tagged categories. dijet systems.

1351 **6.1 Monte Carlo models**

1352 . This section outlines benchmark models for both background from the QCD and
1353 for new physics signals that encapsulated in the models chosen: H' , Strings, and QBH.
1354 Full Run 2 data are used to produce EXOT2 skimmed samples used in this analysis.

1355 **6.1.1 QCD background**

1356 QCD processes from the MC are simulated at LO and NLO in SM perturbative
1357 theory. Due to the large range in cross section of QCD sample, the samples are thus
1358 sliced based on the leading jet p_T , to obtain comparable statistical precision across the
1359 jet p_T range of interest.

1360 **6.1.2 H'**

1361 This analysis performs a model-independent search for two-gluon resonances at
1362 high m_{jj} spectrum, as the CCD background is dominated by valence quark scattering,
1363 gluon tagging in this case could be effective.

1364 The simulated SU(3) singlet scalar that decay via PYTHIA 8 with the A14 set of
1365 tuned parameters is used in this analysis¹. The HiggsBSM:gg2H2, where set the singlet
1366 scalar as H2 particle and has Particle Data Group ID 35. Such H2 particle is set to
1367 decay to gluons and has a narrow resonances width of 0.1 GeV as the physical width is
1368 model-dependent but constrained by the detector resolution.

1369 The benchmark signals used vary in their underlying physics motivation, but also
1370 in the resulting shape of the signal m_{jj} distribution. The peaks of signal shape are set for
1371 various mass points as shown in Figure 6.54, the distributions are normalized to unity
1372 and thus the differences in peak amplitudes are not the changes in cross section.

¹See <https://its.cern.ch/jira/browse/ATLMCPROD-6155>.

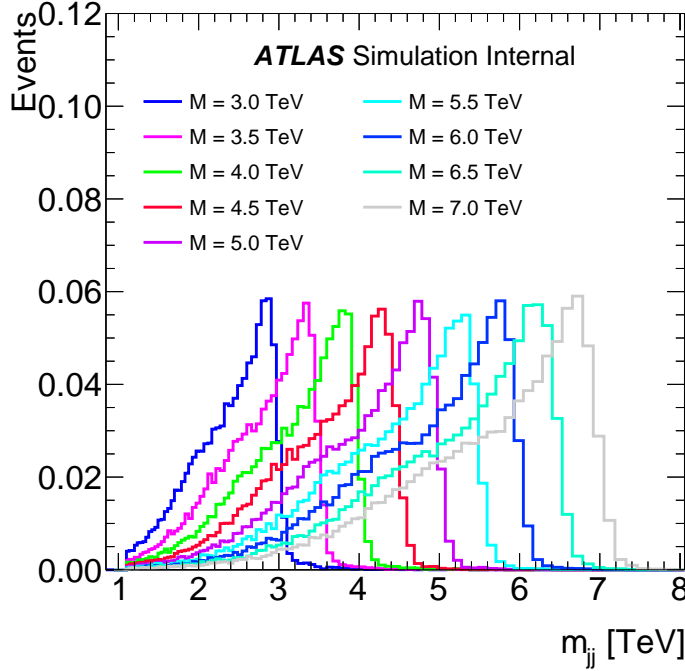


Figure 6.54 Signal shapes for the H' signal at different mass points.

6.1.3 Strings

As the SM has lots of well known problems such as the quadratically divergent corrections to the Higgs self-energy, supersymmetry theory offers a solution to it by fine-tuning the cancellation. The superstring theory, addition to the supersymmetry, can perform as a framework that unify theories from SM at TeV-scale to quantum gravity at Planck-scale .

The fundamental string scale is chosen to be within TeV scale, dotes as string mass-scale M_s . The string resonances could happen at masses $m_n = \sqrt{n}M_s$, for $n = 1, 2, 3, \dots$, where the resonance consist of the Regge excitations of quark, gluon, as well as the colour singlet that lives on the QCD stack of branes. In total, five string scales M_s range from 7.0 TeV to 9.0 TeV, in steps of 0.5 TeV are generated for string-resonance samples. The lower limits of mass M_{\min} provided in the generator are shown in Table 6.22, together with the resulting cross section of the string samples.

As the string resonances have long Breit-Wigner tails, the PDFs at low- x (low mass) can significantly enhance the tail. In this study, the low-mass tail is truncated since only narrow-resonance structure in m_{jj} spectrum is interesting to this analysis. In the range $7.0 \leq M_s \leq 8.0$ TeV, the truncation is done at the minimum value in the differential cross

M_s [TeV]	M_{\min} [TeV]	Cross section [fb]
7.0	6.06	7.09E+0
7.5	6.60	1.86E+0
8.0	7.14	4.56E-1
8.5	7.60	1.00E-1
9.0	8.05	1.99E-2

Table 6.22 MC string-resonance samples with string scale M_s , minimum mass M_{\min} , and cross section.

1390 section on the lower-mass side of the M_s peak, results in around 95% of the area under
 1391 the Breit-Wigner curve. In the range $7.0 \leq M_s \leq 8.0$ TeV, the truncation is done at a
 1392 lower-mass point that covers 95% of the area under the Breit-Wigner curve.

1393 The distribution of signal peak at different mass points is shown in Figure 6.55, the
 1394 distributions are normalized to unity and thus the differences in peak amplitudes are not
 1395 the changes in cross section.

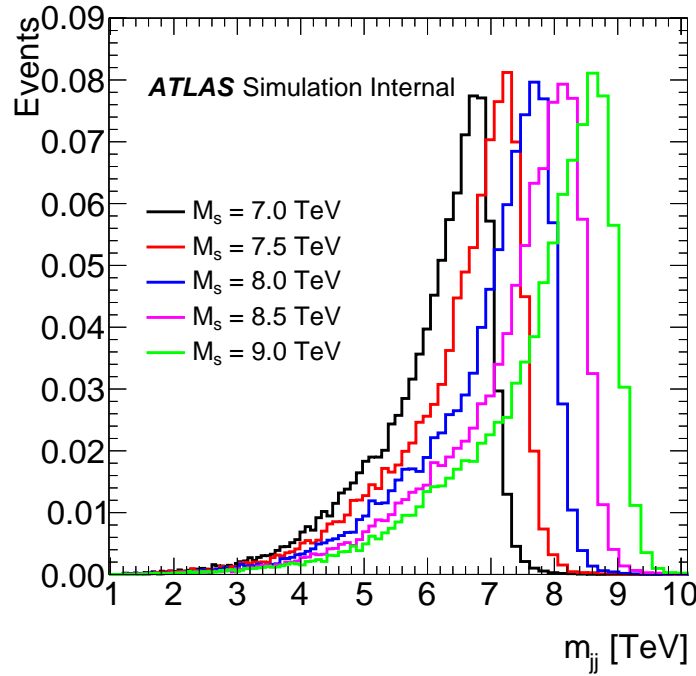


Figure 6.55 Signal shapes for the String signal.

1396 There are five possible $2 \rightarrow 2$ subprocesses from string resonances are simulated.

1397 with the cross section for each subprocess vary as a function of M_s shown in Table 6.23.
 1398 The dominate subprocess across the M_s values is considered to be $gq \rightarrow gq$, which con-
 1399 tributes around 81-87% of the total cross section. The rest of subprocesses: $qq \rightarrow qq$,
 1400 $\bar{q}\bar{q} \rightarrow \bar{q}\bar{q}$, and $q\bar{q} \rightarrow q\bar{q}$ are model dependent and thus do not included in this analysis.

Subprocess	M_s [TeV]				
	7.0	7.5	8.0	8.5	9.0
$gg \rightarrow gg$	11.4%	9.5%	8.2%	7.2%	5.1%
$gg \rightarrow q\bar{q}$	0.3%	0.3%	0.2%	0.2%	0.2%
$gq \rightarrow gq$	81.4%	83.1%	84.6%	85.5%	87.6%
$g\bar{q} \rightarrow g\bar{q}$	0.7%	0.6%	0.5%	0.5%	0.5%
$q\bar{q} \rightarrow gg$	6.3%	6.5%	6.5%	6.5%	6.7%

Table 6.23 String-resonance subprocesses and their relative contributions to the total cross section at each string scales M_s . The statistics are based on samples of 66000 events.

1401 For generating string samples, the MC event generator STRINGS 1.00 [81] with
 1402 interfaced to PYTHIA 8.240 for parton shower modelling is used, together with the A14
 1403 tune. The CTEQ6L1 [76] PDF set at the LO is used for the parton shower and the hard-
 1404 scattering process. The decaying processes is simulated using the EvtGen 1.6.0 program.

1405 The effect from pile-up is simulated by overlaying the MC inelastic pp events gen-
 1406 erated with PYTHIA 8.186 with a PDF set of NNPDF2.3 at LO and the A3 tune over the
 1407 original hard-scattering events.

1408 6.1.4 Quantum Black Holes

1409 In our study, we employ the QBH model for the purpose of comparing limits with
 1410 the previous iteration of the analysis. The feasibility of producing QBHs at the LHC is
 1411 contingent upon the presence of sufficiently large extra dimensions within the universe.
 1412 This model posits that the energy scale of quantum gravity M_D , at which QBHs are gen-
 1413 erated, diminishes as the number of these large extra dimensions, denoted as n , increases.
 1414 Consequently, a larger n permits lower mass scales at which QBHs can be formed.

1415 Two-body isotropic final state is expected by the QBH decay at the LHC, where
 1416 the M_D energy threshold could be reached. Therefore the quantum gravitational effects
 1417 can be probed by searches on m_{jj} spectrum. To simulate events involving quantum black

₁₄₁₈ holes with $n = 6$, we utilize the BlackMax [53] MC generator. This MC generator facil-
₁₄₁₉ itates the simulation of QBH events within the $n = 6$ framework..

1420 6.2 Events selections

1421 The MC and data events are divided into three categories to perform the search:
 1422 the untagged dijet invariant mass spectrum, one-gluon tagged spectrum, and two-gluon
 1423 tagged spectrum. The evidence of BSM resonances would appear as peaks in the m_{jj}
 1424 spectrum formed by two highest p_T jets in the events. A series of specific cuts is applied
 1425 to improved the sensitivity of the searches.

1426 6.2.1 Observables and Kinematic Variables

1427 The predominant source of dijet events in the SM is two-to-two scattering though
 1428 the QCD processes. This search exams two key properties of the QCD background:

- 1429 • The background at high m_{jj} appears as a smooth and continuously falling spec-
 1430 trum.
- 1431 • The background at high energy strongly peaks in the forward region as a result
 1432 of Rutherford t - and u -channel poles in the cross sections for certain scattering
 1433 processes [62].

1434 Resonances of interest have $\cos \theta$ distributions in the detector, which in contrast to
 1435 Rutherford scattering, are either isotropic or have polynomial behaviour in $\cos \theta$ ², thus
 1436 a angular distribution appears. This search therefore defines a y^* to indicate the angle
 1437 separation of the jets in the selected events:

$$y^* = (y_1 - y_2)/2 \quad (6.1)$$

1438 to improve the sensitivity to higher energies where new phenomena are expected. The
 1439 variables y_1, y_2 represent the rapidity of the leading and subleading jet. The value of the
 1440 y^* cut on events is optimized for each signal as discussed in Section .6.4.1.

1441 In this analysis, jets are reconstructed with the anti- k_t algorithm with a radius pa-
 1442 rameter $R = 0.4$, as implemented in the FASTJET package [38]. The EMTopo jets, re-
 1443 constructed from topological clusters via procedures described in Section .4.1, are used.
 1444 The standard *Loose* cut is applied to jet quality as well as jet cleaning. The summarized
 1445 jet criteria are shown in Table 6.24.

²See Ref. [62] p15 for a summary.

Parameter / Observable	Requirement
Algorithm	anti- k_t
R-parameter	0.4
Input Constituent	EMTopo
p_T	>150 GeV
$ \eta $	<2.1

Table 6.24 Jet selection criteria used in this analysis.

6.2.2 Baseline selection

The triggers used in this analysis is HLT_j420. Besides, two single-jet trigger HLT_j225_gsc420_boffperf_split is also used as the unprescaled trigger for full Run 2 data. Both triggers have the threshold of $p_T > 420$ GeV of the jets, while the GSC is applied to the HLT_j225_gsc420_boffperf_split to the trigger turn-on improvement. A turn-on based on the m_{jj} spectrum is found to be much powerful than the cut requirement of the leading jet p_T , where the m_{jj} cut imposes a soft cut on the leading and subleading jet, respectively. More details are shown in Section 6.4.2.

The baseline event selection is applied for all categories. The GRL and various flags that indicate the status of detector when taking data are provided by the ATLAS Data Quality (DQ) group, are applied to ensure the data integrity. Primary vertex requirement is also included to ensure good quality jets. The

- All jets with $p_T > 150$ GeV pass *Loose* cleaning cuts
- Passes the lowest unprescaled single-jet trigger: HLT_j420
- Jet multiplicity ≥ 2
- Leading jet $p_T > 380$ GeV and subbeading jet $p_T > 150$ GeV
- Leading jet $|\eta| < 2.1$ and subbeading jet $|\eta| < 2.1$
- $|\Delta\phi|$ between two jets: $|\Delta\phi| > 1.0$
- $m_{jj} > 1100$ GeV

Additional kinematic criteria are applied according to the distributions of signals, in order to optimize the search potential, are then discussed in Section 6.4.1.

6.3 Quark-Gluon Sample Selection

1467 . The sensitivity of the search on the resonant is expected to increase by distinguishing the type of parton that initiated the jets. The parton types of dijet events as a
 1469 function of m_{jj} from the MC with a PYTHIA8.186 at LO NNPDF2.3 PDFs is shown in
 1470 Figure 6.56, suggesting that the search for new resonance can be improved by tagging
 1471 quark and gluon jets.

1473 In this section we present the search for new particles using the full Run 2 $\sqrt{s} =$
 1474 13 TeV dataset with quark and gluon tagging method.

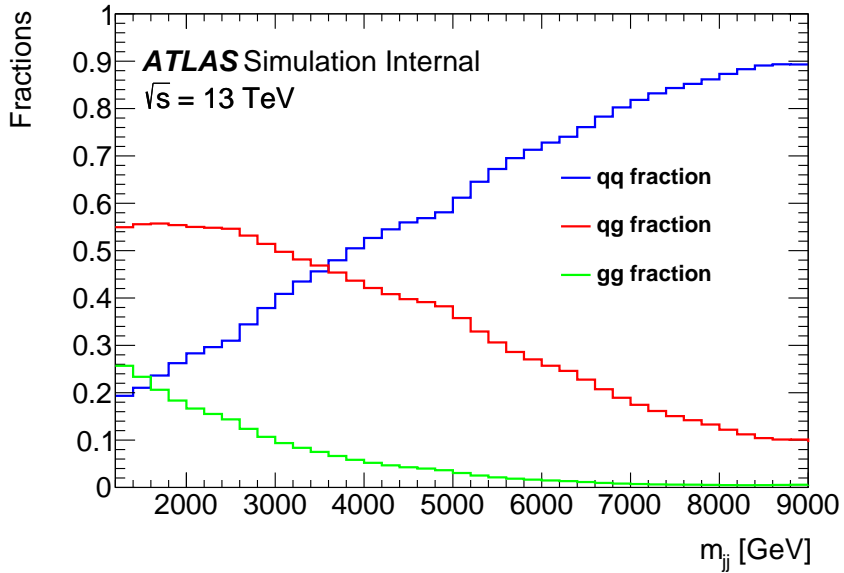


Figure 6.56 The fraction of dijet events that are initiated by quark-quark events (blue), quark-gluon events (green) and gluon-gluon events (red) in simulated data.

1475 Previous study in ATLAS has shown that the jets can be tagged quark or gluon
 1476 jets based on the number of charged tracks associated with the jets with p_T above 500
 1477 MeV. Samples with enhanced fractions of quark or gluon initiated jets can be created by
 1478 using a selection based on the charged-particle constituent multiplicity N_{trk} . As shown in
 1479 Figure 6.57, where PYTHIA 8 generator is used for MC to ensure a good agreement with
 1480 the distribution of N_{trk} in data within the ID acceptance $|\eta| < 2.1$.

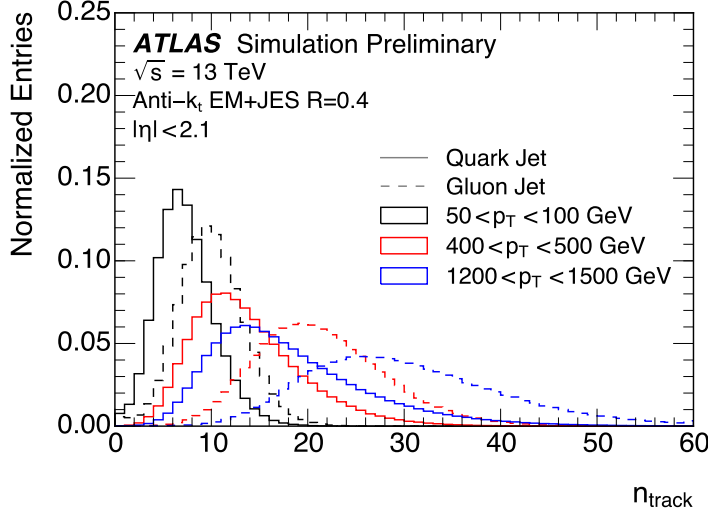


Figure 6.57 Distribution of the jet reconstructed track multiplicity (N_{trk}) in different p_{T} ranges with the PYTHIA 8 MC samples and processes with a full simulation of the ATLAS detector. Tracks are required to have $p_{\text{T}} > 500$ MeV and pass quality criteria described in Ref. [23].

1481 6.3.1 Expected Signal Significance

1482 The shape of m_{jj} from QCD is complex and rapidly changing according to the frac-
 1483 tions of events that originate from quark-quark, quark-gluon and gluon-gluon scattering.
 1484 The QCD background is presented in Section 6.1.1. The MC simulated signals and back-
 1485 ground is thus used for estimating the expected signal significance.

1486 6.3.1.1 Resonances that decay to quark-quark

1487 The statistical significance associated with signals decaying into quark-antiquark
 1488 pairs is assessed using Z' models using

$$S = N_S \sum_i \frac{f_{qq,i} \epsilon_{qQ}^2 + f_{qg,i} \epsilon_{qQ} \epsilon_{gQ} + f_{gg,i} \epsilon_{gQ}^2}{\sqrt{B_{qq,i} \epsilon_{qQ}^2 + B_{qg,i} \epsilon_{qQ} \epsilon_{gQ} + B_{gg,i} \epsilon_{gQ}^2}} \quad (6.2)$$

1489 where N_S is the number of signal events, $f_{qq,i}$ is fraction of signal events that result in the
 1490 two highest jets that were initiated by quarks in bin i ($f_{qg,i}$ are quark-gluon jets, and $f_{gg,i}$
 1491 is two gluon jets), ϵ_{qQ} is the efficiency of a quark initiated jet passing the quark selection
 1492 criteria, ϵ_{gQ} is the efficiency of a gluon initiated jet passing the quark selection criteria,
 1493 and $B_{xx,i}$ is the expected number of background events with quark-quark, quark-gluon or
 1494 gluon-gluon initiated jets.

1495 The statistical significance is computed for Z' particles mass values within the range
 1496 of 1500 to 4000 GeV, and for quark-jet selection efficiencies ranging from 30% to 90%.
 1497 The obtained significance values are presented in Figure 6.58. The depicted results il-
 1498 lustrate a trend of diminishing significance when any quark-selection criteria is imposed
 1499 on the data. This decline in significance can be attributed to the dominant presence of
 1500 quark-quark events within the data, where the selection process concurrently diminishes
 1501 both background and signal contributions to a comparable extent.

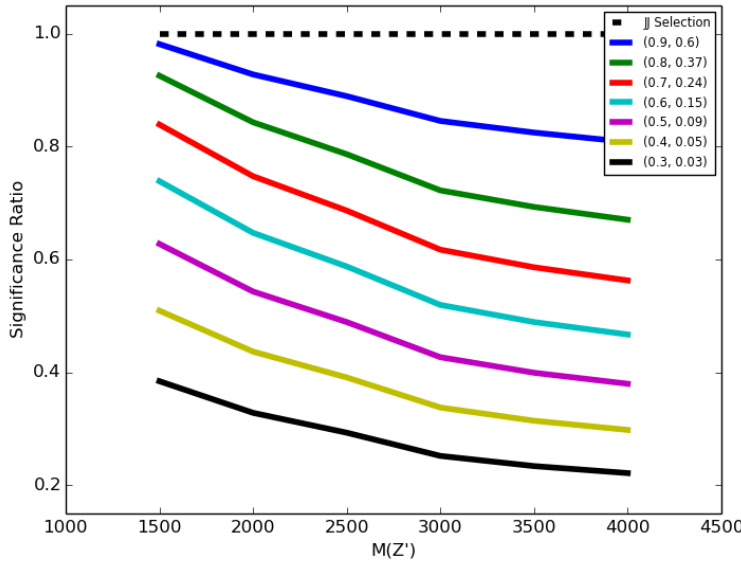


Figure 6.58 The significance for observing a Z' with masses from 1500 to 4000 GeV for ϵ_{qQ} ranging from 90 to 30% compared to the significance calculated with no quark selection applied. The key gives pairs of efficiencies $(\epsilon_{qQ}, \epsilon_{gQ})$.

1502 6.3.1.2 Signals that decay to gluon-gluon

1503 The significance for signals that decay to a gluon-gluon pair are using H' models,
 1504 estimated by:

$$S = N_S \sum_i \frac{f_{qq,i} \epsilon_{qG}^2 + f_{qg,i} \epsilon_{qG} \epsilon_{gG} + f_{gg,i} \epsilon_{gG}^2}{\sqrt{B_{qq,i} \epsilon_{qG}^2 + B_{qg,i} \epsilon_{qG} \epsilon_{gG} + B_{gg,i} \epsilon_{gG}^2}} \quad (6.3)$$

1505 where ϵ_{qG} is the efficiency of a quark initiated jet passing the gluon selection criteria, ϵ_{gG}
 1506 is the efficiency of a gluon initiated jet passing the gluon selection criteria.

1507 The computation of significance involves the utilization of simulated H' signals,
 1508 with masses ranging from 2000 to 7000 GeV. The efficiencies of gluon tagged are varied

1509 across from 60% to 90%. The resulting significances, depicted as functions of H' masses,
 1510 are presented in Figure 6.59. The observed trend reveals a gradual increase in signifi-
 1511 cance, with values ascending from approximately 1.2 at 2 TeV to around 1.6 at 7 TeV.
 1512 Notably, the most substantial enhancements occur at a gluon efficiency of 75%.

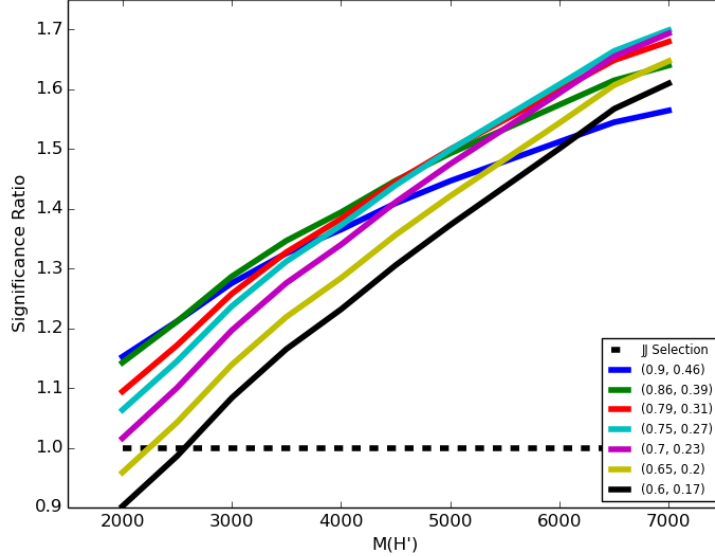


Figure 6.59 The significance for observing a H' with masses from 2000 to 7000 GeV for ϵ_{gG} ranging from 90 to 60% compared to the significance calculated with no gluon selection applied. The key gives pairs of efficiencies $(\epsilon_{gG}, \epsilon_{qG})$.

1513 6.3.1.3 Signals that decay to quark-gluon

1514 Calculating the significance for signals involving quark-gluon decays, such as string
 1515 decays, poses increased complexity due to the potential overlap in the selection criteria
 1516 between decaying jets that satisfy both quark and gluon criteria. In this context, it be-
 1517 comes imperative to establish distinct efficiencies exclusively tailored for quark- and
 1518 gluon-jets. Thus the efficiencies are needed to be defined exclusively for quark- and
 1519 gluon-jets.

1520 The efficiencies for quark-jets are defined as:

- 1521 • ϵ_{qQ} The efficiency that a quark-jet is identified only as a quark-jet.
- 1522 • ϵ_{qQG} The efficiency that a quark-jet is identified as a quark- and a gluon-jet.
- 1523 • ϵ_{qG} The efficiency that a quark-jet is identified only as a gluon-jet.

1524 where $\epsilon_{qQ} + \epsilon_{qQG} + \epsilon_{qG} = 1$.

1525 Another set of efficiencies that is measured for gluon-jets are:

1526 • ϵ_{gQ} The efficiency that a gluon-jet is identified only as a quark-jet.

1527 • ϵ_{gQG} The efficiency that a gluon-jet is identified as a quark- and a gluon-jet.

1528 • ϵ_{gG} The efficiency that a gluon-jet is identified only as a gluon-jet.

The probability of truth pairs of quark-quark (p_{qq}), quark-gluon (p_{qg}) and gluon-gluon (p_{gg}) events that passing the quark-gluon tagging selection criteria are given by:

$$p_{qq} = 2\epsilon_{qQ}\epsilon_{qG} + \epsilon_{qQG}(\epsilon_{qQ} + \epsilon_{qG}) + \epsilon_{qQG}\epsilon_{qQG} \quad (6.4)$$

$$p_{gg} = 2\epsilon_{gQ}\epsilon_{gG} + \epsilon_{gQG}(\epsilon_{gQ} + \epsilon_{gG}) + \epsilon_{gQG}\epsilon_{gQG} \quad (6.5)$$

$$p_{qg} = \epsilon_{qQ}\epsilon_{gG} + \epsilon_{gQ}\epsilon_{qG} + \epsilon_{qQG}(\epsilon_{gQ} + \epsilon_{gG}) + \epsilon_{gQG}(\epsilon_{qQ} + \epsilon_{qG}) + \epsilon_{gQG}\epsilon_{gQG} \quad (6.6)$$

1529 the related significance is then defined as:

$$S = N_S \sum_i \frac{f_{qq,i}p_{qq} + f_{qg,i}p_{qg} + f_{gg,i}p_{gg}}{\sqrt{B_{qq,i}p_{qq} + B_{qg,i}p_{qg} + B_{gg,i}p_{gg}}}. \quad (6.7)$$

1530 No obvious benefit is observed after applied a quark selection with selection ef-
 1531 ficiencies from 30 to 100%. A small but significant improvement is obtained in sig-
 1532 nificance by applying a gluon selection to one of the two leading jets. The resulting
 1533 significances are in Fig. 6.60 where an increase of 25% in significance at masses above
 1534 5 TeV is obtained, with the largest increases happening over 70% gluon efficiency.

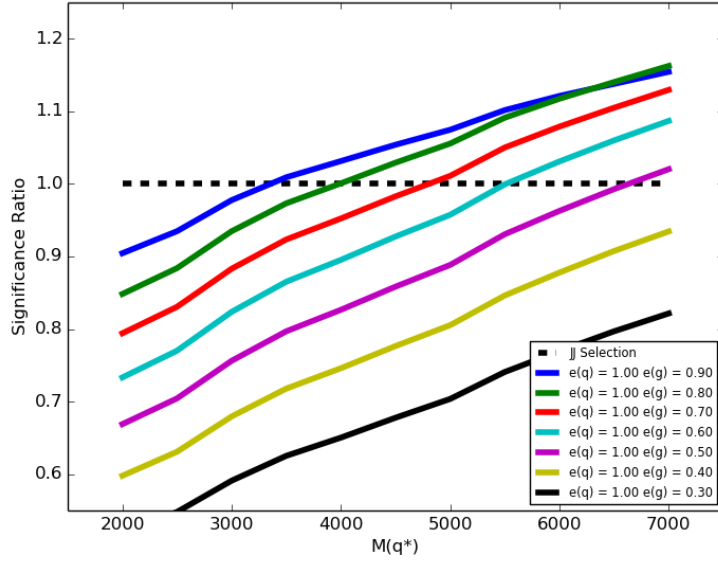


Figure 6.60 The significance for observing a q^* with masses from 2000 to 7000 GeV for ϵ_{gG} ranging from 30 to 90% compared to the significance calculated with no gluon selection applied. The key gives pairs of efficiencies (ϵ_{gG} , ϵ_{qG}).

1535 6.3.2 Selection Criteria

1536 The selection criteria for an quark-enriched jet sample was chosen so that 60%
 1537 quark-initiated purity is achieved in each jet p_T bin. However, discontinuities in the m_{jj}
 1538 spectrum would occur when such criteria is applied to the high mass ($p_T > 5000$ GeV),
 1539 leads to difficulties presented in resonance search.

A selection criteria is thus built as a linear function of the $\ln(p_T)$, results in a smooth m_{jj} distribution. A jet is tagged as being more likely to be quark-initiated if N_{trk} is less than the threshold n_q and more likely to be gluon-initiated if N_{trk} is greater than the threshold n_g :

$$N_{\text{trk}} \leq n_q \text{ quark-initiated sample} \quad (6.8)$$

$$N_{\text{trk}} \geq n_g \text{ gluon-initiated sample}$$

1540 where

$$n_{q(g)} = c_{q(g)} + m_{q(g)} \ln(p_T) \quad (6.9)$$

1541 parameters $m_{q(g)}$ and $c_{q(g)}$ are constants obtained from the MC samples, these are founded

1542 by finding the value of N_{trk} that corresponds to a given efficiency for truth quark and gluon
 1543 jets in p_T bins, and chosen to defined suitable subsamples, the p_T here is in units of GeV.

1544 For each p_T bin, the number of tracks N_{trk} that closest to the given selection effi-
 1545 ciency is found. Because the N_{trk} is an integer number of track thus does not correspond
 1546 exactly to the selection efficiency, a linear interpolation is carried out between the given
 1547 efficiencies of the selected bin and the closest bin of it, to correct the fractional number
 1548 of tracks that corresponds to the selection efficiency, the corresponding uncertainty is
 1549 evaluated as binomial distribution.

1550 The jet p_T bin edges are divided into 480, 500, 520, 540, 560, 580, 600, 625, 650,
 1551 700, 750, 800, 900, 1000, 1400, 1600, 1800, 2000, 2500, 3000, 3500, 4000, 5000, 6000
 1552 GeV. An example of the cumulative distribution of N_{trk} for truth quark- and gluon-jets at
 1553 the p_T range of 800 - 900 GeV is shown in Figure 6.61.

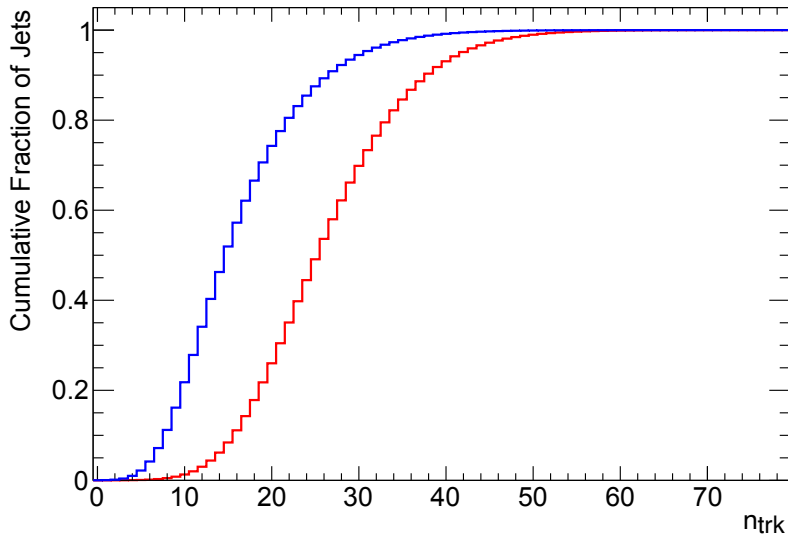


Figure 6.61 The cumulative distribution of N_{trk} for truth quark- (blue) and gluon- (red) jets satisfying $800 < p_T < 900$ GeV.

1554 The coefficients for Equation 6.9 are determined for quark and gluon selection ef-
 1555 ficiencies ranging from 65% to 95% in increments of 5%. The plot showcasing the N_{trk}
 1556 values corresponding to selection efficiencies of 70%, 75%, and 80% is depicted in Fig-
 1557 ure 6.62, along with the optimal fit employing Equation 6.9. The constants' values for
 1558 both quark and gluon selections are summarized in Tables 6.25 and 6.26. For a selec-
 1559 tion efficiency of 75%, the fitting yields a χ^2 of 33.5 (quark selection) and 2.6 (gluon
 1560 selection) for 21 degrees of freedom.

Notably, the N_{trk} value that satisfies the selection efficiency attains a plateau above 4000 GeV, suggesting the potential presence of a saturation effect. To validate these findings, the data is subjected to an alternative fit function. An alternative fit function is derived as a cross check:

$$n_{q(g)} = c + m \ln(p_T) + n \sqrt{\ln(p_T)}. \quad (6.10)$$

which improve the χ^2 of the fit in a selection efficiency of 75% from 33.5 to 25.1 in quark-selection, and from 2.6 to 1.6 in gluon-selection. Figure 6.63 shows the alternative fit for quark and gluon selections. The values of the constants for both quark and gluon selections are summarised in Tables 6.27 and 6.28.

The values of the constants for both quark and gluon selections are summarised in Tables 6.25 and 6.26.

Truth- q selection efficiency	Truth- g selection efficiency	c	m
0.95	0.732	-27.568	8.789
0.90	0.563	-21.518	7.269
0.85	0.447	-17.646	6.304
0.80	0.350	-14.956	5.610
0.75	0.278	-12.600	5.022
0.70	0.221	-10.691	4.536
0.65	0.174	-8.990	4.105

Table 6.25 Values of constants m and c from Equation. 6.9 such that $N_{\text{trk}} \leq n_q$ for truth quark jets for a range of efficiencies from 65 to 95%.

1570

Truth- g selection efficiency	Truth- q selection efficiency	c	m
0.95	0.586	-7.541	3.233
0.90	0.456	-8.980	3.779
0.85	0.377	-10.419	4.230
0.80	0.320	-11.964	4.659
0.75	0.274	-13.376	5.047
0.70	0.234	-14.937	5.446
0.65	0.202	-16.466	5.834

Table 6.26 Values of constants m and c from Equation 6.9 such that $N_{\text{trk}} \geq n_g$ for truth quark jets for a range of efficiencies from 65 to 95%.

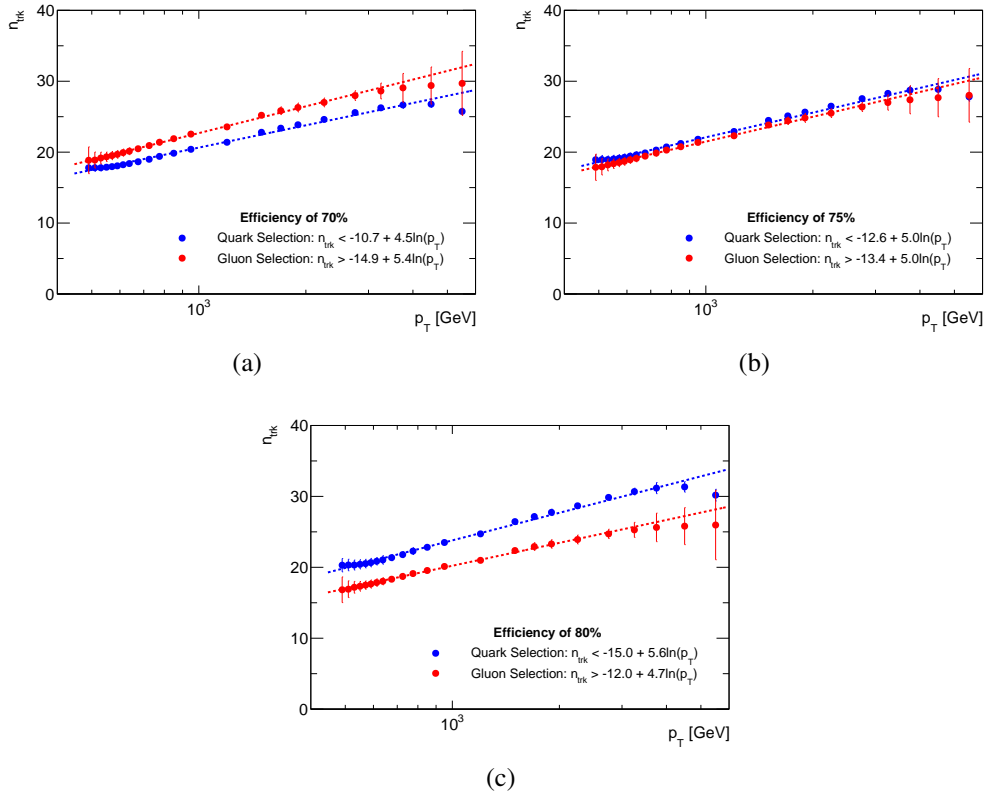


Figure 6.62 The values of N_{trk} for (a) 70%, (b) 75% and (c) 80% quark (blue) and gluon (red) selection efficiencies in each p_T bin along with the best fit to Equation 6.9.

Search for new phenomena in dijet events

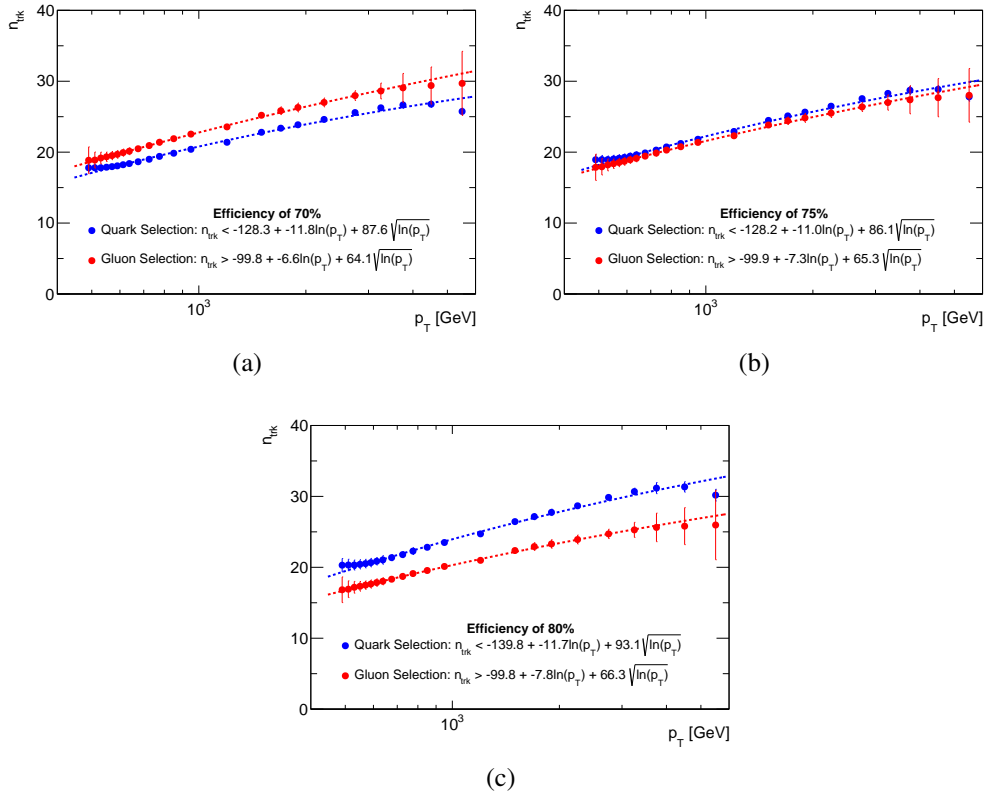


Figure 6.63 The values of N_{trk} for (a) 70%, (b) 75% and (c) 80% quark (blue) and gluon (red) selection efficiencies in each p_T bin along with the best fit to Equation 6.10.

Search for new phenomena in dijet events

Truth- q selection efficiency	Truth- g selection efficiency	c	m	n
0.80	0.350	-139.822	-11.714	93.100
0.75	0.278	-128.174	-11.001	86.141
0.70	0.221	-128.255	-11.755	87.604

Table 6.27 Values of constants m and c from Equation 6.10 such that $N_{\text{trk}} \leq n_q$ for truth quark jets for a range of efficiencies from 70 to 80%.

Truth- g selection efficiency	Truth- q selection efficiency	c	m	n
0.80	0.320	-99.796	-7.839	66.301
0.75	0.274	-99.949	-7.271	65.347
0.70	0.234	-99.774	-6.640	64.077

Table 6.28 Values of constants m and c from Equation 6.10 such that $N_{\text{trk}} \geq n_g$ for truth quark jets for a range of efficiencies from 70 to 80%.

6.3.2.1 Signal Selection Efficiencies

The H' signal described in section 6.1.2 is required to pass the selection criteria for a single jet gluon selection efficiency of 75% given in Table 6.29. The selection efficiency for the H' sample is expected to be 56.3% (0.75^2 as both jets are required to be 75%). In actual process, the ratio of H' events that decay to two gluons ranges from 51.9% for a 2 TeV signal to 57.4% for a 7 TeV signal.

The effective fraction of H' events decaying into two gluons is slightly below 100%, due to factors like gluon splitting and other showering effects. This fraction varies from 91.3% to 95.4%. The discrepancy between the actual efficiency and the expected efficiency (56.3% of the truth efficiency) is depicted in Figure 6.64. The average difference across selection criteria is approximately 3.3%.

Since there is minimal distinction between the two selection criteria, the simpler choice outlined in Equation 6.9 will be adopted.

H' Mass (GeV)	Selection efficiency(%)		
	Equation 6.9	Equation. 6.10 ($\sqrt{}$ term)	Truth
2000	51.9	51.8	91.3
2500	53.2	53.0	91.7
3000	54.9	54.6	92.3
3500	55.3	55.1	93.4
4000	56.4	56.2	93.4
4500	56.7	56.7	94.1
5000	56.2	56.4	94.3
5500	57.2	57.5	94.9
6000	57.4	57.8	95.1
6500	57.4	58.3	95.5
7000	57.4	58.1	95.4

Table 6.29 The signal selection efficiency for a fully simulated H' decaying to two gluons with requiring two jets to pass the 75% single jet criteria given in Equation 6.9 with constants from Table 6.26 and the criteria given in Equation 6.10 with constants from Table 6.28. The expected double tagged gluon efficiency is 56.3%.

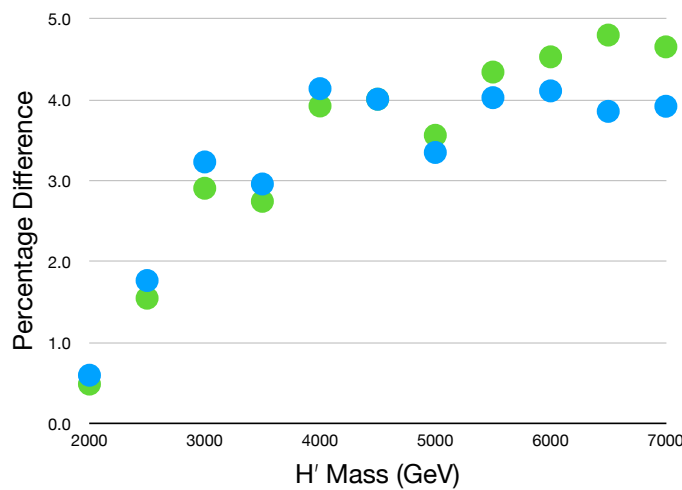


Figure 6.64 The difference between the expected signal selection efficiency of 56.3% for a single jet selection efficiency of 75% for H' using Equation 6.9 (Blue) and Equation 6.10 (Green)

1584 6.4 Signal Optimisation

1585 6.4.1 y^* Cut Optimisation

1586 In QCD, t -channel in 2-to-2 scattering is the dominant process. Thus the dijet pro-
 1587 duction from the QCD is proportional to $(1 - \cos \theta^*)^{-2}$. However the distribution of
 1588 $\cos \theta^*$ is supposed to be flat for H' signal, which means the y^* of H' signal will peak at 0
 1589 while that of QCD background will minimize at 0.

1590 The significance is defined as:

$$1591 S = \sqrt{\sum_i 2 \left[(S_i + B_i) \cdot \ln \left(1 + \frac{S_i}{B_i} \right) - S_i \right]} \quad (6.11)$$

1591 where S_i (B_i) is the number of signal (background) events in bin i . The calculation of
 1592 such significance only include the bins where signal samples have 95% of the area under
 1593 the distribution, not include the entire m_{jj} distribution.

1594 For some signal samples where S_i is small ($S_i \ll 10^{-5}$) thus the logarithm func-
 1595 tions do not have enough precision in equation 6.11. An approximation is introduced as
 1596 follows:

$$1597 S = \sqrt{\sum_i 2 \sum_{n=1}^6 \frac{(-S_i)^{n+1}}{n(n+1)B_i^n}} \quad (6.12)$$

1597 which is accurate up to 10 decimal places around $\frac{S_i}{B_i} = 10^{-5}$ and even more precise for
 1598 smaller $\frac{S_i}{B_i}$.

1599 The significance of H' signal as a function of the value of the y^* is shown in Fig-
 1600 ure 6.65. The peaks of significance in all tagging categories are around 0.6, therefore
 1601 an optimal y^* cut for the H' search is set to $|y^*| < 0.6$. The exact values of y^* cut that
 1602 correspond to the peak significance value for the H' signal at each mass point are shown
 1603 in Table 6.30 with the ranges in y^* cut around the peak that gives a significance ≥ 0.99 .

1604 For String signal, there is also a dependence on $\cos \theta^*$, leads the y^* will peak at 0
 1605 too. Figure 6.66 shows the significance of String signal as a function of y^* cut. The
 1606 maximum significance in all tagging categories are around 0.8, therefore an optimal y^*
 1607 cut for the String search is set to $|y^*| < 0.8$. The exact values of y^* cut that correspond
 1608 to the peak significance value for the String signal at each mass point are shown in
 1609 Table 6.31 with the ranges in y^* cut around the peak that gives a significance ≥ 0.99 .

1610 Figure 6.67 shows the significance of Graviton signal as a function of y^* cut. The

Search for new phenomena in dijet events

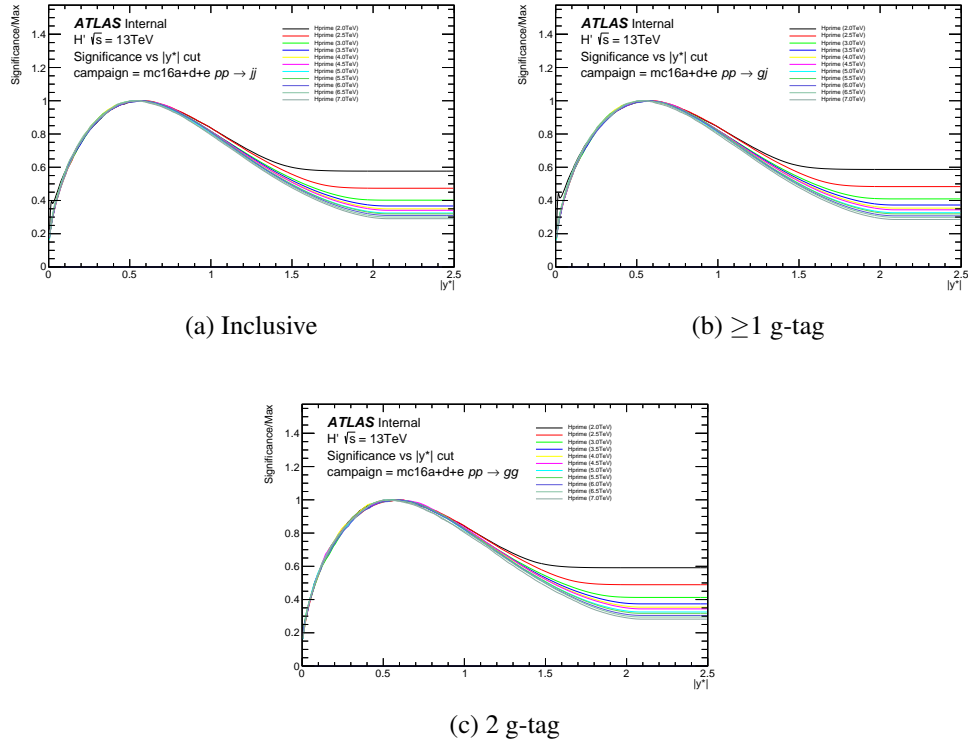


Figure 6.65 H' significance as a function y^* cut in the case of (a) Inclusive, (b) ≥ 1 g-tag, (c) 2 g-tag.

H' Mass (TeV)	Optimal Selection			Peak Width
	Inclusive	≥ 1 g tag	≥ 2 g tag	
2.0	0.57	0.57	0.57	0.50–0.65
2.5	0.58	0.59	0.62	0.50–0.67
3.0	0.59	0.59	0.59	0.50–0.66
3.5	0.56	0.56	0.60	0.49–0.65
4.0	0.58	0.58	0.58	0.47–0.65
4.5	0.55	0.57	0.57	0.35–0.68
5.0	0.55	0.56	0.57	0.47–0.66
5.5	0.55	0.55	0.57	0.46–0.66
6.0	0.60	0.60	0.60	0.52–0.66
6.5	0.55	0.55	0.54	0.47–0.64
7.0	0.56	0.56	0.51	0.35–0.61

Table 6.30 $|y^*|$ selection leading to the maximum significance value calculated using Equation 6.11.

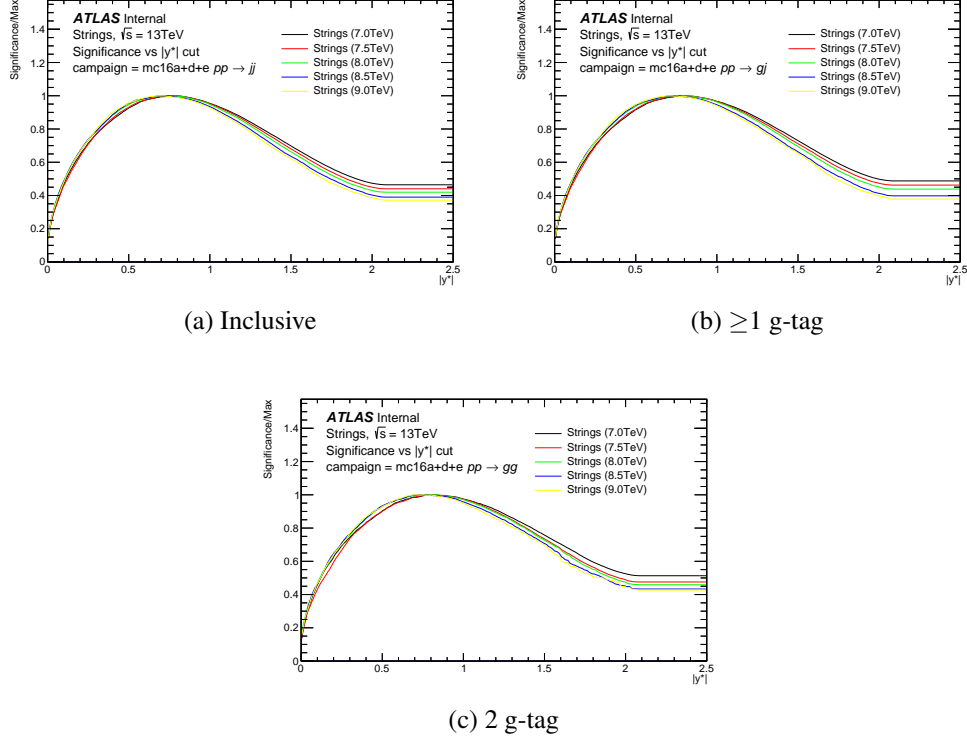


Figure 6.66 String significance as a function y^* cut in the case of (a) Inclusive, (b) ≥ 1 g-tag, (c) 2 g-tag.

String Mass (TeV)	Optimal Selection			Peak Width
	Inclusive	≥ 1 g tag	2 g tag	
7.0	0.78	0.82	0.81	0.70–0.91
7.5	0.77	0.77	0.83	0.68–0.91
8.0	0.72	0.76	0.84	0.66–0.90
8.5	0.74	0.74	0.74	0.65–0.85
9.0	0.71	0.71	0.71	0.62–0.84

Table 6.31 $|y^*|$ selection leading to the maximum significance value calculated using Equation 6.11.

significance peaks at about 0.6, so the optimal cut for the Graviton search is $|y^*| < 0.6$. Table 6.32 shows the y^* cut corresponding to the peak significance value for Graviton at each mass point, and the range in y^* cut around the peak that gives a significance ≥ 0.99 . Figure 6.68 shows the significance of QBH signal as a function of y^* cut. The maximum significance is at about 0.9, so the optimal cut for the QBH search is $|y^*| < 0.9$.

Search for new phenomena in dijet events

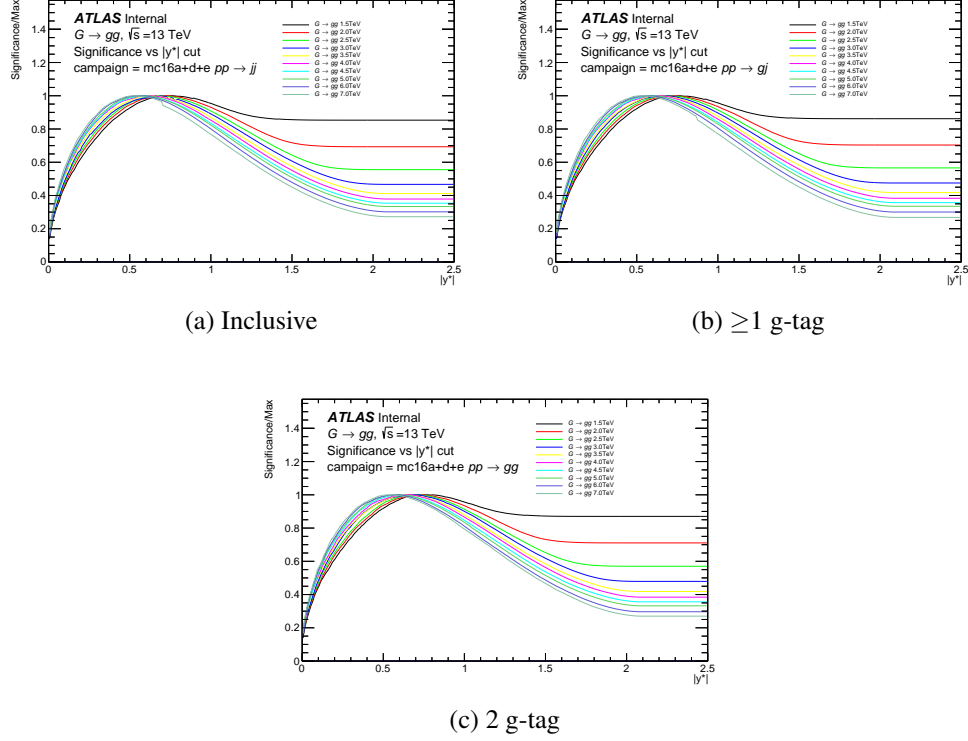


Figure 6.67 Graviton significance as a function y^* cut in the case of (a) Inclusive, (b) ≥ 1 g-tag, (c) 2 g-tag.

Graviton Mass (TeV)	Optimal Selection			Peak Width
	Inclusive	≥ 1 g tag	2 g tag	
1.5	0.77	0.77	0.78	0.65–0.87
2.0	0.71	0.74	0.72	0.65–0.83
2.5	0.67	0.69	0.70	0.61–0.80
3.0	0.66	0.66	0.66	0.60–0.77
3.5	0.64	0.65	0.65	0.57–0.73
4.0	0.63	0.64	0.64	0.55–0.73
4.5	0.59	0.59	0.59	0.53–0.69
5.0	0.59	0.59	0.59	0.50–0.69
6.0	0.57	0.57	0.60	0.49–0.66
7.0	0.53	0.53	0.56	0.47–0.63

Table 6.32 $|y^*|$ selection leading to the maximum significance value calculated using Equation 6.11.

Search for new phenomena in dijet events

Table 6.33 shows the y^* cut corresponding to the peak significance value for the QBH at each mass point, and the range in y^* cut around the peak that gives a significance ≥ 0.99

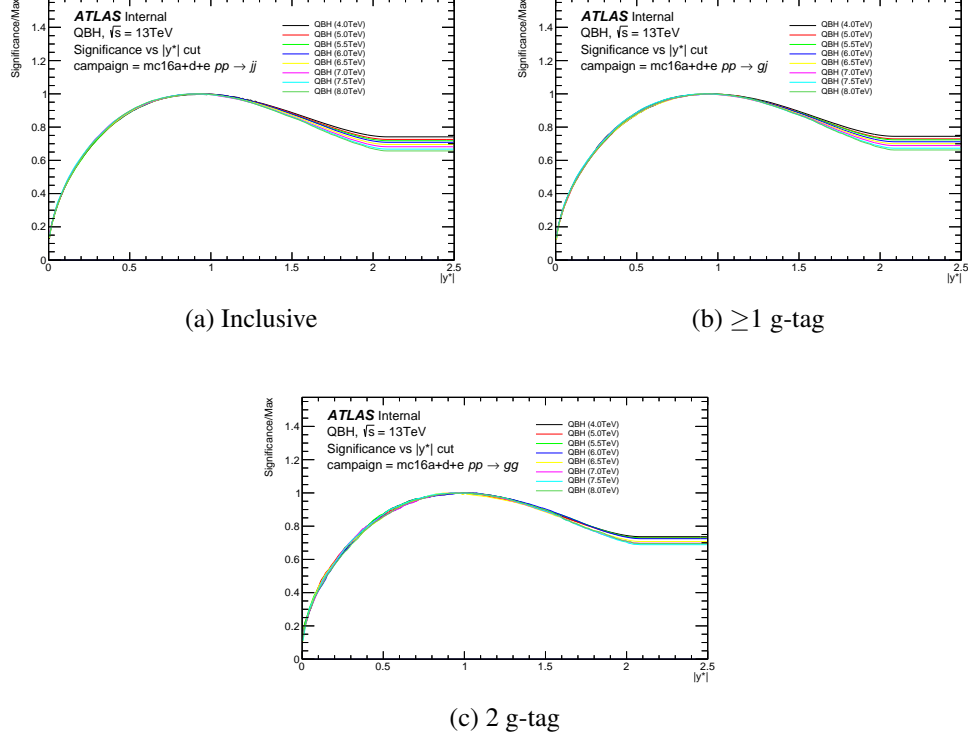


Figure 6.68 QBH significance as a function y^* cut in the case of (a) Inclusive, (b) ≥ 1 g-tag, (c) 2 g-tag.

1617

QBH Mass (TeV)	Optimal Selection			Peak Width
	Inclusive	≥ 1 g tag	2 g tag	
4.0	0.92	0.95	1.01	0.81–1.11
5.0	0.95	0.95	0.95	0.81–1.09
5.5	0.94	0.96	0.94	0.81–1.09
6.0	0.92	0.96	1.01	0.81–1.09
6.5	0.91	0.91	0.93	0.81–1.06
7.0	0.93	0.97	0.94	0.82–1.07
7.5	0.92	0.94	0.93	0.79–1.08
8.0	0.92	0.96	0.99	0.82–1.09

Table 6.33 $|y^*|$ selection leading to the maximum significance value calculated using Equation 6.11.

6.4.2 Dijet Mass Turn-on

The m_{jj} turn-on is investigated by comparing events collected with the highest p_T trigger threshold with one with a lower p_T threshold using data. The efficiency of the HLT_j420 trigger is calculated by comparing to the following triggers in each data taking period: 2015 HLT_j360, 2016 HLT_j380, 2017 and 2018 HLT_mu50. The muon trigger 2017 and 2018 are included as HLT_j420 is the only unprescaled jet trigger available. The full Run 2 dataset is included for comparison as the HLT_mu50 is available for all running periods. Events where the efficiency of trigger less than 99.5% will be removed by a mass cut.

The efficiencies as a function of m_{jj} are shown in Figure. 6.69 for $|y^*| < 0.6$ and Figure. 6.70 for $|y^*| < 0.8$ in two gluon-tag categories for both triggers. The results are summarised in Table. 6.34 for the different data-taking periods. The m_{jj} mass cut is chosen to be slightly above the value of the plateau ($\geq 99.5\%$), so a cut of 1100 GeV for $|y^*| < 0.6$ is applied. For $|y^*| < 0.8$, a cut of 1200 is applied to samples with either one or two gluon tags.

Data Taking Period	Mass turn on $ y^* < 0.6$		Mass turn on $ y^* < 0.8$	
	≥ 1 g-tag (GeV)	≥ 2 g-tag (GeV)	≥ 1 g-tag (GeV)	≥ 2 g-tag (GeV)
2015	1040	1030	1160	1160
2016	1030	1030	1160	1170
2017	990	1000	1110	1120
2018	1000	1010	1110	1120
Run 2	1020	1030	1120	1120

Table 6.34 The m_{jj} value of the start of the plateau ($\geq 99.5\%$) for each period of data taking.

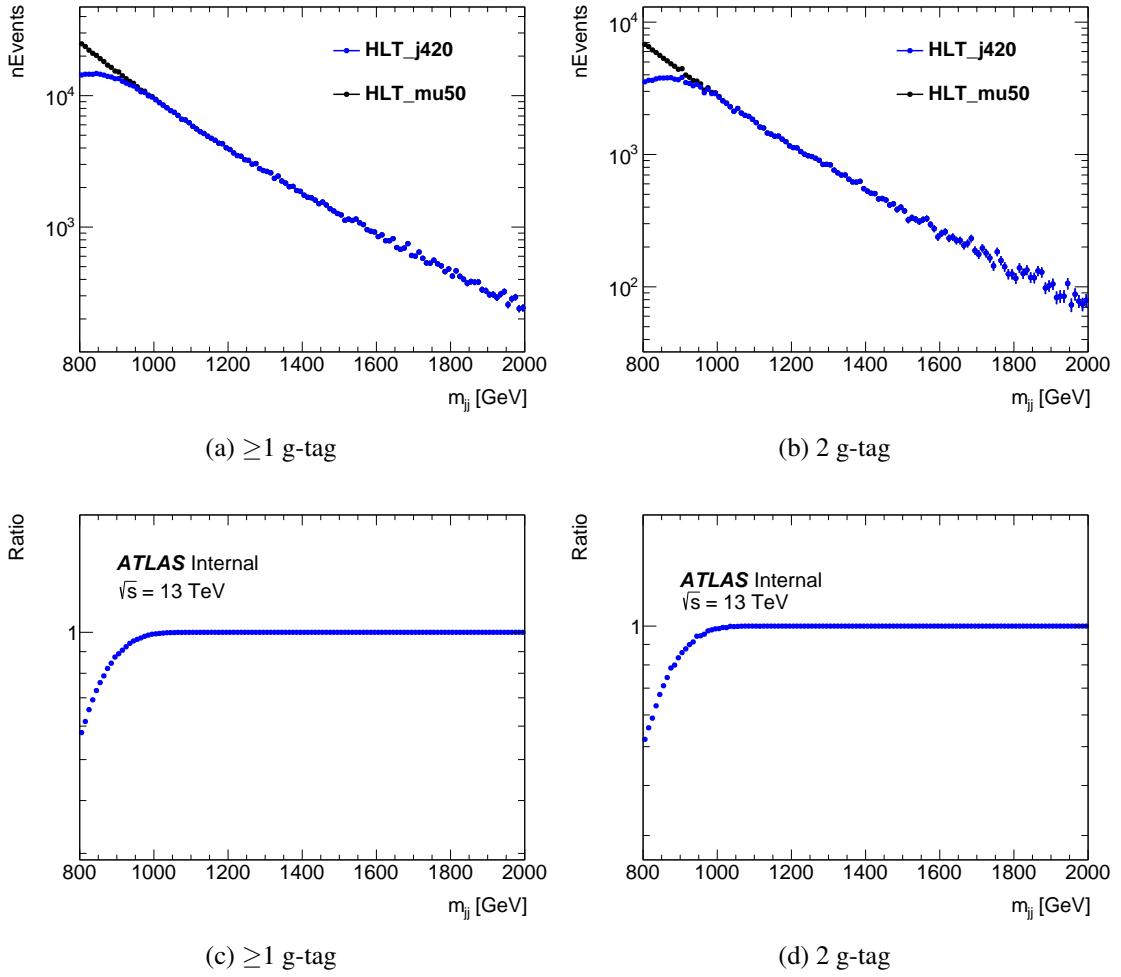


Figure 6.69 Eiciencies as a function of m_{jj} for $|y^*| < 0.6$ using HLT_j420 compared with HLT_mu50 in the case of comparison of mass spectra with (a) ≥ 1 g-tag, (b) 2 g-tag and the ratio between the two (c) ≥ 1 g-tag and (d) 2 g-tag.

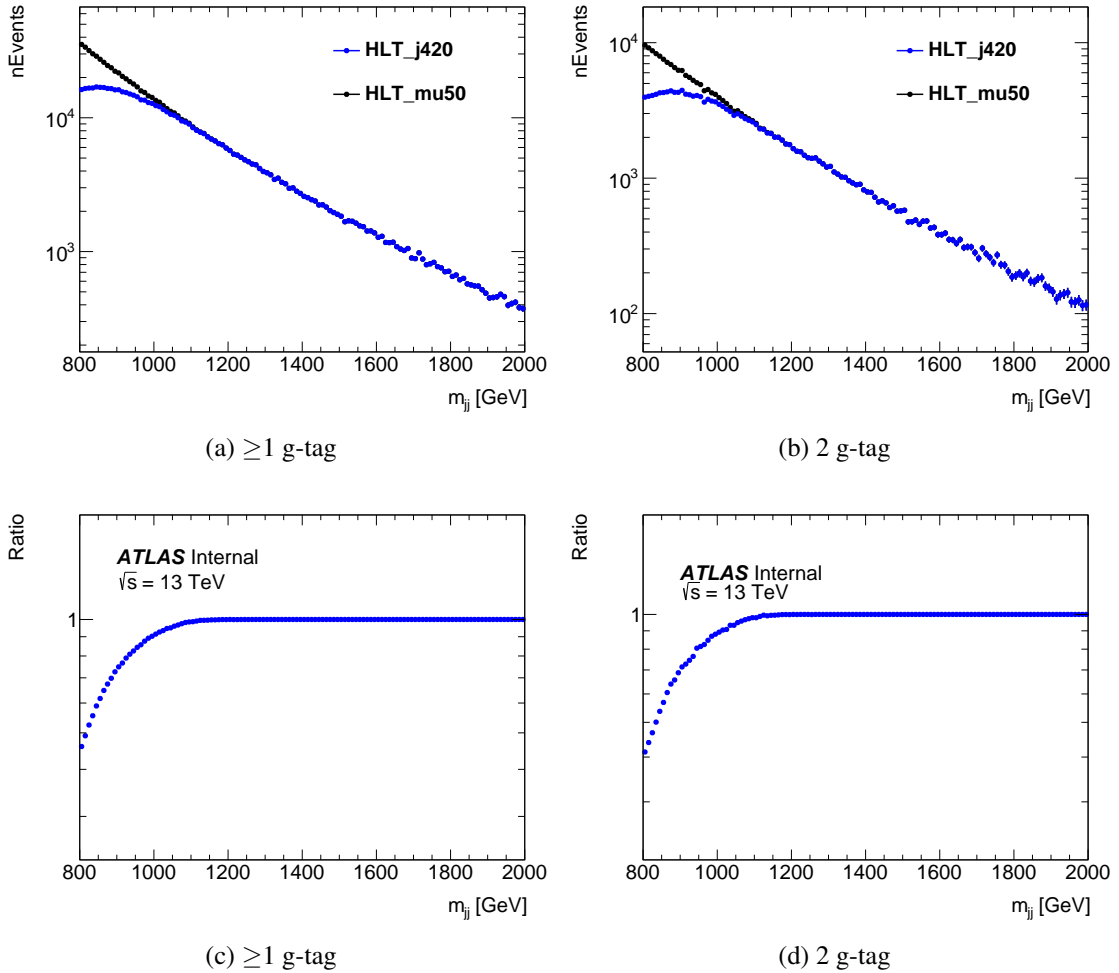


Figure 6.70 Eiciencies as a function of m_{jj} for $|y^*| < 0.8$ using HLT_j420 compared with HLT_mu50 in the case of comparison of mass spectra with (a) ≥ 1 g-tag, (b) 2 g-tag and the ratio between the two (c) ≥ 1 g-tag and (d) 2 g-tag.

1633 **6.4.3 Optimised Selection**

1634 In addition to the baseline selection described in Section 6.2.2, optimized cuts are
1635 applied to different tagging regions to improve the search potential with good tracking
1636 efficiency.

1637 The following additional cuts are applied for the the inclusive samples.

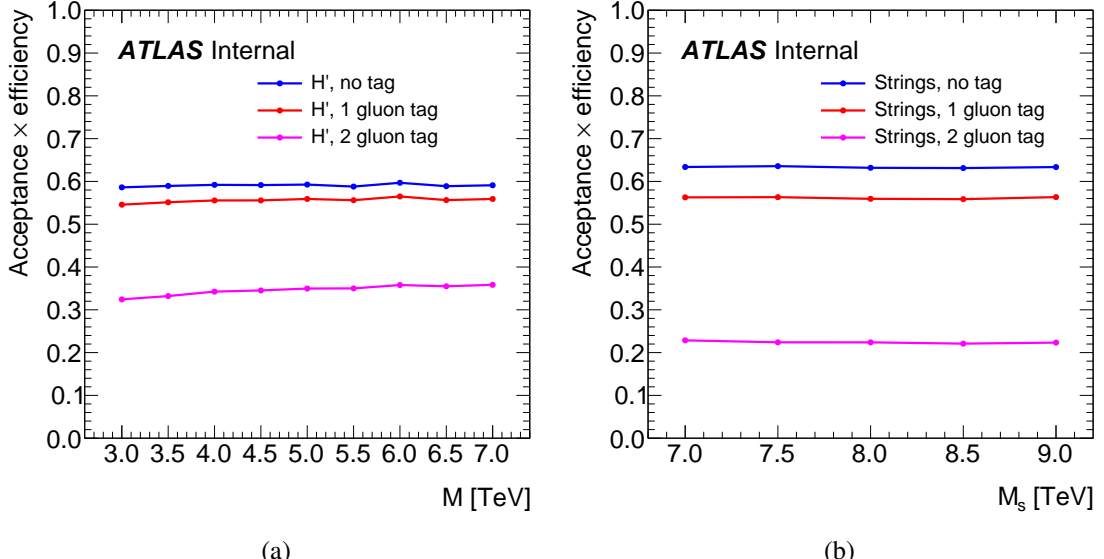
- 1638 • $|y^*| < 0.8$
- 1639 • $m_{jj} > 1200 \text{ GeV}$

1640 The following additional cuts are for quark-gluon tagging.

- 1641 • $|\eta| < 2.1$ (both jets) for track acceptance
- 1642 • ≥ 1 gluon tagged (75% working point)
- 1643 • 2 gluons tagged (75% working point)

1644 where the 75% gluon selection criteria is applied as: $N_{\text{trk}} > -7.3 + 4.2 \ln(p_T)$, with jet
1645 p_T in GeV.

1646 The acceptance times efficiency as a function of signal masses in inclusive, signal-
1647 gluon and double-gluon tagged regions for different benchmark signal models are shown
1648 in Figure 6.71.


 Figure 6.71 Acceptance times efficiency for the (a) H' signal and (b) String signal.

1649 6.4.4 Selected Kinematic Plots

1650 In this section a selection of kinematic and monitoring plots processed with sam-
 1651 ples passed the gluon-gluon selection criteria are shown in Figure 6.72, 6.73, 6.74. The
 1652 distributions of kinematics in MC are consistent with full dataset.

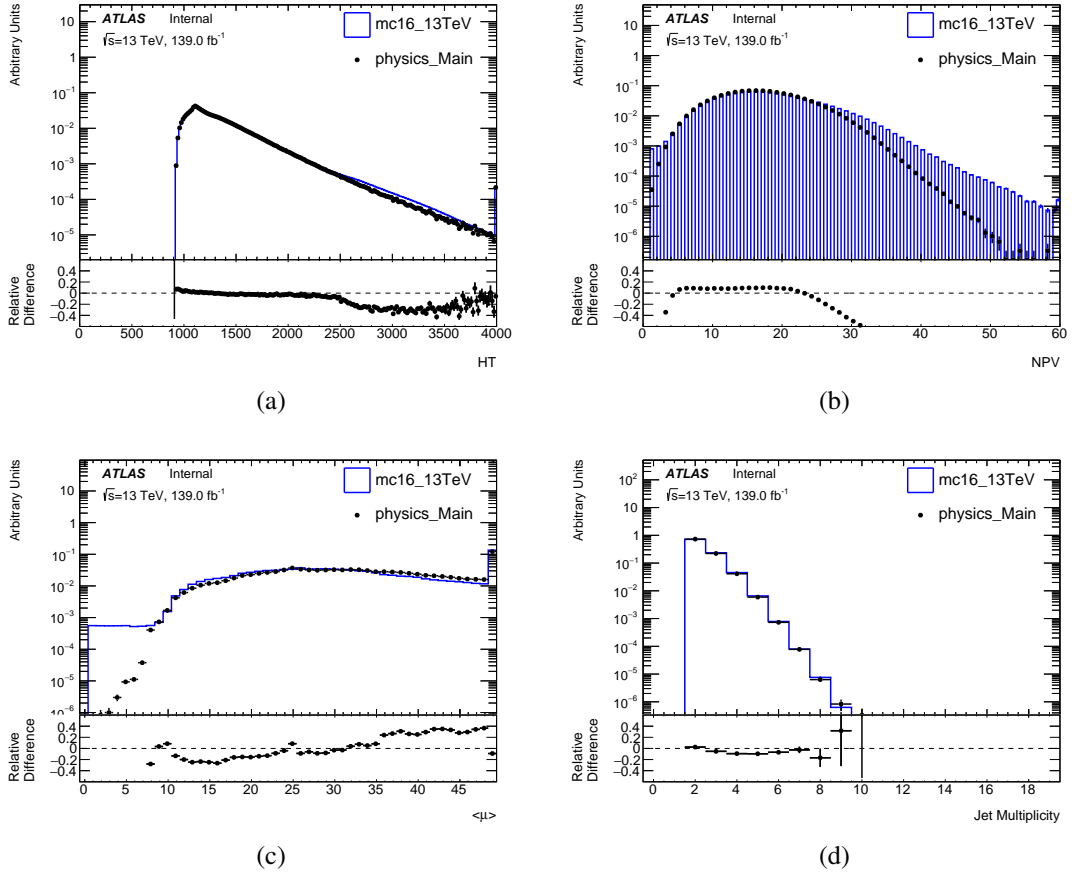


Figure 6.72 Monitoring plots for the gluon-gluon selection. (a) scalar p_T sum of all parton-level jets (H_T), (b) number of primary interaction vertices (NPV), (c) average interactions per bunch crossing, and (d) number of jets.

Search for new phenomena in dijet events

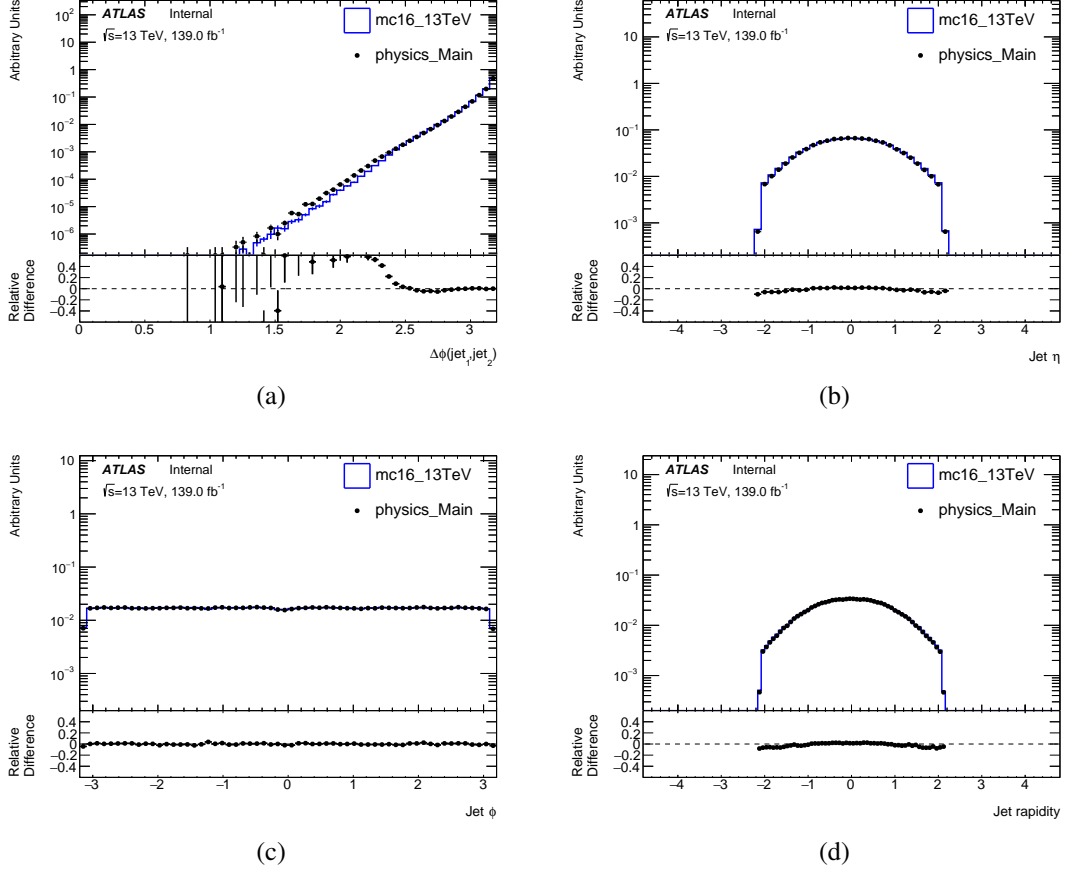


Figure 6.73 Monitoring plots on the gluon-gluon sample. (a) $\Delta\phi$ between the two jets, (b) jet η , (c) jet ϕ , and (d) jet rapidity.

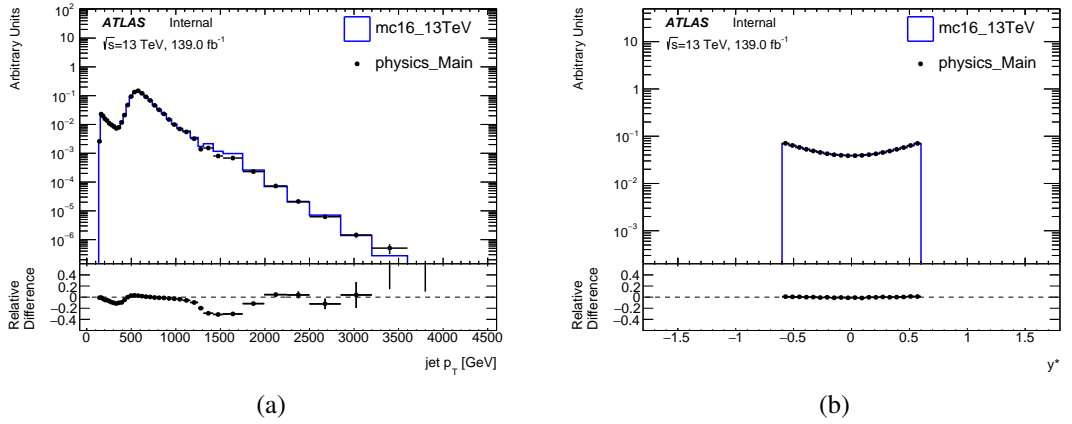


Figure 6.74 Monitoring plots on the gluon-gluon sample. (a) jet p_T , (b) y^* .

1653 6.5 Statistical Framework

1654 6.5.1 Fitting Framework

1655 The fitting framework used to parameterise QCD background is based on XML
 1656 Analytic Workspace Builder [85] (xmlAnaWSBuilder), which employs one-dimensional
 1657 observables to create RooFit [82] workspaces. The workflow of the framework is sum-
 1658 marised in Figure 6.75.

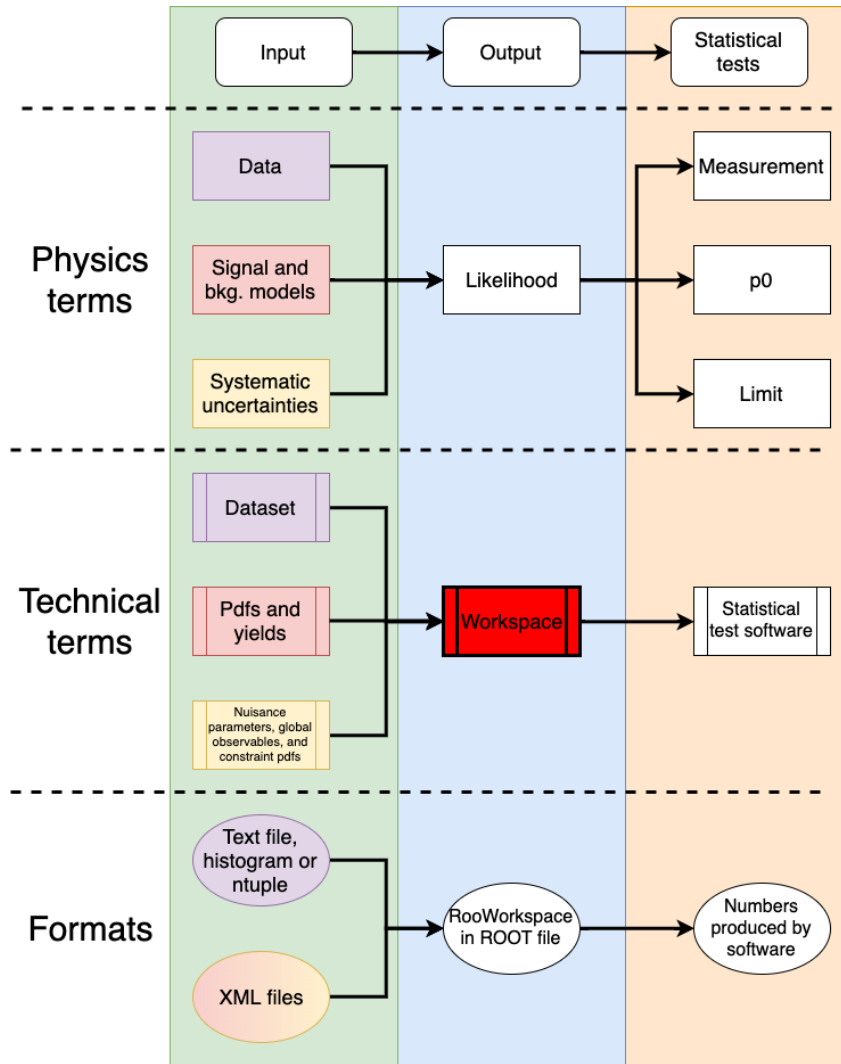


Figure 6.75 Workflow of the XmlAnaWSBuilder.

1659 The quickFit framework [84] that based on RooFit data fitting package is used for
 1660 data fitting. Modifications are needed so that it can integrate over binned data, as RooFit
 1661 evaluates its fit functions using the centre value of each bin rather than the actual average

mass in each bin. As a result, significant biases could occur in the fit results [59]. Recent developments introduce a new class of `RooBinSamplingPdf` in to `RooFit` package, which solve such issue.

6.5.2 Statistical Method

In this analysis, the discriminating variable is set to the dijet invariant mass m_{jj} , and the distribution of it is used as a probability density function (pdf) to build the likelihood function.

6.5.2.1 Parametric background models

The distribution of m_{jj} of background is parameterized by

$$f_b(m_{jj}; \mathbf{p}_b) = f_b(m_{jj}; p_1, p_2, p_3, p_4, p_5) = p_1 \left(1 - \frac{m_{jj}}{\sqrt{s}}\right)^{p_2} \left(\frac{m_{jj}}{\sqrt{s}}\right)^{p_3 + p_4 \ln\left(\frac{m_{jj}}{\sqrt{s}}\right) + p_5 \left[\ln\left(\frac{m_{jj}}{\sqrt{s}}\right)\right]^2}, \quad (6.13)$$

where \mathbf{p}_b are free parameters determined by fitting to data (or pseudo data), and $\sqrt{s} = 13$ TeV. In some cases, $p_5 = 0$ is taken. We will assume Equation (6.13) is normalized to unity as needed.

Given that we are employing a binned likelihood approach and working with histograms, it becomes essential to determine the average count of events in the i th bin, arising from both the signal and background contributions:

$$s_i = s_{\text{tot}} \int_{\text{bin } i} f_s(m_{jj}; \mathbf{p}_s) dm_{jj}, \quad (6.14)$$

$$b_i = b_{\text{tot}} \int_{\text{bin } i} f_b(m_{jj}; \mathbf{p}_b) dm_{jj}, \quad (6.15)$$

where f_s and f_b are pdfs of m_{jj} for the signal and background, respectively. The quantities s_{tot} and b_{tot} represent the total mean numbers of signal and background events. The variable b_{tot} is an additional nuisance parameter. The signal normalization s_{tot} is not treated as a parameter that can be adjusted, but rather is set to the value determined by the nominal signal model. The parameter can be expressed as $s_{\text{tot}} = \sigma L \epsilon$, where σ is fixed by the model cross section, and L and ϵ represent the nominal luminosity and total acceptance times efficiency, respectively.

6.5.2.2 Uncertainties

In this analysis, there are six sources of systematic uncertainties on the signal studied:

δL an uncertainty on the integrated luminosity of the data sample,

$\delta \epsilon$ an uncertainty on the signal efficiency times acceptance,

δt an uncertainty on the gluon-tag efficiency,

δE_{JER} an uncertainty on the jet energy resolution, and

δE_{JES} an uncertainty on the jet energy scale.

δS an uncertainty due to spurious signals.

All these uncertainties are treated as shape uncertainties except for δL which is a normalization uncertainty. These uncertainties are associated to nuisance parameters denoted by $\alpha_L, \alpha_\epsilon, \alpha_t, \alpha_{E_{\text{JER}}}, \alpha_{E_{\text{JES}}}, \alpha_S$, respectively, and the values of the auxiliary measurements by $\theta_b, \theta_L, \theta_\epsilon, \theta_t, \theta_{E_{\text{JER}}}, \theta_{E_{\text{JES}}}, \theta_S$, respectively.

6.5.2.3 Likelihood function definition

A binned likelihood is used in this analysis. Consider the m_{jj} histogram of $\mathbf{n} = (n_1, \dots, n_N)$ events, the likelihood function without uncertainties is built as:

$$\mathcal{L}(\mu; b_{\text{tot}}, \mathbf{p}_s, \mathbf{p}_b) = \prod_{i=1}^N \frac{(\mu s_i + b_i)^{n_i}}{n_i!} e^{-(\mu s_i + b_i)}, \quad (6.16)$$

where the parameter of interest (POI) μ is the signal strength parameter, b_i is the number of background events in the i bin, s_i is the number of signal events in the i bin.

Background-only hypothesis corresponding to $\mu = 0$, whereas nominal signal hypothesis corresponding to $\mu = 1$.

The full likelihood function with uncertainties included is defined as:

$$\begin{aligned} \mathcal{L}(\mu; b_{\text{tot}}, \mathbf{p}_s, \mathbf{p}_b, \boldsymbol{\alpha}_s) &= \prod_{i=1}^N \frac{(\mu_i^T)^{n_i}}{n_i!} e^{-\mu_i^T} N_i(\alpha_L; \theta_L, \delta_L) N_i(\alpha_\epsilon; \theta_\epsilon, \delta \epsilon) \\ &\quad \cdot N_i(\alpha_t; \theta_t, \delta E_t) N_i(\alpha_{E_{\text{JER}}}; \theta_{E_{\text{JER}}}, \delta E_{\text{JER}}) \end{aligned} \quad (6.17)$$

$$\cdot \quad N_i(\alpha_{E_{\text{JES}}}; \theta_{E_{\text{JES}}}, \delta E_{\text{JES}}) N_i(\alpha_s; \theta_s, \delta_s), \quad (6.18)$$

1705 where μ_i^T is the total number of expected event in the i bin, which is given by:

$$\mu_i^T = \mu s_i \eta_i^L(\alpha_L) \eta_i^\epsilon(\alpha_\epsilon) \eta_i^t(\alpha_t) \eta_i^{E_{\text{JER}}}(\alpha_{E_{\text{JER}}}) \eta_i^{E_{\text{JES}}}(\alpha_{E_{\text{JES}}}) + b_i. \quad (6.19)$$

1706 The parameter $\eta^s(\alpha_s)$ are response functions for uncertainty s , and the subsidiary mea-
1707 surements are constrained by the $N(\alpha; \theta, \delta)$ functions.

1708 In this analysis, constraint functions are built from standard Gaussians, together
1709 with uncertainties that mapped in the response functions. Luminosity uncertainty is
1710 fitted by a log-normal response function, the JER and JES uncertainties are given by
1711 Gaussian and asymmetric response functions, respectively. For each bin, a vertical inter-
1712 polation strategy called piece-wise linear method is used independently. In the case of
1713 the asymmetric error, the polynomial interpolation and exponential extrapolation method
1714 is used.

1715 The parameters $(\mu, N_b, p_s, p_b, \alpha_L)$ are fixed from the fit to data (pseudo-data) and
1716 are common for all bins, whereas parameters $(\alpha_\epsilon, \alpha_t, \alpha_{E_{\text{JER}}}, \alpha_{E_{\text{JES}}}, \alpha_s)$ are different from
1717 bin to bin.

1718 For simplicity in notation, the 18 nuisance parameters are written as the vector α ,
1719 where six of them have corresponding uncertainties. The simplified likelihood function
1720 is written as:

$$\mathcal{L}(\mu; \alpha) = \prod_{i=1}^N \frac{[\mu_i^T(\mu, \alpha)]^{n_i}}{n_i!} e^{-\mu_i^T(\mu, \alpha)} \prod_{s=1}^6 G_{i,s}(\alpha_s). \quad (6.20)$$

1721 6.5.2.4 Statistical Method

1722 A hypothesis test is used for estimating the compatibility between data and a theo-
1723 retical hypothesis, where the pseudo datasets are generated according to a given hypoth-
1724 esis, and compared to the tested dataset in terms of a test statistic.

1725 The procedure is demonstrated as follows: first, the agreement between the col-
1726 lected data and the null hypothesis is evaluated through a hypothesis test. The null hy-
1727 pothesis ($\mu = 0$) posits that only the SM background is present. If the data does not
1728 exhibit any substantial excess under this hypothesis test, the subsequent step involves es-
1729 tablishing an exclusion limit for the targeted signal model on the resonance cross section
1730 for m_{jj} . In this scenario, the hypothesis transforms into a signal + background assump-

1731 tion, leading to the construction of a test statistic based on the signal + background PDF
 1732 of the discriminating variable.

1733 The statistical measurement's p-value serves as a quantification of the degree of
 1734 agreement or discrepancy between a hypothesis and the observed data. Mathematically,
 1735 it represents the integral of the distribution of the test statistic from the value obtained
 1736 for the dataset in question to infinity. This value characterizes the probability of achiev-
 1737 ing the observed outcomes assuming the null hypothesis. A lower p-value indicates a
 1738 higher degree of statistical significance for the observed incompatibility. For instance,
 1739 if the p-value of the data is below 0.05, it signifies that the likelihood of the observed
 1740 data aligning with the hypothesis is less than 5%. This prompts the assertion that the
 1741 hypothesis can be excluded at the 95% confidence level (CL).

1742 **6.5.2.5 Test statistic and p-value definitions**

1743 A binned maximum likelihood (ML) fitting method is used to extract the signal,
 1744 together with profile likelihood ratio test statistic. The test statistics used for claiming a
 1745 positive signal is defined as:

$$q_0 = \begin{cases} -2 \ln \frac{\mathcal{L}(0, \hat{\alpha}(0))}{\mathcal{L}(\hat{\mu}, \hat{\alpha})} & \hat{\mu} \geq 0, \\ 0 & \hat{\mu} < 0. \end{cases} \quad (6.21)$$

1746 and the test statistic used for evaluating the upper limits is given as:

$$\tilde{q}_\mu = \begin{cases} -2 \ln \frac{\mathcal{L}(\mu, \hat{\alpha}(\mu))}{\mathcal{L}(0, \hat{\alpha}(0))} & \hat{\mu} < \mu, \\ -2 \ln \frac{\mathcal{L}(\mu, \hat{\alpha}(\mu))}{\mathcal{L}(\hat{\mu}, \hat{\alpha})} & 0 \leq \hat{\mu} \leq \mu, \\ 0 & \hat{\mu} > \mu. \end{cases} \quad (6.22)$$

1747 where the parameter μ represents the signal strength associated with the hypothesis being
 1748 tested. The maximum likelihood (ML) estimators that optimize the likelihood function
 1749 \mathcal{L} without constraints are referred to as $\hat{\mu}$ for the signal strength and $\hat{\alpha}$ for the other pa-
 1750 rameters. The parameter $\hat{\alpha}$ represents the conditional ML estimator of α that maximizes
 1751 \mathcal{L} while considering a specific value of μ .

1752 The p-value corresponding to the background-only hypothesis is expressed as:

$$p_0 = \int_{q_{0,\text{obs}}}^{\infty} f(q_0|0) dq_0. \quad (6.23)$$

1753 The values of \tilde{q}_μ are calculated for different values of μ by fitting a dataset where

1754 the pseudo data is represented by μ' . This calculation of \tilde{q}_μ is conducted for each pseudo
 1755 dataset at various selected signal mass points, resulting in a distribution of \tilde{q}_μ denoted as
 1756 $f(\tilde{q}_\mu | \mu = \mu')$. As a result, a p-value for the tested dataset is determined based on this
 1757 distribution:

$$p_{\mu'} = \int_{\tilde{q}'_{\mu,\text{obs}}}^{\infty} f(\tilde{q}_\mu | \mu = \mu') dq_\mu, \quad (6.24)$$

1758 the term $\tilde{q}'_{\mu,\text{obs}}$ represents the computed value of the test statistic based on the dataset
 1759 being tested. These p-values are also referred to as p_{s+b} , which signifies that they are
 1760 associated with the signal plus background hypothesis.

1761 6.5.2.6 Generation of pseudo-data

1762 The PDF of a certain model is used for generating the pseudo datasets. Signal +
 1763 background pseudo datasets are utilized to estimate the observed confidence level (CL) of
 1764 a signal + background hypothesis, while background-only pseudo datasets are employed
 1765 for expected CL estimations.

1766 During the generation of pseudo datasets, all parameters in the PDF are set to their
 1767 nominal values. The expected event counts in each bin follow a Poisson distribution.
 1768 Nuisance parameters (NPs), which represent systematic uncertainties, are treated ac-
 1769 cording to the "unconditional ensemble" approach: for each pseudo dataset, the values
 1770 of α_i (associated with the NPs) are drawn from their respective constraint terms, and
 1771 these values are used in both the likelihood \mathcal{L} and the computation of \tilde{q}_μ .

1772 6.5.2.7 Definition of exclusion limit

1773 The data is interpreted by the modified frequentest method (CL_s method), where
 1774 p-value is modified to take into account downward background fluctuations and quoted
 1775 as CL_s . The definition of CL_s is:

$$CL_s = \frac{p_{s+b}}{1 - p_b}, \quad (6.25)$$

1776 where $p_{b(s+b)}$ is the integrated value of the background-only (signal + background) dis-
 1777 tribution from zero to $\tilde{q}_\mu^{\text{obs}}$. Thus $1 - p_b$ is also referred to as the confidence level of the
 1778 background-only hypothesis (CL_b). The CL_s limit claims exclusion at 95% CL when
 1779 $CL_s = 0.05$.

1780 **6.5.2.8 Implementation**

1781 The statistical approach employed in this analysis differs slightly from previous
 1782 dijet analyses and aligns with the current trigger-level analysis. In previous approaches,
 1783 a background model devoid of NPs was fitted to the data, and the resulting background
 1784 fit parameters were employed (and held constant) in subsequent likelihood fits involving
 1785 nuisance parameters. However, in this analysis, the background fit parameters are treated
 1786 as unconstrained NPs within the complete likelihood framework used in all fits.

1787 To create the RooFit workspaces, the XML Analytic Workspace Builder is utilized.
 1788 The xRooFit tool processes these workspaces and performs operations like setting limits,
 1789 among others, using classes from the RooFit and RooStats libraries.

1790 **6.5.3 Background Estimation**

1791 In the resonant search the SM background of the m_{jj} spectrum is established
 1792 through a functional fitting procedure applied to the data. Refs. [33, 42, 27, 50, 10,
 1793 28]) have found that a parametric function of the form

$$f(x) = p_1(1-x)^{p_2}x^{p_3+p_4 \ln x + p_5 (\ln x)^2}, \quad (6.26)$$

1794 where $x \equiv m_{jj} / \sqrt{s}$, accurately describes dijet mass distribution predicted by leading and
 1795 next-to-leading-order QCD Monte Carlo. In the ATLAS Run 2 analysis with 139.0 fb^{-1}
 1796 of data [29, 73], the four parameter version of the function ($p_5 = 0$) was found to suffi-
 1797 ciently described the data. The introduction of gluon tagging may require more parame-
 1798 ters to properly describe the full invariant mass spectrum.

1799 To avoid introducing any potential bias due to the selection of a specific background
 1800 function, an alternative functional form is employed. This alternative form is inspired by
 1801 the one used by the UA2 experiment [5, 6] when observing the decay of W and Z bosons
 1802 into two jets, followed by a subsequent search.

$$f(x) = p_1 x^{p_2} \exp(p_3 x + p_4 x^2). \quad (6.27)$$

1803 **6.5.4 Analysis Strategy**

1804 The analysis begins with the utilization of skimmed ntuples, which are the result
 1805 of applying the event selection criteria outlined in Section 6.4.3. These ntuples serve as

1806 the basis for generating pseudo-data using the background-only model. Subsequently,
 1807 a 4-parameter ($p_5 = 0$) fit function described by Equation 6.26 is employed to fit this
 1808 pseudo-data. The fit to the data is deemed satisfactory if it meets the following criterion:

- 1809 • Global χ^2 p -value > 0.05

1810 If the conditions mentioned above are satisfied, the background is chosen for the
 1811 purpose of upper limit estimations. Conversely, if the criteria are not met, the 5-parameter
 1812 version of Equation 6.26 is employed for background fitting and is subjected to the same
 1813 selection criterion. If the fit using the 5-parameter function also fails to meet the cri-
 1814 teria, the analysis reduces the range of the window and repeats the fitting process with
 1815 the 5-parameter function to see if a satisfactory fit can be achieved. If this attempt still
 1816 does not meet the criteria, the analysis switches to an alternative option for generating
 1817 pseudo-data. Once a fit satisfying the criteria is obtained, the fit function undergoes var-
 1818 ious validation tests to ensure the appropriateness of the fit strategy. The flowchart of
 1819 Figure 6.76 shows the analysis strategy.

1820 **6.5.5 Spurious Signal Tests**

1821 The spurious signal test is designed to estimate the difference between the signal
 1822 yields from the fit and the expected signal yields that given by fitting a known template
 1823 signal model on a smooth background distribution. Such difference is considered as fit
 1824 bias and defined as S_{spur} :

$$S_{\text{spur}} = S_{\text{fit}} - S_{\text{template}} \quad (6.28)$$

1825 It is crucial to verify the stability of the fit when applied to a background-only
 1826 distribution. In this context, no signal is intentionally introduced into the yields, ensuring
 1827 that the extracted number of signal events remains zero. In the spurious signal test, S_{spur}
 1828 is determined by fitting a model comprising both signal and background components
 1829 onto a background-only template. The corresponding uncertainty from the fit is denoted
 1830 as σ_{fit} . Both the spurious signal S_{spur} and its associated uncertainty σ_{fit} are expected to be
 1831 consistent with zero.

1832 The estimation of the spurious signal is consequently conducted through these pseudo-
 1833 experiments. The mean value across all experiments is calculated, and a total of 100
 1834 pseudo-experiments have been employed. For each individual signal hypothesis, the

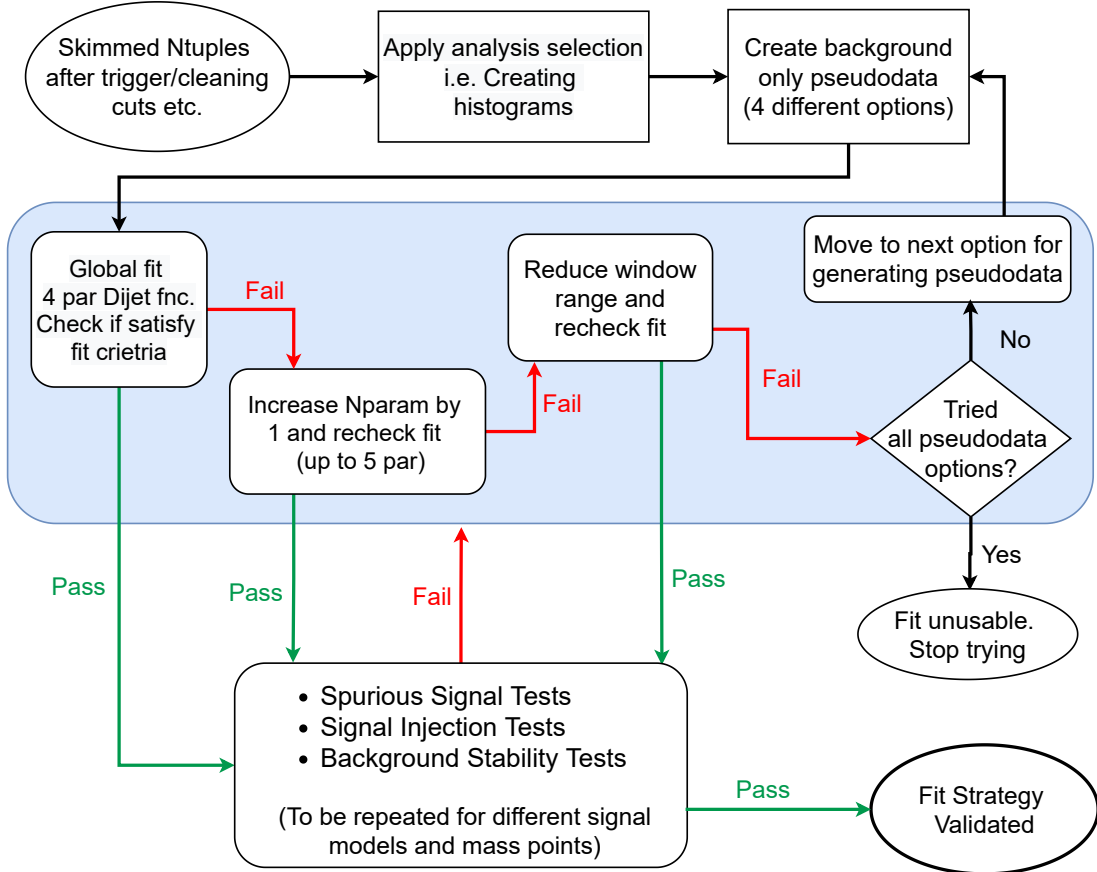


Figure 6.76 Analysis top-level flowchart.

1835 assessment of spurious signals is conducted at various mass points. This is done in
 1836 individually for each signal hypothesis and at each mass point. The outcomes of the
 1837 model-independent tests for Gaussian signals, considering different masses and widths,
 1838 are consolidated in Table 6.35 for the 1 gluon-tagged category and in Table 6.36 for the
 1839 2 gluon-tagged category. Correspondingly, the findings for string signals characterized
 1840 by different string scales are presented in Table 6.37.

1841 Following the recommendations of the Statistical PUB Note [25], the spurious
 1842 signal is required to be

$$S_{\text{spur}} < (20\% - 50\%) \sigma_{\text{fit}} \quad (6.29)$$

1843 The idea criteria is when the spurious signal satisfy: $S_{\text{spur}} < 30\% \sigma_{\text{fit}}$, but can be
 1844 loosen up to 50% σ_{fit} . Most of the tested mass points and widths satisfy the spurious
 1845 signal criteria.

Mass TeV	Width percentage [%]	Median ± Rms S_{spurious} ± Uncertainty	Ratio $S_{\text{spurious}}/\text{Uncertainty}$
2	5	0.19 2 ± 802.85 2	2.36E-042
2	10	3.35 2 ± 1313.792	2.55E-032
2	15	154.92 2 ± 1666.6 2	0.093 2
3	5	1.76 2 ± 249.13 2	7.06E-032
3	10	82.55 2 ± 520.85 2	0.158 2
3	15	344.74 2 ± 803.85 2	0.429 2
4	5	48.42 2 ± 112.34 2	0.431 2
4	10	115.89 2 ± 200.83 2	0.577 2
4	15	2.02 2 ± 242.15 2	8.34E-032
5	5	0.021 2 ± 31.77 2	6.61E-042
5	10	0.012 2 ± 31.96 2	3.75E-042
5	15	0.006 2 ± 18.98 2	3.16E-042
6	5	7.82E-042 ± 5.54 2	1.41E-042
6	10	2.84E-042 ± 5.93 2	4.79E-052
6	15	3.62E-042 ± 5.79 2	6.25E-052
7	5	8.65E-042 ± 2.66 2	3.25E-042
7	10	1.6E-04 2 ± 2.59 2	6.18E-052
7	15	8.34E-052 ± 2.71 2	3.08E-052

Table 6.35 Spurious Signal tests using Gaussian signals for 1 gluon tagged category.

Mass TeV	Width percentage [%]	Median ± Rms $S_{\text{spurious}} \pm \text{Uncertainty}$	Ratio $S_{\text{spurious}}/\text{Uncertainty}$
2	5	179.84 2 ± 635.08 2	0.283 2
2	10	757.07 2 ± 1265.99 2	0.598 2
2	15	1666.24 2 ± 2126.08 2	0.784 2
3	5	1.83E-032 ± 85.31 2	2.14E-05 2
3	10	0.27 2 ± 125.63 2	2.15E-03 2
3	15	0.021 2 ± 113.74 2	1.85E-04 2
4	5	1.91E-032 ± 25.6 2	7.46E-05 2
4	10	3.55E-032 ± 38.68 2	9.18E-05 2
4	15	1.50E-032 ± 27.01 2	5.55E-05 2
5	5	2.72E-042 ± 7.13 2	3.81E-05 2
5	10	9.99E-052 ± 5.57 2	1.79E-05 2
5	15	2.1E-04 2 ± 4.72 2	4.45E-05 2
6	5	1.37E-042 ± 1.92 2	7.14E-05 2
6	10	1.47E-042 ± 3.25 2	4.52E-05 2
6	15	6.49E-052 ± 2.59 2	2.51E-05 2
7	5	1.88E-042 ± 1.19 2	1.58E-04 2
7	10	1.17E-042 ± 1.17 2	1.0E-04 2
7	15	7.83E-052 ± 1.20 2	6.53E-05 2

Table 6.36 Spurious Signal tests using Gaussian signals for 2 gluon tagged category.

String scale TeV	Median ± Rms	Ratio
	S_{spurious} ± Uncertainty	$S_{\text{spurious}}/\text{Uncertainty}$
7	4.12E-042 ± 5.832	7.07E-052
7.5	1.6E-042 ± 3.722	2.84E-052
8	6.77E-052 ± 2.112	3.21E-052
8.5	3.83E-052 ± 1.842	2.08E-052
9	3.87E-052 ± 1.932	2.01E-052

Table 6.37 Spurious Signal tests using String signals.

 1846 **6.5.6 Fit Stability Tests**

1847 The fit stability tests are employed to assess the behaviour of the background fit
 1848 function under different scenarios: when applied to the background-only template and
 1849 the signal + background template. A comparison is made between the fit results obtained
 1850 from these two templates. Ideally, the background fit function should yield consistent
 1851 outcomes in both cases. The results of these fit stability tests are presented in Table 6.38
 1852 through Table 6.39, encompassing various signal strengths and mass points.

1853 Notably, the background estimation derived from the signal + background fit (B_1)
 1854 aligns with the background estimation obtained from the background-only fit (B_2), indi-
 1855 cating good agreement between the two approaches.

Mass (TeV)	Width (percentage)	Signal Strength	B_1 from S+B fit	B_2 from B-only fit
			Mean \pm Rms	Mean \pm Rms
2	5	1	20062716.452 \pm 4370.572	20064025.612 \pm 4003.072
2	5	3	20063730.272 \pm 4882.092	20067248.182 \pm 4003.142
2	5	5	20062961.532 \pm 4521.622	20070470.902 \pm 4003.362
5	5	1	20062414.492 \pm 4005.802	20062458.642 \pm 4003.052
5	5	3	20062420.852 \pm 4002.942	20062547.112 \pm 4003.092
5	5	5	20062420.962 \pm 4002.822	20062635.822 \pm 4003.252
5	10	1	20062435.182 \pm 4010.372	20062483.502 \pm 4002.872
5	10	3	20062448.752 \pm 4007.222	20062622.262 \pm 4002.952
5	10	5	20061413.122 \pm 3682.052	20062761.082 \pm 4003.122
7	5	1	20062420.382 \pm 4002.682	20062420.292 \pm 4002.982
7	5	3	20062422.562 \pm 4002.862	20062432.082 \pm 4003.082
7	5	5	20062422.862 \pm 4002.982	20062444.092 \pm 4003.202

Table 6.38 Fit Stability tests using Gaussian signals for 1 gluon tagged category.

Mass (TeV)	Width (percentage)	Signal Strength	B_1 from S+B fit		B_2 from B-only fit	
			Mean \pm Rms	Mean \pm Rms	Mean \pm Rms	Mean \pm Rms
2	5	1	3901512.922 \pm 2163.272	3902240.712 \pm 2048.042		
2	5	3	3901530.762 \pm 2166.982	3903253.552 \pm 2047.372		
2	5	5	3901621.902 \pm 2291.012	3905032.952 \pm 2050.682		
5	5	1	3901529.752 \pm 2049.312	3901559.922 \pm 2046.182		
5	5	3	3901528.522 \pm 2049.152	3901589.412 \pm 2044.932		
5	5	5	3901533.992 \pm 2047.482	3901621.882 \pm 3901586.682		
5	10	1	3901536.862 \pm 2047.402	3901566.442 \pm 2048.232		
5	10	3	3901535.712 \pm 2054.622	3901616.492 \pm 2050.262		
5	10	5	3901538.472 \pm 2049.542	3901670.562 \pm 2047.942		
7	5	1	3901531.272 \pm 2047.302	3901538.452 \pm 2049.162		
7	5	3	3901540.722 \pm 2068.732	3901542.752 \pm 2048.462		
7	5	5	3901533.132 \pm 2052.642	3901540.092 \pm 2048.942		

Table 6.39 Fit Stability tests using Gaussian signals for 2 gluon tagged category.

1856 **6.6 Systematic uncertainties**

1857 **6.6.1 String resonance systematic uncertainties**

1858 As described in Section 4.2, JES and JER systematic uncertainties are considered
1859 for the String resonances. In this study, three NPs from the JES and 7 NPs from the JER
1860 are studied on the normalised template shapes.

1861 The impact from JES on the signal template is evaluated by comparing the nominal
1862 distribution to the distribution from each JES NP. The impact from JER on the signal
1863 template is estimated by examining the shift in the RMS (or standard deviation) of the
1864 distribution from each JER NP. Such signal shifts are parameterised by fitting a Gaus-
1865 sian function to the most significant bins surrounding the maximum mean value of the
1866 distribution.

1867 Figure 6.77 shows an example for the $M_s = 8$ TeV signal sample. This histogram
1868 exemplifies one of the systematic variations employed in the subsequent limit calcula-
1869 tion. Among the various systematic sources, GroupedNP_3 emerges as having the most
1870 substantial impact, leading to a significant shift in the signal mean. Across signal samples
1871 of diverse masses and widths, the reconstructed peak of the signal demonstrates a shift
1872 towards lower values in comparison to the generated peak, amounting to approximately
1873 $0.92 \times M_s$. It is important to note that this shift is present even before accounting for the
1874 JES or JER systematic uncertainties.

1875 In Figure 6.78, the proportional shift in the mean of the m_{jj} distribution attributed
1876 to the JES uncertainty and the relative change in RMS of the m_{jj} distribution due to the
1877 JER uncertainty are depicted. While all the NPs are independently incorporated in the
1878 limit computations, this illustration presents a combined display of the three JES mean
1879 shifts in quadrature and the seven JER resolution differences in quadrature.

1880 The alterations in signal acceptance from the inclusion of JES and JER uncertainties
1881 are combined in quadrature and determined to be less than 0.06%. Such small uncertainty
1882 can be ignored for the signal acceptance.

1883 The shifts in the mean of the signal distributions, resulting from the inclusion of
1884 JES uncertainty, are primarily driven by GroupedNP_3 and amount to less than 4%.
1885 Conversely, the alterations in the RMS of the signal distributions following the incor-
1886 poration of JER uncertainty remain below 1.2%. Among the seven values combined in
1887 quadrature, none exhibit a dominant influence. Notably, the JER uncertainty emerges as

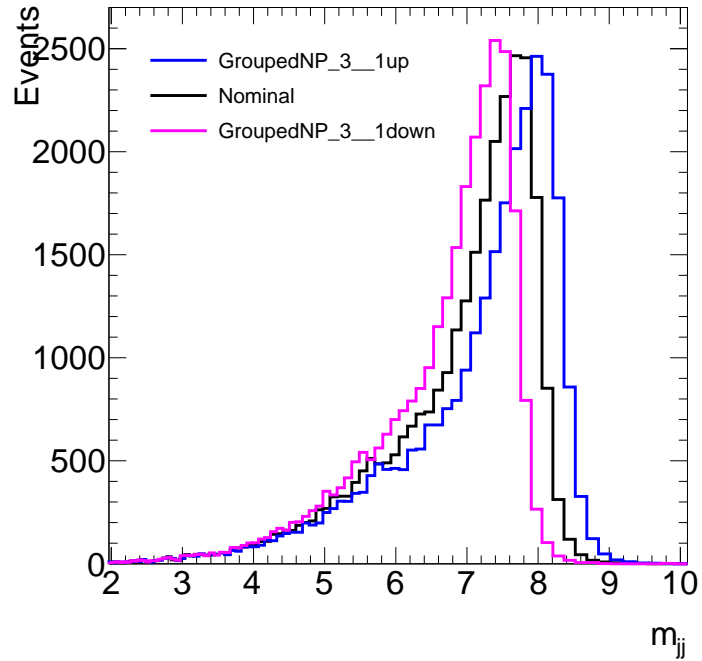


Figure 6.77 m_{jj} distribution for the $M_s = 8$ TeV string sample (nominal). Also shown are the distributions using the jet energy scale GroupedNP_3 one standard deviation up and down systematic uncertainties.

1888 the most substantial source of uncertainty for the lowest M_s signal sample.

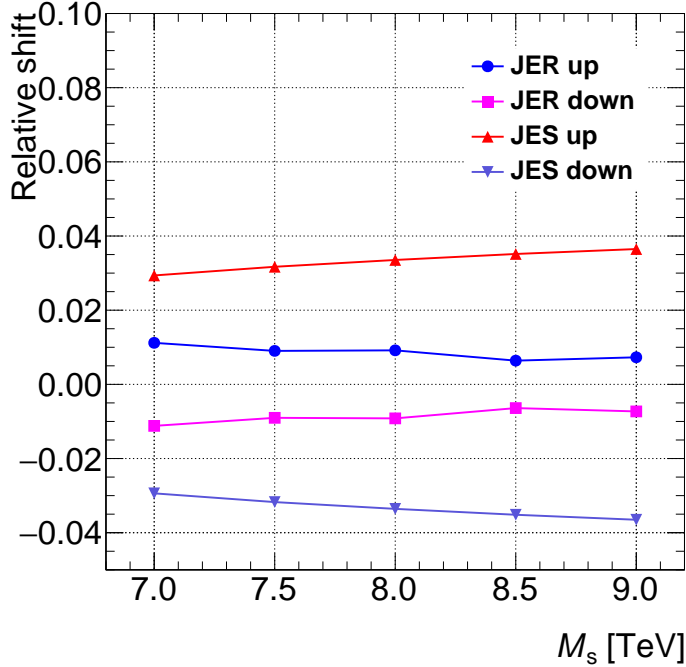


Figure 6.78 Relative shift in the mean of the m_{jj} distributions for each string sample due to jet energy scale uncertainty, and relative change in the RMS of the m_{jj} distributions for each string sample due to the jet energy resolution uncertainty. The changes due to each nuisance parameter group are added in quadrature.

1889 6.6.2 q/g tagging Systematics

1890 6.6.2.1 Pure MC Systematics

1891 Indeed, obtaining uncertainties for a q/g tagger built upon track multiplicity poses
 1892 challenges, particularly in the higher p_T range. This difficulty is partly attributed to the
 1893 limited statistics available beyond 1 TeV, where fewer gluon-jets are present due to their
 1894 tendency to be produced at lower masses compared to quark-jets. Consequently, an issue
 1895 arises in equations that necessitate the average number of tracks in quark- or gluon-jets to
 1896 facilitate calculations. The scarcity of data points at higher p_T values hampers the robust
 1897 estimation of these averages, contributing to the uncertainty challenge in this context.

1898 The determination of the fraction of jets classified as quark- or gluon-initiated jets
 1899 is accomplished through the ratio f_q^f/f_g^c , where the superscript f (c) designates the jet
 1900 with the higher (lower) η value in simulated dijet events. These fractions are derived by
 1901 convolving parton distribution functions with matrix element calculations. The number
 1902 of charged tracks events in the jet with higher η can be described by the following system

1903 of equations [23]:

$$\langle n_{\text{charged}}^f \rangle = f_q^f \langle n_{\text{charged}}^q \rangle + f_g^f \langle n_{\text{charged}}^g \rangle \quad \langle n_{\text{charged}}^c \rangle = f_q^c \langle n_{\text{charged}}^q \rangle + f_g^c \langle n_{\text{charged}}^g \rangle. \quad (6.30)$$

1904 These equations require two samples with different fractions of quark- and gluon-
 1905 jets. While theoretically valid even at high p_T values, their applicability diminishes in the
 1906 high p_T regime due to the exceedingly small fractions of gluon jets. Notably, the main
 1907 sources of uncertainty stem from discrepancies in the MC modelling and the challenges
 1908 associated with reconstructing charged tracks within jets. This is especially relevant as
 1909 the separation between tracks is comparable to the resolution of the detector. Conse-
 1910 quently, the efficiency of the tagger relies on the accurate resolution of tracks for precise
 1911 N_{trk} determination, which in turn is constrained by available statistics.

1912 They systematic uncertainty can be estimated by using pure MC simulations and
 1913 is expected to be substantial, yet smaller than that obtained from data at the edges of
 1914 the mass range. This technique is particularly effective where statistics are not limited,
 1915 such as in the central region of the p_T distribution. Such an approach has proven to be
 1916 the optimal choice. To extend the uncertainties into the higher p_T regime, particle-level
 1917 effects and MC reconstruction effects are incorporated. These uncertainties pertain to
 1918 "in-situ" considerations, making it reasonable to employ them during an extrapolation
 1919 procedure.

1920 The procedure is performed at constant p_T ranges, as N_{trk} depends only on p_T and
 1921 the parton type that initiating jets, uncertainties can be computed by comparing the dis-
 1922 tribution of N_{trk} in bins of jet p_T , which generated from different simulation models.
 1923 Thus different type of MC generators could introduce underlying uncertainties to the re-
 1924 sults. Details on different types of uncertainties and the samples used to estimate them
 1925 are described in Section 5.7. Six working points (10%, 25%, 40%, 50%, 60% and 75%)
 1926 are provided for fixed efficiency curves.

1927 **6.7 Results**

1928 **6.7.1 Untagged Resonances: Model-independent Gaussian Limits**

1929 One way to demonstrate the search in the analysis is to set limits on the cross-section
1930 of signal modes. Here a model-independent signal as Gaussian are used to expand the
1931 sensitivity of the search to new signals that may be detectable with this analysis but
1932 not currently theoretically described. Besides, a model-independent signal could help to
1933 evaluate and compare the strength of different analyses without bias, as the case where
1934 specific models are applied and leads less sensitive to the search.

1935 Therefore, model-independent limits are produced based on model-independent sig-
1936 nal resonances. Because this analysis is sensitive to the shape of resonance, specific
1937 models with different shapes would influence the results strongly. In general, a model-
1938 independent signal is a good feature of the analysis which verify the ability to distinguish
1939 different signal models, although the model-independent limits are still influenced by the
1940 shape of the resonance in an implicit way. The motivation to choose a Gaussian reso-
1941 nance as a proxy is the fact that it is similar to the ‘average’ signal with specific width.
1942 Besides, the shape of reconstructed jet p_T of any realistic signal without very specific
1943 model is produced approximately as a Gaussian resonance, without applied JER. Hence
1944 it is straightforward to use Gaussian resonances to represent any realistic resonance:

1945 The untagged $y^* < 0.8$, 1-g tagged $y^* < 0.6$ and 2-g tagged $y^* < 0.8$ model-independent
1946 Gaussian limits are shown in fig 6.79, 6.80 and 6.81 respectively, for Gaussians with
1947 width equal to 0, 3, 5, 7, 10 and 15% of their peak position, without systematics in-
1948 cluded.

Search for new phenomena in dijet events

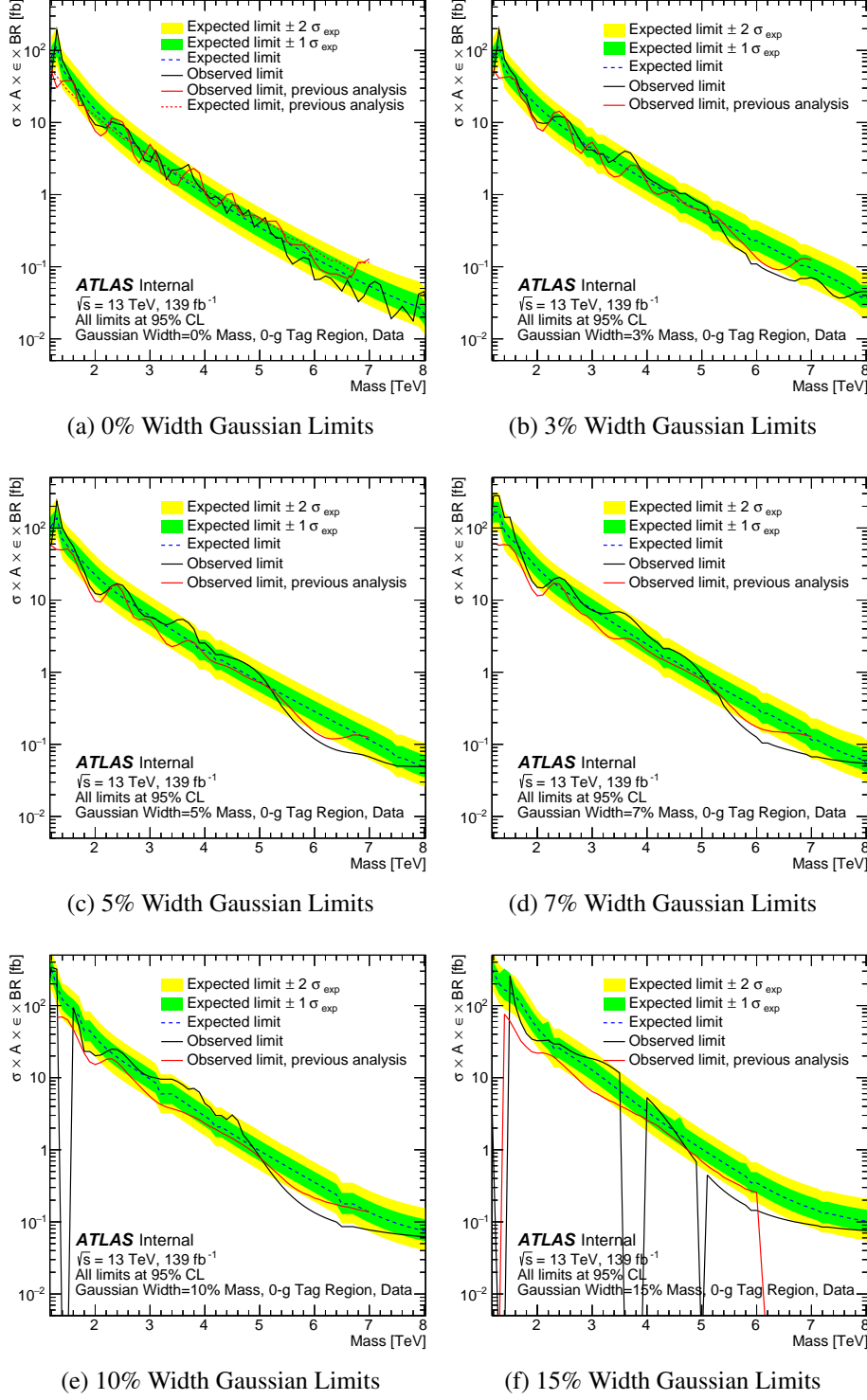


Figure 6.79 Model-independent limits set in the untagged $y^* < 0.8$ Signal Region using Gaussian resonances of varying widths from 0% to 15% of their peak position without systematics included using the full 139fb^{-1} Run-2 dataset.

Search for new phenomena in dijet events

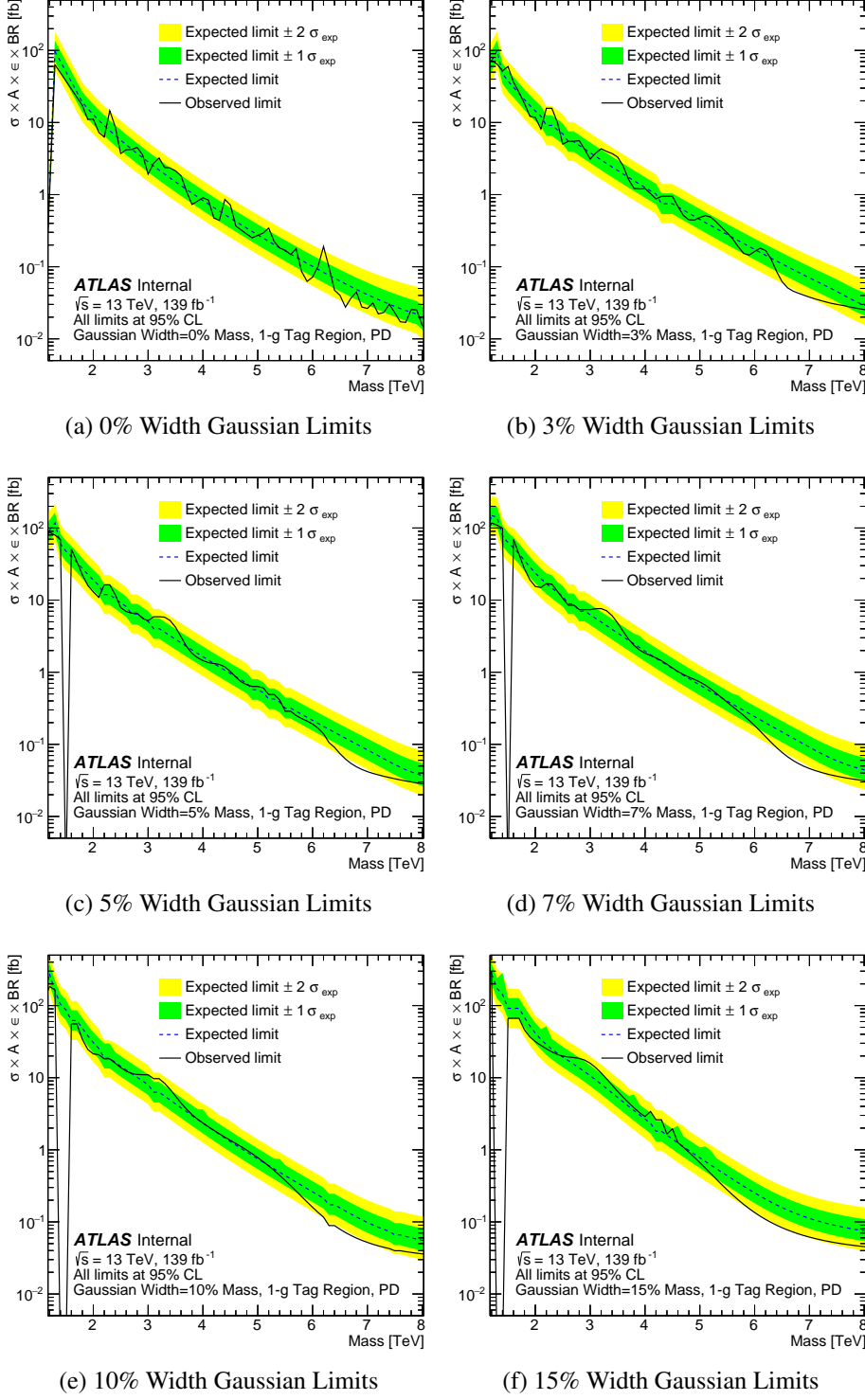


Figure 6.80 Model-independent limits set in the 1-g tagged $y^* < 0.6$ Signal Region using Gaussian resonances of varying widths from 0% to 15% of their peak position without systematics included using the full 139fb^{-1} Run-2 dataset.

Search for new phenomena in dijet events

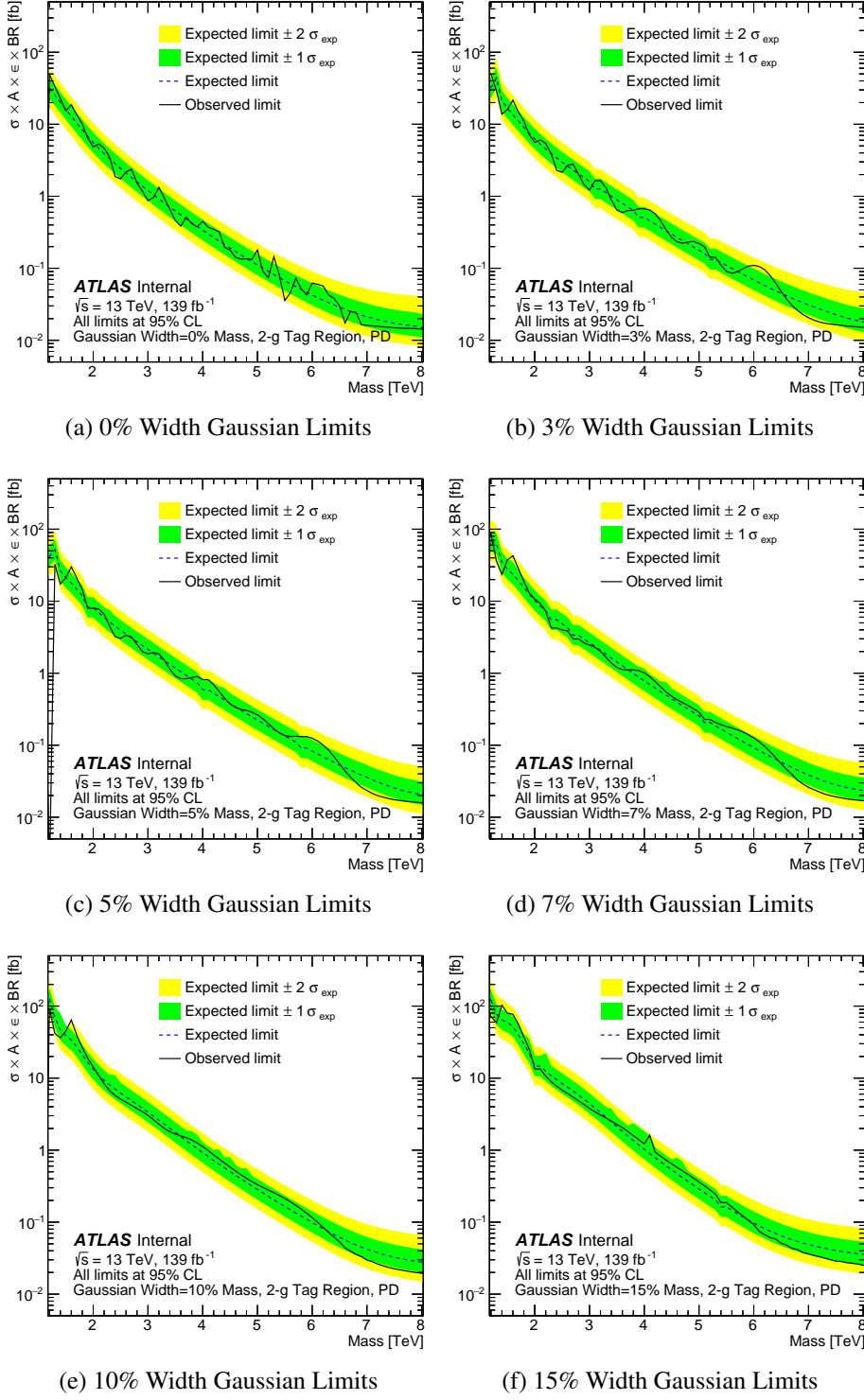


Figure 6.81 Model-independent limits set in the 2-g tagged $y^* < 0.8$ Signal Region using Gaussian resonances of varying widths from 0% to 15% of their peak position without systematics included using the full 139 fb^{-1} Run-2 dataset.

1949

7 Conclusions

1950 From 2015 to 2018, the proton-proton collision at the LHC have achieved an unprece-
1951 dented centre-of-mass energy of $\sqrt{s} = 13$ TeV, with a total integrated luminosity of 140
1952 fb^{-1} that have been recorded by the ATLAS experiment. Such huge amount of collision
1953 data allow scientists test models beyond the SM in a more efficient way, leading a deeper
1954 understanding of physics beyond the SM.

1955 In this thesis, jet taggers are built using the charged multiplicity information pro-
1956 vided by the ID to distinguish quark-initiated and gluon-initiated jets. In order to com-
1957 pensate the data and MC difference, a calibration procedure has been done using matrix
1958 method. Four working points of 50%, 60%, 70%, 80% together with all systematics are
1959 provided so that analyses can use it based on their own interest.

1960 This thesis presents the search for new resonances that potentially decay into a pair
1961 of jets using the data collected by the ATLAS detector during 2015-2018. Resonances
1962 predicted by the BSM can decay into quarks and/or gluons, by introducing jet taggers,
1963 the sensitivity of the search could be significantly increased. In this analysis, searches
1964 are performed on m_{jj} spectrum. Benchmark models H' , String, and QBH are tested, as
1965 well as model-independent Gaussians. Because no significant excess in data are found,
1966 a upper limit is set to each model.

1967

REFERENCES

- 1968 [1] A. Buckley et al. “LHAPDF6: parton density access in the LHC precision era”.
1969 In: *Eur. Phys. J. C* 75 (2015), p. 132. DOI: <https://doi.org/10.1140/epjc/s10052-015-3318-8>. arXiv: [1412.7420](https://arxiv.org/abs/1412.7420) [hep-ph].
- 1970
1971 [2] B. Abbott et al. “Production and integration of the ATLAS Insertable B-Layer”.
1972 In: *JINST* 13 (2018), T05008. DOI: [10.1088/1748-0221/13/05/T05008](https://doi.org/10.1088/1748-0221/13/05/T05008).
1973 arXiv: [1803.00844](https://arxiv.org/abs/1803.00844) [physics.ins-det].
- 1974 [3] Takuya Akiba et al. *Optuna: A Next-generation Hyperparameter Optimization Framework*. 2019. arXiv: [1907.10902](https://arxiv.org/abs/1907.10902) [cs.LG].
- 1975
1976 [4] Simone Alioli et al. “A general framework for implementing NLO calculations in
1977 shower Monte Carlo programs: the POWHEG BOX”. In: *JHEP* 06 (2010), p. 043.
1978 DOI: [10.1007/JHEP06\(2010\)043](https://doi.org/10.1007/JHEP06(2010)043). arXiv: [1002.2581](https://arxiv.org/abs/1002.2581) [hep-ph].
- 1979 [5] J. Alitti et al. “A Measurement of two jet decays of the W and Z bosons at the
1980 CERN $\bar{p}p$ collider”. In: *Z. Phys. C* 49 (1991), pp. 17–28. DOI: [10.1007/BF01570793](https://doi.org/10.1007/BF01570793).
- 1981
1982 [6] J. Alitti et al. “A Search for new intermediate vector mesons and excited quarks
1983 decaying to two jets at the CERN $\bar{p}p$ collider”. In: *Nucl. Phys. B* 400 (1993),
1984 pp. 3–24. DOI: [10.1016/0550-3213\(93\)90395-6](https://doi.org/10.1016/0550-3213(93)90395-6).
- 1985 [7] G. Altarelli and G. Parisi. “Asymptotic freedom in parton language”. In: *Nucl.*
1986 *Phys. B* 126.2 (1977), pp. 298–318. DOI: [https://doi.org/10.1016/0550-3213\(77\)90384-4](https://doi.org/10.1016/0550-3213(77)90384-4).
- 1987
1988 [8] A. Altheimer et al. “Jet substructure at the Tevatron and LHC: new results, new
1989 tools, new benchmarks”. In: *J. Phys. G* 39 (2012), p. 063001. DOI: [10.1088/0954-3899/39/6/063001](https://doi.org/10.1088/0954-3899/39/6/063001). arXiv: [1201.0008](https://arxiv.org/abs/1201.0008) [hep-ph].
- 1990
1991 [9] J. R. Andersen et al. “Les Houches 2015: Physics at TeV Colliders Standard Model
1992 Working Group Report”. In: *9th Les Houches Workshop on Physics at TeV Colliders*. May 2016. arXiv: [1605.04692](https://arxiv.org/abs/1605.04692) [hep-ph].
- 1993

REFERENCES

- 1994 [10] ATLAS Collaboration. “A search for new physics in dijet mass and angular distributions in (pp) collisions at ($\sqrt{s} = 7\text{ TeV}$) measured with the ATLAS detector”. In: *New J. Phys.* 13 (2011), p. 053044. DOI: [10.1088/1367-2630/13/5/053044](https://doi.org/10.1088/1367-2630/13/5/053044). arXiv: [1103.3864 \[hep-ex\]](https://arxiv.org/abs/1103.3864).
- 1995
1996
1997
- 1998 [11] ATLAS Collaboration. “ATLAS data quality operations and performance for 2015–2018 data-taking”. In: *JINST* 15.04 (2020), P04003. DOI: [10.1088/1748-0221/15/04/P04003](https://doi.org/10.1088/1748-0221/15/04/P04003). arXiv: [1911.04632 \[physics.ins-det\]](https://arxiv.org/abs/1911.04632).
- 1999
2000
- 2001 [12] ATLAS Collaboration. *ATLAS Pythia 8 tunes to (7 TeV) data*. ATL-PHYS-PUB-2014-021. 2014. URL: <https://cds.cern.ch/record/1966419>.
- 2002
- 2003 [13] ATLAS Collaboration. “Jet energy scale and resolution measured in proton–proton collisions at $\sqrt{s} = 13\text{ TeV}$ with the ATLAS detector”. In: *Eur. Phys. J. C* 81.8 (2021), p. 689. DOI: [10.1140/epjc/s10052-021-09402-3](https://doi.org/10.1140/epjc/s10052-021-09402-3). arXiv: [2007.02645 \[hep-ex\]](https://arxiv.org/abs/2007.02645).
- 2004
2005
2006
- 2007 [14] ATLAS Collaboration. “Jet energy scale measurements and their systematic uncertainties in proton-proton collisions at $\sqrt{s} = 13\text{ TeV}$ with the ATLAS detector”. In: *Phys. Rev. D* 96 (Oct. 2017), p. 072002. DOI: [10.1103/PhysRevD.96.072002](https://doi.org/10.1103/PhysRevD.96.072002). arXiv: [1703.09665 \[hep-ex\]](https://arxiv.org/abs/1703.09665).
- 2008
2009
2010
- 2011 [15] ATLAS Collaboration. “Jet reconstruction and performance using particle flow with the ATLAS Detector”. In: *Eur. Phys. J. C* 77 (2017), p. 466. DOI: [10.1140/epjc/s10052-017-5031-2](https://doi.org/10.1140/epjc/s10052-017-5031-2). arXiv: [1703.10485 \[hep-ex\]](https://arxiv.org/abs/1703.10485).
- 2012
2013
- 2014 [16] ATLAS Collaboration. “Light-quark and gluon jet discrimination in pp collisions at $\sqrt{s} = 7\text{ TeV}$ with the ATLAS detector”. In: *Eur. Phys. J. C* 74 (2014), p. 3023. DOI: [10.1140/epjc/s10052-014-3023-z](https://doi.org/10.1140/epjc/s10052-014-3023-z). arXiv: [1405.6583 \[hep-ex\]](https://arxiv.org/abs/1405.6583).
- 2015
2016
- 2017 [17] ATLAS Collaboration. “Luminosity determination in pp collisions at $\sqrt{s} = 13\text{ TeV}$ using the ATLAS detector at the LHC”. In: (Dec. 2022). arXiv: [2212.09379 \[hep-ex\]](https://arxiv.org/abs/2212.09379).
- 2018
2019
- 2020 [18] ATLAS Collaboration. “Measurement of jet charge in dijet events from $\sqrt{s}=8\text{ TeV}$ pp collisions with the ATLAS detector”. In: *Phys. Rev. D* 93.5 (2016), p. 052003. DOI: [10.1103/PhysRevD.93.052003](https://doi.org/10.1103/PhysRevD.93.052003). arXiv: [1509.05190 \[hep-ex\]](https://arxiv.org/abs/1509.05190).
- 2021
2022

REFERENCES

- 2023 [19] ATLAS Collaboration. “Measurement of jet shapes in top-quark pair events at \sqrt{s}
2024 = 7 TeV using the ATLAS detector”. In: *Eur. Phys. J. C* 73.12 (2013), p. 2676. DOI:
2025 10.1140/epjc/s10052-013-2676-3. arXiv: 1307.5749 [hep-ex].
- 2026 [20] ATLAS Collaboration. “Measurement of the flavour composition of dijet events
2027 in pp collisions at $\sqrt{s} = 7$ TeV with the ATLAS detector”. In: *Eur. Phys. J. C*
2028 73.2 (2013), p. 2301. DOI: 10.1140/epjc/s10052-013-2301-5. arXiv:
2029 1210.0441 [hep-ex].
- 2030 [21] ATLAS Collaboration. “Performance of the ATLAS track reconstruction algo-
2031 rithms in dense environments in LHC Run 2”. In: *Eur. Phys. J. C* 77.10 (2017),
2032 p. 673. DOI: 10.1140/epjc/s10052-017-5225-7. arXiv: 1704.07983
2033 [hep-ex].
- 2034 [22] ATLAS Collaboration. “Performance of the ATLAS trigger system in 2015”. In:
2035 *Eur. Phys. J. C* 77 (2017), p. 317. DOI: 10.1140/epjc/s10052-017-
2036 4852-3. arXiv: 1611.09661 [hep-ex].
- 2037 [23] ATLAS Collaboration. *Quark versus Gluon Jet Tagging Using Charged-Particle*
2038 *Constituent Multiplicity with the ATLAS Detector*. ATL-PHYS-PUB-2017-009.
2039 Geneva, 2017. URL: <https://cds.cern.ch/record/2263679>.
- 2040 [24] ATLAS Collaboration. *Quark versus Gluon Jet Tagging Using Jet Images with*
2041 *the ATLAS Detector*. ATL-PHYS-PUB-2017-017. 2017. URL: <https://cds.cern.ch/record/2275641>.
- 2043 [25] ATLAS Collaboration. *Recommendations for the Modeling of Smooth Backgrounds*.
2044 ATL-PHYS-PUB-2020-028. 2020. URL: <https://cds.cern.ch/record/2743717>.
- 2046 [26] ATLAS Collaboration. “Search for diboson resonances with boson-tagged jets in
2047 pp collisions at $\sqrt{s}= 13$ TeV with the ATLAS detector”. In: *Phys. Lett. B* 777
2048 (2018), p. 91. DOI: 10.1016/j.physletb.2017.12.011. arXiv: 1708.04445 [hep-ex].
- 2050 [27] ATLAS Collaboration. “Search for New Particles in Two-Jet Final States in (7 TeV) *Proton–*
2051 *–Proton Collisions with the ATLAS Detector at the LHC*”. In: *Phys. Rev. Lett.* 105 (2010),
2052 p. 161801. DOI: 10.1103/PhysRevLett.105.161801. arXiv: 1008.2461 [hep-ex].

REFERENCES

- 2054 [28] ATLAS Collaboration. “Search for new phenomena in the dijet mass distribution
2055 using (pp) collision data at ($\sqrt{s} = 8\text{ TeV}$) with the ATLAS detector”. In: *Phys. Rev.*
2056 *D* 91 (2015), p. 052007. DOI: [10.1103/PhysRevD.91.052007](https://doi.org/10.1103/PhysRevD.91.052007). arXiv:
2057 [1407.1376 \[hep-ex\]](https://arxiv.org/abs/1407.1376).
- 2058 [29] ATLAS Collaboration. “Search for new resonances in mass distributions of jet
2059 pairs using (139 fb^{-1}) of (pp) collisions at ($\sqrt{s} = 13\text{ TeV}$) with the ATLAS detector”.
2060 In: *JHEP* 03 (2020), p. 145. DOI: [10.1007/JHEP03\(2020\)145](https://doi.org/10.1007/JHEP03(2020)145). arXiv:
2061 [1910.08447 \[hep-ex\]](https://arxiv.org/abs/1910.08447).
- 2062 [30] ATLAS Collaboration. “Search for the Standard Model Higgs boson produced
2063 by vector-boson fusion and decaying to bottom quarks in $\sqrt{s} = 8\text{ TeV}$ pp colli-
2064 sions with the ATLAS detector”. In: *JHEP* 11 (2016), p. 112. DOI: [10.1007/JHEP11\(2016\)112](https://doi.org/10.1007/JHEP11(2016)112). arXiv: [1606.02181 \[hep-ex\]](https://arxiv.org/abs/1606.02181).
- 2066 [31] ATLAS Collaboration. *The ATLAS Collaboration Software and Firmware*. ATL-
2067 SOFT-PUB-2021-001. 2021. URL: <https://cds.cern.ch/record/2767187>.
- 2069 [32] ATLAS Collaboration. “The ATLAS Experiment at the CERN Large Hadron Col-
2070 linder”. In: *JINST* 3 (2008), S08003. DOI: [10.1088/1748-0221/3/08/S08003](https://doi.org/10.1088/1748-0221/3/08/S08003).
- 2072 [33] P. Bagnaia et al. “Measurement of Jet Production Properties at the CERN anti-p
2073 p Collider”. In: *Phys. Lett.* 144B (1984), pp. 283–290. DOI: [10.1016/0370-2693\(84\)91822-7](https://doi.org/10.1016/0370-2693(84)91822-7).
- 2075 [34] Johannes Bellm et al. “Herwig 7.0/Herwig++ 3.0 release note”. In: *Eur. Phys. J.*
2076 *C* 76.4 (2016), p. 196. DOI: [10.1140/epjc/s10052-016-4018-8](https://doi.org/10.1140/epjc/s10052-016-4018-8). arXiv:
2077 [1512.01178 \[hep-ph\]](https://arxiv.org/abs/1512.01178).
- 2078 [35] Enrico Bothmann et al. “Event generation with Sherpa 2.2”. In: *SciPost Phys.* 7.3
2079 (2019), p. 034. DOI: [10.21468/SciPostPhys.7.3.034](https://doi.org/10.21468/SciPostPhys.7.3.034). arXiv: [1905.09127 \[hep-ph\]](https://arxiv.org/abs/1905.09127).
- 2081 [36] C. Frye, A. J. Larkoski, J. Thaler and K. Zhou. “Casimir meets Poisson: improved
2082 quark/gluon discrimination with counting observables”. In: *JHEP* 09 (2017), p. 083.
2083 DOI: [10.1007/JHEP09\(2017\)083](https://doi.org/10.1007/JHEP09(2017)083). arXiv: [1704.06266 \[hep-ph\]](https://arxiv.org/abs/1704.06266).

REFERENCES

- 2084 [37] Matteo Cacciari and Gavin P. Salam. “Pileup subtraction using jet areas”. In: *Phys.*
2085 *Lett. B* 659.1 (2008), pp. 119–126. DOI: <https://doi.org/10.1016/j.physletb.2007.09.077>. arXiv: 0707.1378 [hep-ph].
- 2087 [38] Matteo Cacciari, Gavin P. Salam, and Gregory Soyez. “FastJet User Manual”. In:
2088 *Eur. Phys. J. C*72 (2012), p. 1896. DOI: 10.1140/epjc/s10052-012-
2089 1896-2. arXiv: 1111.6097 [hep-ph].
- 2090 [39] Matteo Cacciari, Gavin P. Salam, and Gregory Soyez. “The anti-(k_t) jet clustering algorithm”.
2091 In: *JHEP* 04 (2008), p. 063. DOI: 10.1088/1126-6708/2008/04/063.
2092 arXiv: 0802.1189 [hep-ph].
- 2093 [40] CDF Collaboration. “Measurement of b -jet shapes in inclusive jet production in
2094 $p\bar{p}$ collisions at $\sqrt{s} = 1.96$ TeV”. In: *Phys. Rev. D* 78 (2008), p. 072005. DOI:
2095 10.1103/PhysRevD.78.072005. arXiv: 0806.1699 [hep-ex].
- 2096 [41] CDF Collaboration. “Study of jet shapes in inclusive jet production in $p\bar{p}$ colli-
2097 sions at $\sqrt{s} = 1.96$ TeV”. In: *Phys. Rev. D* 71 (2005), p. 112002. DOI: 10.1103/
2098 PhysRevD.71.112002. arXiv: hep-ex/0505013.
- 2099 [42] CDF Collaboration, T. Aaltonen et al. “Search for new particles decaying into
2100 dijets in proton-antiproton collisions at $\sqrt{s} = 1.96$ ”. In: *Phys. Rev. D* 79 (Aug.
2101 2009), p. 112002. DOI: 10.1103/PhysRevD.79.112002. arXiv: 0812.
2102 4036 [hep-ex].
- 2103 [43] CLEO Collaboration. “Comparison of particle production in quark and gluon frag-
2104 mentation at $\sqrt{s} \sim 10$ GeV”. In: *Phys. Rev. D* 76 (2007), p. 012005. DOI: 10.
2105 1103/PhysRevD.76.012005. arXiv: 0704.2766 [hep-ex].
- 2106 [44] CMS Collaboration. “Electroweak production of two jets in association with a Z
2107 boson in proton-proton collisions at $\sqrt{s}= 13$ TeV”. In: *Eur. Phys. J. C* 78 (2018),
2108 p. 589. DOI: 10.1140/epjc/s10052-018-6049-9. arXiv: 1712.09814
2109 [hep-ex].
- 2110 [45] CMS Collaboration. “Measurement of jet substructure observables in $t\bar{t}$ events
2111 from proton-proton collisions at $\sqrt{s} = 13$ TeV”. In: *Phys. Rev. D* 98 (2018), p. 092014.
2112 DOI: 10.1103/PhysRevD.98.092014. arXiv: 1808.07340 [hep-ex].

REFERENCES

- 2113 [46] CMS Collaboration. “Measurement of the jet mass in highly boosted $t\bar{t}$ events
2114 from pp collisions at $\sqrt{s} = 8$ TeV”. In: *Eur. Phys. J. C* 77.7 (2017), p. 467. DOI:
2115 [10.1140/epjc/s10052-017-5030-3](https://doi.org/10.1140/epjc/s10052-017-5030-3). arXiv: [1703.06330](https://arxiv.org/abs/1703.06330) [hep-ex].
- 2116 [47] CMS Collaboration. “Measurements of jet charge with dijet events in pp collisions
2117 at $\sqrt{s} = 8$ TeV”. In: *JHEP* 10 (2017), p. 131. DOI: [10.1007/JHEP10\(2017\)131](https://doi.org/10.1007/JHEP10(2017)131).
2118 arXiv: [1706.05868](https://arxiv.org/abs/1706.05868) [hep-ex].
- 2119 [48] CMS Collaboration. “Measurements of the differential jet cross section as a func-
2120 tion of the jet mass in dijet events from proton-proton collisions at $\sqrt{s} = 13$ TeV”.
2121 In: *JHEP* 11 (2018), p. 113. DOI: [10.1007/JHEP11\(2018\)113](https://doi.org/10.1007/JHEP11(2018)113). arXiv:
2122 [1807.05974](https://arxiv.org/abs/1807.05974) [hep-ex].
- 2123 [49] CMS Collaboration. *Performance of quark/gluon discrimination using pp colli-*
2124 *sion data at $\sqrt{s} = 8$ TeV*. CMS-PAS-JME-13-002. 2013. URL: <https://cds.cern.ch/record/1599732>.
- 2126 [50] CMS Collaboration. “Search for Dijet Resonances in (7 TeV) (pp) Collisions at CMS”.
2127 In: *Phys. Rev. Lett.* 105 (2010), p. 211801. DOI: [10.1103/PhysRevLett.105.211801](https://doi.org/10.1103/PhysRevLett.105.211801). arXiv: [1010.0203](https://arxiv.org/abs/1010.0203) [hep-ex].
- 2129 [51] CMS Collaboration. “Studies of jet mass in dijet and W/Z + jet events”. In: *JHEP*
2130 05 (2013), p. 090. DOI: [10.1007/JHEP05\(2013\)090](https://doi.org/10.1007/JHEP05(2013)090). arXiv: [1303.4811](https://arxiv.org/abs/1303.4811)
2131 [hep-ex].
- 2132 [52] CMS Collaboration. “Study of quark and gluon jet substructure in Z+jet and di-
2133 jet events from pp collisions”. In: *JHEP* 01 (2022), p. 188. DOI: [10.1007/JHEP01\(2022\)188](https://doi.org/10.1007/JHEP01(2022)188). arXiv: [2109.03340](https://arxiv.org/abs/2109.03340) [hep-ex].
- 2135 [53] De-Chang Dai et al. “BlackMax: a black-hole event generator with rotation, recoil,
2136 split branes, and brane tension”. In: *Phys. Rev. D* 77 (2008), p. 076007. DOI: [10.1103/PhysRevD.77.076007](https://doi.org/10.1103/PhysRevD.77.076007). arXiv: [0711.3012](https://arxiv.org/abs/0711.3012) [hep-ph].
- 2138 [54] DELPHI Collaboration. “The scale dependence of the hadron multiplicity in quark
2139 and gluon jets and a precise determination of C_A/C_F ”. In: *Phys. Lett. B* 449 (1999),
2140 pp. 383–400. DOI: [10.1016/S0370-2693\(99\)00112-4](https://doi.org/10.1016/S0370-2693(99)00112-4). arXiv: [hep-ex/9903073](https://arxiv.org/abs/hep-ex/9903073).

REFERENCES

- 2142 [55] Sayipjamal Dulat et al. “New parton distribution functions from a global analysis
2143 of quantum chromodynamics”. In: *Phys. Rev. D* 93.3 (2016), p. 033006. DOI: [10.1103/PhysRevD.93.033006](https://doi.org/10.1103/PhysRevD.93.033006). arXiv: [1506.07443](https://arxiv.org/abs/1506.07443) [hep-ph].
- 2145 [56] Lyndon Evans and Philip Bryant. “LHC Machine”. In: *JINST* 3 (2008), S08001.
2146 DOI: [10.1088/1748-0221/3/08/S08001](https://doi.org/10.1088/1748-0221/3/08/S08001).
- 2147 [57] Stefano Frixione, Paolo Nason, and Carlo Oleari. “Matching NLO QCD com-
2148 putations with parton shower simulations: the POWHEG method”. In: *JHEP* 11
2149 (2007), p. 070. DOI: [10.1088/1126-6708/2007/11/070](https://doi.org/10.1088/1126-6708/2007/11/070). arXiv: [0709.2092](https://arxiv.org/abs/0709.2092) [hep-ph].
- 2151 [58] J. Gallicchio and M. D. Schwartz. “Quark and Gluon Tagging at the LHC”. In:
2152 *Phys. Rev. Lett.* 107 (2011), p. 172001. DOI: [10.1103/PhysRevLett.107.172001](https://doi.org/10.1103/PhysRevLett.107.172001). arXiv: [1106.3076](https://arxiv.org/abs/1106.3076) [hep-ph].
- 2154 [59] V. V. Gligorov et al. *Avoiding biases in binned fits*. 2021. arXiv: [2104.13879](https://arxiv.org/abs/2104.13879)
2155 [physics.data-an].
- 2156 [60] Philippe Gras et al. “Systematics of quark/gluon tagging”. In: *JHEP* 07 (2017),
2157 p. 091. DOI: [10.1007/JHEP07\(2017\)091](https://doi.org/10.1007/JHEP07(2017)091). arXiv: [1704.03878](https://arxiv.org/abs/1704.03878) [hep-ph].
- 2158 [61] L. A. Harland-Lang et al. “Parton distributions in the LHC era: MMHT 2014
2159 PDFs”. In: *Eur. Phys. J. C* 75.5 (2015), p. 204. DOI: [10.1140/epjc/s10052-015-3397-6](https://doi.org/10.1140/epjc/s10052-015-3397-6). arXiv: [1412.3989](https://arxiv.org/abs/1412.3989) [hep-ph].
- 2161 [62] Robert M. Harris and Konstantinos Kousouris. “Searches for dijet resonances at
2162 hadron colliders”. In: *Int. J. Mod. Phys. A* 26 (2011), pp. 5005–5055. DOI: [10.1142/S0217751X11054905](https://doi.org/10.1142/S0217751X11054905). arXiv: [1110.5302](https://arxiv.org/abs/1110.5302) [hep-ex].
- 2164 [63] J. Gallicchio and M. D. Schwartz. “Quark and gluon jet substructure”. In: *JHEP*
2165 04 (2013), p. 090. DOI: [10.1007/JHEP04\(2013\)090](https://doi.org/10.1007/JHEP04(2013)090). arXiv: [1211.7038](https://arxiv.org/abs/1211.7038)
2166 [hep-ph].
- 2167 [64] Guolin Ke et al. “LightGBM: A Highly Efficient Gradient Boosting Decision
2168 Tree”. In: *Advances in Neural Information Processing Systems 30 (NIPS 2017)*.
2169 Curran Associates, Inc. URL: https://proceedings.neurips.cc/paper_files/paper/2017/file/6449f44a102fde848669bdd9eb6b76fa-Paper.pdf.

REFERENCES

- 2172 [65] Patrick T. Komiske, Eric M. Metodiev, and Matthew D. Schwartz. “Deep learning in color: towards automated quark/gluon jet discrimination”. In: *JHEP* 01
2173 (2017), p. 110. DOI: [10.1007/JHEP01\(2017\)110](https://doi.org/10.1007/JHEP01(2017)110). arXiv: [1612.01551](https://arxiv.org/abs/1612.01551)
2174 [[hep-ph](#)].
2175
- 2176 [66] Patrick T. Komiske, Eric M. Metodiev, and Jesse Thaler. “An operational defi-
2177 nition of quark and gluon jets”. In: *JHEP* 11 (2018), p. 059. DOI: [10.1007/JHEP11\(2018\)059](https://doi.org/10.1007/JHEP11(2018)059). arXiv: [1809.01140](https://arxiv.org/abs/1809.01140) [[hep-ph](#)].
2178
- 2179 [67] David Krohn et al. “Jet Charge at the LHC”. In: *Phys. Rev. Lett.* 110 (May 2013),
2180 p. 212001. DOI: [10.1103/PhysRevLett.110.212001](https://doi.org/10.1103/PhysRevLett.110.212001). arXiv: [1209.2421](https://arxiv.org/abs/1209.2421) [[hep-ph](#)].
2181
- 2182 [68] Andrew J. Larkoski, Gavin P. Salam, and Jesse Thaler. “Energy correlation func-
2183 tions for jet substructure”. In: *JHEP* 06 (2013), p. 108. DOI: [10.1007/JHEP06\(2013\)](https://doi.org/10.1007/JHEP06(2013)108)
2184 [108](https://arxiv.org/abs/1305.0007). arXiv: [1305.0007](https://arxiv.org/abs/1305.0007) [[hep-ph](#)].
2185
- 2186 [69] Andrew J. Larkoski, Jesse Thaler, and Wouter J. Waalewijn. “Gaining (mutual)
2187 information about quark/gluon discrimination”. In: *JHEP* 11 (2014), p. 129. DOI:
2188 [10.1007/JHEP11\(2014\)129](https://doi.org/10.1007/JHEP11(2014)129). arXiv: [1408.3122](https://arxiv.org/abs/1408.3122) [[hep-ph](#)].
2189
- 2190 [70] Ian Moult, Lina Necib, and Jesse Thaler. “New angles on energy correlation func-
2191 tions”. In: *JHEP* 12 (2016), p. 153. DOI: [10.1007/JHEP12\(2016\)153](https://doi.org/10.1007/JHEP12(2016)153).
2192 arXiv: [1609.07483](https://arxiv.org/abs/1609.07483) [[hep-ph](#)].
2193
- 2194 [71] S. Mrenna and P. Skands. “Automated parton-shower variations in PYTHIA 8”. In:
2195 *Phys. Rev. D* 94.7 (2016), p. 074005. DOI: [10.1103/PhysRevD.94.074005](https://doi.org/10.1103/PhysRevD.94.074005).
2196 arXiv: [1605.08352](https://arxiv.org/abs/1605.08352) [[hep-ph](#)].
2197
- 2198 [72] Paolo Nason. “A new method for combining NLO QCD with shower Monte Carlo
2199 algorithms”. In: *JHEP* 11 (2004), p. 040. DOI: [10.1088/1126-6708/2004/11/040](https://doi.org/10.1088/1126-6708/2004/11/040). arXiv: [hep-ph/0409146](https://arxiv.org/abs/hep-ph/0409146).
2200
- 2197 [73] Nishu Nishu et al. *Search for New Phenomena in Dijet Events using the complete
2198 Run-2 dataset collected with the ATLAS Detector at $\sqrt{s} = 13$ TeV*. Tech. rep. ATL-
2199 COM-PHYS-2018-1538. Geneva: CERN, Nov. 2018. URL: <https://cds.cern.ch/record/2646455>.

REFERENCES

- 2201 [74] NNPDF Collaboration, Richard D. Ball, et al. “Parton distributions with LHC
2202 data”. In: *Nucl. Phys. B* 867 (2013), p. 244. DOI: [10.1016/j.nuclphysb.2012.10.003](https://doi.org/10.1016/j.nuclphysb.2012.10.003). arXiv: [1207.1303](https://arxiv.org/abs/1207.1303) [hep-ph].
- 2204 [75] OPAL Collaboration. “Experimental properties of gluon and quark jets from a
2205 point source”. In: *Eur. Phys. J. C* 11 (1999), pp. 217–238. DOI: [10.1007/s100520050628](https://doi.org/10.1007/s100520050628). arXiv: [hep-ex/9903027](https://arxiv.org/abs/hep-ex/9903027).
- 2207 [76] J. Pumplin et al. “New Generation of Parton Distributions with Uncertainties from
2208 Global QCD Analysis”. In: *JHEP* 07 (2002), p. 012. DOI: [10.1088/1126-6708/2002/07/012](https://doi.org/10.1088/1126-6708/2002/07/012). arXiv: [hep-ph/0201195](https://arxiv.org/abs/hep-ph/0201195).
- 2210 [77] Steffen Schumann and Frank Krauss. “A parton shower algorithm based on Catani–
2211 Seymour dipole factorisation”. In: *JHEP* 03 (2008), p. 038. DOI: [10.1088/1126-6708/2008/03/038](https://doi.org/10.1088/1126-6708/2008/03/038). arXiv: [0709.1027](https://arxiv.org/abs/0709.1027) [hep-ph].
- 2213 [78] Torbjorn Sjöstrand, Stephen Mrenna, and Peter Z. Skands. “PYTHIA 6.4 physics
2214 and manual”. In: *JHEP* 05 (2006), p. 026. DOI: [10.1088/1126-6708/2006/05/026](https://doi.org/10.1088/1126-6708/2006/05/026). arXiv: [hep-ph/0603175](https://arxiv.org/abs/hep-ph/0603175).
- 2216 [79] Torbjörn Sjöstrand et al. “An introduction to PYTHIA 8.2”. In: *Comput. Phys.*
2217 *Commun.* 191 (2015), p. 159. DOI: [10.1016/j.cpc.2015.01.024](https://doi.org/10.1016/j.cpc.2015.01.024). arXiv:
2218 [1410.3012](https://arxiv.org/abs/1410.3012) [hep-ph].
- 2219 [80] The NNPDF Collaboration, Richard D. Ball, et al. “Parton distributions for the
2220 LHC run II”. In: *JHEP* 04 (2015), p. 040. DOI: [10.1007/JHEP04\(2015\)040](https://doi.org/10.1007/JHEP04(2015)040).
2221 arXiv: [1410.8849](https://arxiv.org/abs/1410.8849) [hep-ph].
- 2222 [81] Pourya Vakilipourtakalou and Douglas M. Gingrich. “Monte Carlo event generator
2223 for the production and decay of string resonances in proton-proton collisions”. In:
2224 (Nov. 2018). arXiv: [1811.07458](https://arxiv.org/abs/1811.07458) [hep-ph].
- 2225 [82] Wouter Verkerke and David Kirkby. *The RooFit toolkit for data modeling*. 2003.
2226 arXiv: [physics/0306116](https://arxiv.org/abs/physics/0306116) [physics.data-an].
- 2227 [83] Jan-Christopher Winter, Frank Krauss, and Gerhard Soff. “A modified cluster-
2228 hadronization model”. In: *Eur. Phys. J. C* 36 (2004), pp. 381–395. DOI: [10.1140/epjc/s2004-01960-8](https://doi.org/10.1140/epjc/s2004-01960-8). arXiv: [hep-ph/0311085](https://arxiv.org/abs/hep-ph/0311085).
- 2230 [84] Hongtao Yang. *quickFit*. 2021. URL: https://gitlab.cern.ch/atlas_higgs_combination/software/quickFit (visited on 06/22/2021).

REFERENCES

- 2232 [85] Hongtao Yang. *XML Analytic Workspace Builder*. 2021. URL: <https://twiki.cern.ch/twiki/bin/viewauth/AtlasProtected/XmlAnaWSBuilder> (visited on 06/22/2021).
- 2233
- 2234
- 2235 [86] ZEUS Collaboration. “Substructure dependence of jet cross sections at HERA and
- 2236 determination of alpha(s)”. In: *Nucl. Phys. B* 700 (2004), pp. 3–50. DOI: [10.1016/j.nuclphysb.2004.08.049](https://doi.org/10.1016/j.nuclphysb.2004.08.049). arXiv: [hep-ex/0405065](https://arxiv.org/abs/hep-ex/0405065).
- 2237

2238

8 Acknowledgements

2239 ◦